THÈSE

En vue de l'obtention du

DOCTORAT DE L'UNIVERSITÉ DE TOULOUSE

Délivré par :
Institut National Polytechnique de Toulouse (INP Toulouse)

Discipline ou spécialité :

Microondes, ElectroMagnétisme, Optoélectronique

Présentée et soutenue par :
Usman ZABIT
le : mardi 20 juillet 2010

Titre :

Optimisation of a Self-mixing Laser Displacement Sensor

JURY
Prof. Stephen Wilson
Dr Francis Bony
Dr Frédéric Grillot
Dr Maurizzio Dabbicco
Dr Anne Marie de Smet

Ecole doctorale :
Génie Electrique, Electronique et Télécommunications (GEET)
Unité de recherche :
Laboratoire d'Optoélectronique pour les Systèmes embarqués
Directeur(s) de Thèse :

Prof. Thierry Bosch

Rapporteurs :
Prof Pascal Picart
Prof. Horacio Lamela Rivera

Acknowledgements

First of all, I wish to thank my research advisor Prof. Thierry Bosch whose contribution to my thesis cannot be stated enough. I am highly indebted to his continuous involvement and guidance over the course of the thesis in spite of his many responsibilities and hectic timetable. His ever-present enthusiasm and availability never failed to encourage me while his scientific curiosity and acuity moulded and enriched my research work. But, it is at a personal level that I admire him most for his irrepressible sense of humour, flourishing eloquence and eclectic tastes. I treasure the endless hours that I spent in his presence, full of wit and observation.

I would like to express my gratitude for Prof. Horacio Lamela Rivera of University Carlos III of Madrid and Prof. Pascal Picart of University of Maine, Le Mans who kindly accepted to review my research work despite their research activities and busy schedules at this time of the year. Their remarks and observations have helped me further improve the quality of this manuscript.

I am also honoured by the presence of Prof. Stephen Wilson of University of Queensland, Australia who has so kindly accepted to be a part of the jury. Likewise, I would like to thank Dr. Marie-Anne de Smet of Airbus Industries, Dr. Maurizio Dabbicco of University of Pavia, Italy, and Dr. Frédéric Grillot of INSA-Rennes, all of who have graciously accepted to be a member of the jury.

My thoughts are also with Francis Bony who helped me become self-reliant in my research activities. I am also thankful to Olivier Bernal for his cheering presence and insightful participation towards the end of the thesis.

I would also like to highlight the contribution of Reza Atashkhooei and Dr. Santiago Royo of Technical University of Catalonia, Spain. It has been a pleasure collaborating with them and I sincerely appreciate their warm and cordial personalities.

Likewise, I thank Prof. Aleksandar Rakic of University of Queensland for the part that he has taken in my research activities. I'd also mention the time spent with Russell Kliese whose technical acumen is only surpassed by his humane nature.

I am also indebted to the technical support and friendly encouragement provided by Clément Tronche and Francis Jayat during the experiments. I would equally thank Emmanuelle Tronche for her help and patience that allows me to wade through the paperwork.

Let me put in a word for Han-Cheng Seat and Julien Perchoux for their help with whom I shared many an hour of teaching classes. I really admire their wonderful and intriguing personalities.

I am also thankful for the good humour and patience of my fellow PhD students, past and present, Caroline, Pierre, Laurent, Josephe, Maha, Saroj, Emmanuel, Florent, Lucie, Raphael and Bendy. Let me underscore the delicious dinners to which I was invited by Saroj and all the thoughtful advice and friendship provided by the kind-hearted Maha. I also appreciate the exuberance brought by the internees that have shared our office, Chao, Harold and Cristina, ever ready to laugh out loud.

On a personal note, what I feel for my parents, my mother Habiba Shaheen and my father Raja Zabit Hussain, is more profound than mere words. I can’t count the sacrifices they did for the little ones. They have given their lifeblood to see me grow and then fly away. I hope that my work will be a source of happiness for them even if I have wavered along the way.

I express my love for Omer and Fakiha, my siblings that have always found a way of bringing a smile to my face. I hope that they have thoroughly enjoyed my absence for a grumbling, frowning brother is not the best gift that one may get.

Finally, I do wish to heartily thank my friends and flat-mates, Amir, Ahmad and Aamir. The time I spent in their company and the tales that we weaved together is the thing that I shall cherish all my life. Likewise, I wish all the best to Olivier, Stéphane and the drifters from Arsenal. I express my gratitude for those close to me in Colmar once we got to France. I equally appreciate everyone at FJT Espérance Toulouse who have twice welcomed me and brought me such surprises. I remain grateful for the hospitality accorded by Gilles and Marilyne. Thanks to all who have brightened my days these last few years. Sometimes, I feel as if life in France has been like being with Alice in wonderland.

Usman Zabit

Toulouse

Table of Contents

Introduction

The field of metrological sensing continues to rely on optics based solutions, as contrary to other measuring techniques which necessitate a contact with the target surface, an optical sensor provides a precise and contact-less measurement of the target motion. Various optical instruments exist in the market, which use, among others, the principle of classical interferometry to obtain results with excellent precision. However, high cost, difficult alignment and cumbersome nature of various optical components needed in the set-up remain important hindrances to their increased use under industrial conditions.

Within this context, the principle of Self-Mixing Interferometry provides us with a sensing solution that is compact, self-aligned and cost-effective while providing very good precision. In this technique, instead of using a separate receiving channel to first gather and then mix the light beam that has been reflected by the moving target, the back-reflected beam in allowed to enter the active laser cavity. The resultant interference signal is then retrieved and signal processing is done in order to retrieve the target movement.

An often-reported configuration has been the use of a laser diode as a light source where the interferometric signal of the active cavity is then captured by the built-in photodiode of the laser diode package. Recent results have, however, shown that the laser diode junction voltage can be used to retrieve the same information. Thus, in such a configuration, the laser diode acts simultaneously as a light source, as a micro-interferometer as well as a light detector. The sensor component count can then be resumed by a laser diode, a focusing lens and an electronic circuitry used to recover, amplify and digitalize the signal. Such a synthesis thus opens up new possibilities for increased miniaturization and replication of the sensor.

Some major challenges, however, remain before the Self-Mixing Interferometry based metrological sensors can reliably be used to provide increased precision measurement results under industrial conditions. For example, firstly, in order to go beyond the basic half-wavelength precision of the sensor, various signal processing methods have been proposed. The goal is then to improve such techniques such that the algorithms become faster and can be easily integrated into hardware. Secondly, solutions are also needed to counter the influence of various self-mixing phenomena that can perturb, complicate or falsify the target motion extraction, namely; the disappearance of self-mixing fringes, the change in self-mixing optical feedback regime or the issue of speckle. Thirdly, the measurement range of the sensor needs to be improved and the sensor needs to be robust with respect to the conditions dictated by industrial use, i.e. presence of parasitic mechanical vibrations, misalignment between the sensor and the target, and the lack of possibility of preparing the target surface.

Thus, this present thesis, addresses the three major issues highlighted in the previous paragraph so that a precise, reliable and robust self-mixing based displacement sensor be designed. The present work has highlighted the hardware or signal processing solutions that can be used as building blocks in order to achieve the objective of the realization of an autonomous, miniature, robust embedded metrological sensor.

The thesis manuscript has been written with the following order.

The first chapter has been dedicated to an introduction to the phenomenon of the Self-Mixing Interferometry. In its first section, the well-documented equivalent cavity model has been used to characterize the phenomenon. Then, the expressions for the threshold gain and allowed emission frequencies, the phase as well as the optical output power have been derived. In the second section of this introductory chapter, various applications of the phenomenon have been presented, such as the measurement of displacement, vibration, linear and rotating velocity as well as absolute distance.

The second chapter starts by explaining in detail an existing displacement measuring algorithm. Then, various approaches have been discussed that aim to reduce the execution time of this algorithm either by improving the routines used within this algorithm or by replacing these routines with others that are better suited for actual sensing conditions. This chapter thus contains the sections dedicated to the analysis of a Fourier Transform based approach, an adapted Nelder-Mead algorithm as well as the hybrid optimization algorithm.

The third chapter presents a major portion of the research work achieved during this thesis. It starts by presenting a new algorithm inspired from the work presented in the second chapter. It is of a real-time nature and has the added advantage of the detection and correction of self-mixing fringe disappearance, a phenomenon that happens due to increased optical feedback. The second section of this chapter presents a technique that makes the sensor autonomous with respect to a possible self-mixing feedback regime change. The third section details the use of adaptive optics in the shape of a liquid lens that allows us to maintain the signal in a fringe-loss free regime as well as to increase the laser to target distance range over which the measurement can be accurately done. This chapter thus presents the adaptive solutions to the issue of varying optical feedback that can cause a change in self-mixing regime as well as fringe-loss. These solutions are either algorithmic in nature such as the fringe-loss compensating algorithm and the adaptive fringe-detection algorithm or the use of a liquid lens to electronically control the optical feedback into the laser cavity thereby staying in a favorable feedback regime.

The fourth and final chapter presents the work done so that the sensor can even be used under realistic conditions where non-cooperative target surfaces, misalignment between the target and the sensor as well as parasitic mechanical vibrations exist. This chapter then starts with the presentation of a solution to the issue of speckle for centimetric displacements. The second section proposes a technique for the correction of parasitic vibrations undergone by the sensor under unfavorable industrial conditions that would have falsified the sensor measurement. For this purpose, a sold-state accelerometer has been added to the sensor that monitors the parasitic vibrations undergone by the sensor and then a correction is done so as to obtain the true target movement. The third section presents the work done to optimize the trigonometric functions needed for the algorithms while also giving a highlight of the future FPGA implementation.

Finally, a general conclusion is presented followed by a list of publications done during the course of this thesis.

I Self-Mixing and its Applications

The usefulness of lasers, especially in the field of instrumentation, has long been recognized. Thus, many systems using these sources have already been proposed. However, a limitation arises in the case of an optical beam back-scattering into the active cavity. This retro-injection may occur as a result of reflection either by the target itself or the optical equipment involved, such as a lens used in the set-up. Indeed, the reflected beam induces significant changes in power level and frequency of the laser emission. In 1963, King & Stewart [1] were the first to see variations of optical power output of a gas laser, due to the back-scattered beam inside the cavity. This phenomenon, generally described as "self-mixing" in the literature, was originally considered parasitic for certain applications, such as optical fiber communications, as well as in compact disc players. Considerable efforts were made to reduce this phenomenon, e-g by the introduction of optical isolating elements. This, however, led to the increase in the cost and the complexity of the system. Then, it was revealed that the sensitivity of the laser to the back-scattered beam offered many advantages in certain applications. Indeed, Rudd [2] in 1968, is the first to use the effect of "self-mixing" for measuring Doppler velocity using a Helium-Neon laser. In 1984, Churnside [3] [4] studied the laser Doppler velocimetry with a CO2 laser.

However, it is pertinent to underline that this phenomenon has mainly been studied in the case of laser diodes to take advantage of the compactness and the low cost of this type of source. As early as 1980, Dandridge et al [5] presented a laser diode sensor capable of detecting sinusoidal displacements as small as ~ 9×10^{-5} nm. The sensor, designed for acoustic application, employed an external reflector placed at 10µm from the laser diode and used the phase modulation of light fed back into the laser cavity. It so followed that the theory of this optical phenomenon has been studied and implemented to achieve distance, displacement and velocity sensors using laser diodes [6]-[10].

Self-mixing thus remains an active area of research with its latest applications in fields as varied as the sensing of the net motion of an ensemble of brownian particles suspended in water [11] to its use in nanomechanical polymer cantilever sensing [12] as well as in medical applications to generate blood flow maps [13].

In this chapter, we start by presenting a simplified analysis of the phenomenon of "self-mixing", then we shall outline the various applications based on this phenomenon.

I.1 Self-Mixing Phenomenon

When laser diode beam points on a target, a small portion of the emitted laser beam is reflected from the target and then re-injected into the laser cavity. This has the effect of altering the power and the frequency of laser emission. This phenomenon has been called "Self-mixing", "Frequency-modulated laser diode" (Beheim), "Backscatter-modulated laser diode" (de Groot), "External optical feedback effect" (Lang), "Active optical feedback" (Wang), and "Feedback interferometry" (Donati).

The principle of self-mixing is indicated in on the right side of Fig. I:1. Such a system can be compared with a classical Michelson interferometer. However, the measurement system based on self-mixing is simple, cost-effective, little complicated and auto-aligned as it only necessitates a laser diode and normally a photodiode included in the same chip as well as a focusing lens. So it avoids the traditional optical components (mirrors, isolators, splitters) that are expensive and need a great care in their handling and alignment.

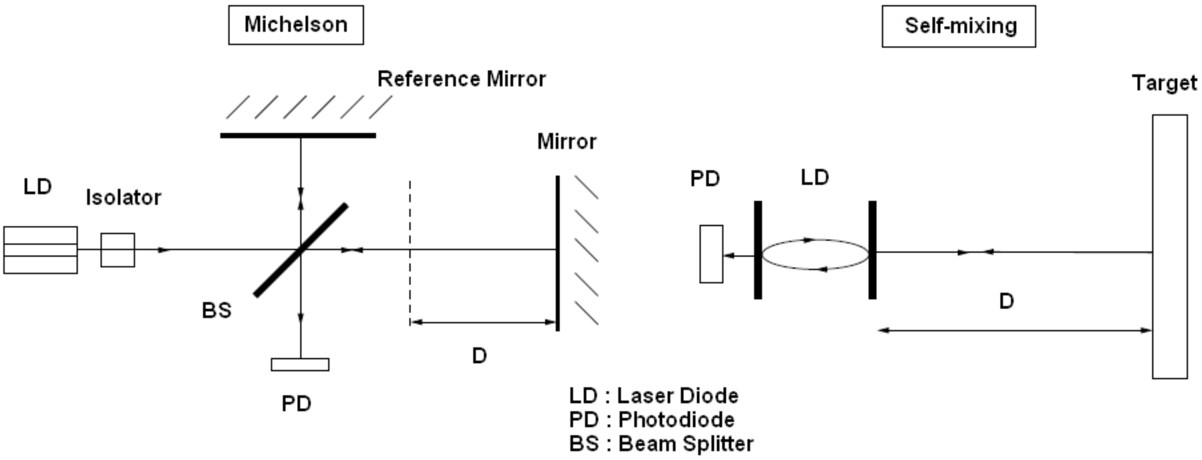

Fig. I:1 Analogy between a Michelson based interference and a Self-mixing based interference.

As a result of reflection by a target, the retro-injected light interferes with the existing light field of the laser cavity. This, however, requires that the target be at a distance of less than the half of the coherence length of the laser subject to feedback. The photodiode (PD) integrated in the laser diode

(LD) casing (Fig. I:2), that is normally used to control the power of emission of the diode laser, is then used to detect variations in optical power that are induced by the interference or the phenomenon of “self-mixing”. The output power is then modulated if the target is in motion or if the laser diode injection current is modulated or when the refractive index between the laser and the target is varying. It is also mentioned that the PD is inclined by some degrees as compared to the back facet of the LD in order to avoid a back-reflection due to PD.

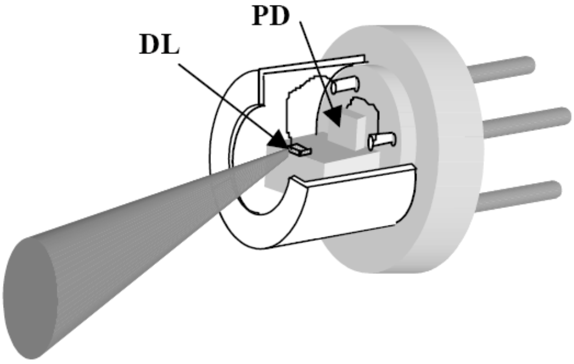

Fig. I:2 Schematic diagram of the component containing the laser diode and the internal photodiode.

Moreover, in some recent self-mixing set-ups even the use of PD has been eliminated by directly monitoring the variations of the LD junction voltage [15]- [16]. Thus, SM can then be used for those LDs that do not have a built-in PD. This opens the way to even have an array of LDs that would be grown on the same chip. However, a relatively lower signal to noise ratio of the SM signal retrieved from across the LD junction as compared to a PD retrieved SM signal remains an issue [17].

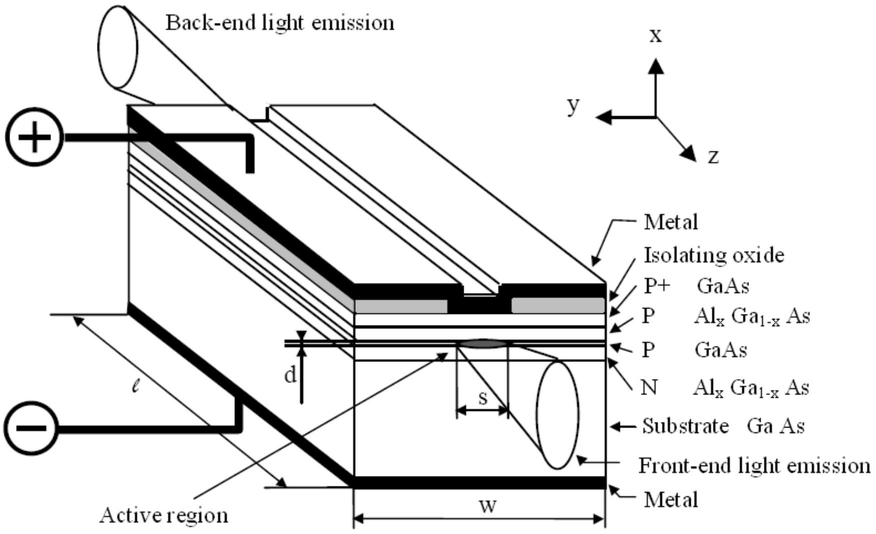

Fig. I:3 A double hetero-junction laser diode. The active cavity has a length l*, a width* s *and a thickness* d *[14].*

As compared to the classical interferences, the self-mixing interferences occur in the semiconductor active medium (see Fig. I:3) whereas classical interferences are normally observed in free space, i.e. in passive medium. This important difference results in an asymmetric, non-sinusoidal form of the intensity modulation that happens with self-mixing.

The remarkable aspect of LD based SM device is the fact that the LD simultaneously acts as a light source, as a micro-interferometer as well as a light detector, thus resulting in a compact optical sensor.

In order to explain in detail the self-mixing phenomenon, i.e. the influence of optical retro-injection into the laser cavity on the laser emission, we can use the model of coupled cavities, with the target acting as an external optical cavity. For this, we need first to describe the behavior of the diode laser in a stand-alone condition, followed by the behavior of the laser diode in the presence of a target.

I.1.1 Stand-alone Laser Diode

The active medium of a laser diode of length *l*, bounded by two interfaces I_1 and I_2 can be modeled as a Fabry-Perot cavity (Fig. I:4). The reflection coefficients for the electric field amplitude are denoted as r_i and r'_i, where the index *i* represents the interface concerned.

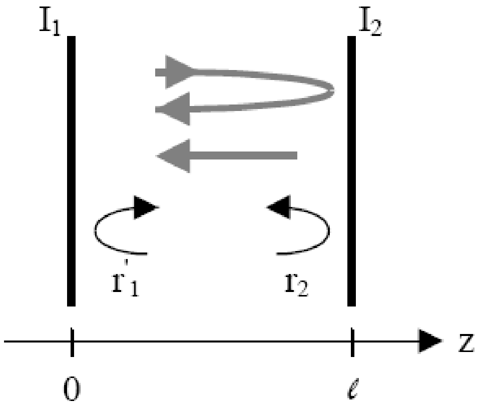

Fig. I:4. Modelling of the active medium of a laser diode as an equivalent Fabry-Perot cavity.

According to Petermann [18], the condition of emission of the laser diode without external coupling can be stated as:

$$r_1' r_2 \exp\left(-j\frac{4\pi\mu_{e0}\nu_0}{c}l\right)+(g_{th0}-\alpha_p)l=1 \tag{1-1}$$

where μ_{e0} represents the effective refractive index of the active region, ν_0 is the laser diode emission frequency, *c* is the speed of light, g_{th0} is the threshold gain of the active region and α_p is the coefficient representing the losses mainly due to absorption by the free carriers.

Solving this equation leads to the expressions of threshold gain and the allowed optical frequencies of the diode laser, given by (1-2), where *q* is an integer.

$$g_{th0} = \alpha_p - \frac{1}{l}\left(r_1' r_2\right) \qquad (1\text{-}2)$$

$$\nu_0 = q \frac{c}{2 l \mu_{e0}}$$

I.1.2 Laser Diode in the presence of a target

I.1.2.a Equivalent Cavity Model

Let us now consider the same diode laser in the presence of a target located at a distance l_{ext}. This set-up can be interpreted as a combination of a Fabry-Perot type laser cavity of length *l*, along with a long external cavity of length l_{ext}. These two can now be modeled as an equivalent Fabry-Perot cavity of length *l* (Fig. I:5).

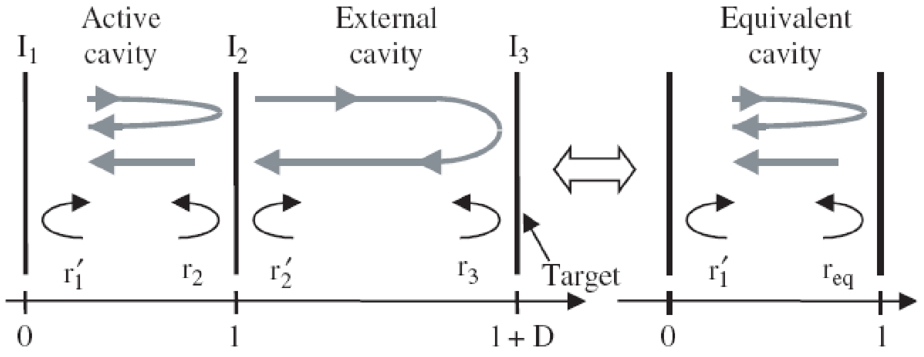

Fig. I:5. Modelling of a laser diode in the presence of a target by an equivalent Fabry-Perot cavity.

The coefficient r_{eq} represents the amplitude of the reflection coefficient of the equivalent cavity. Now, for the case of weak retro-diffusion (i.e. when the amplitude of the reflection coefficient of the target r_3 is small as compared to that of the front facet of the laser diode r_2), we can neglect the multiple reflections in the external cavity [19]. The amplitude of reflection coefficient of the equivalent cavity is thus written as:

$$r_{eq}(\nu) = r_2\left(1 + \kappa \exp(-j 2\pi \nu_F \tau_{ext})\right)$$

$$= \left\| r_{eq} \right\| \exp(-j\phi_{eq}) \quad \text{, with } \phi_{eq} = \kappa \sin(2\pi \nu_F \tau_{ext}) \qquad (1\text{-}3)$$

where ν_F is the optical frequency of the laser diode in the presence of the target, τ_{ext} is the time of flight of the laser beam in the external cavity and κ is a parameter denoting the coupling effect between the target and the laser cavity (such as $0 < \kappa < 1$). The parameter ϕ_{eq} is the inverse of the phase of the equivalent reflection coefficient.

$$\tau_{ext} = \frac{2\,l_{ext}}{c} \quad \text{and} \quad \kappa = \frac{r_3}{r_2}(1-r_2^2) \tag{1-4}$$

The condition of laser emission for a diode in the presence of coupling with a target (1-5) is none other than the equation (1-1) where the values for the laser diode in stand-alone condition (specified by the subscript 0) are replaced by those for the equivalent diode (specified by the subscript F). Thus, the reflection coefficient r_2 is replaced by the coefficient r_{eq} of the equivalent laser cavity.

$$r_1 \cdot r_{eq} \exp\left(-j\frac{4\pi\mu_{eF}\nu_F}{c}l\right)+(g_{thF}-\alpha_p)l=1 \tag{1-5}$$

I.1.2.b Threshold gain and allowed emission frequencies

We can now write in a single equation (1-6), the two laser emission conditions for an equivalent laser diode, under free running conditions (i.e. in the absence of target) and subject to feedback, namely equations (1-1) et (1-5).

$$\left\|\frac{r_{eq}}{r_2}\right\| \exp\left(-j(\phi_F-\phi_0)+(g_{thF}-\alpha_p)l\right)=1 \tag{1-6}$$

$$\text{where, } \phi_F = \frac{4\pi\mu_{eF}\nu_F}{c}+\phi_{eq} \quad \text{and} \quad \phi_0 = \frac{4\pi\mu_{e0}\nu_0}{c}$$

So, we can thus deduce the relations for the gain (1-7) and the phase (1-8), where g_{th} , ϕ and μ_e are the laser emission threshold gain, the phase of laser emission and the effective refractive index respectively.

$$g_{thF}-g_{th0} = -\frac{\kappa}{l}\cos(2\pi\nu_F\tau_{ext}) \tag{1-7}$$

$$\phi_F-\phi_0 = \frac{4\pi l}{c}(\mu_{eF}\nu_F-\mu_{e0}\nu_0)+\kappa\sin(2\pi\nu_F\tau_{ext})=0 \tag{1-8}$$

However, the effective refractive index μ_e depends on the density of electrons n and the emission frequency ν. Thus, for a small variation in these parameters for the case of a diode with external coupling (n_F and ν_F) as compared to the case of no external coupling (n_0 and ν_0), we obtain the expression for the variation in the effective refractive index.

$$\Delta\mu_e = \mu_{eF}-\mu_{e0} = \left(\frac{\partial\mu_e}{\partial n}\right)\cdot\Delta n+\left(\frac{\partial\mu_e}{\partial\nu}\right)\cdot\Delta\nu \tag{1-9}$$

for $\Delta\nu = \nu_F-\nu_0$ and $\Delta n = n_F-n_0$

Substituting this differential of the effective refractive indices in the phase equation (1-8), we then obtain the equation (1-10).

$$\nu_0\left(\frac{\partial\mu_e}{\partial n}\right)\cdot\Delta n+\left\{\left(\frac{\partial\mu_e}{\partial\nu}\right)\cdot\nu_0+\mu_{e0}\right\}\cdot\Delta\nu+\kappa\frac{c}{4\pi l}\sin(2\pi\nu_F\tau_{ext})=0 \qquad (1\text{-}10)$$

Now, considering the effective refractive index μ_e in its complex form, the electric field E of the plane wave (propagating along the z axis, with a wave vector k) can be written as:

$$E=E_0\exp(-jk\mu_e z) \qquad \text{with} \qquad \mu_e=\mu_{\grave{e}}-j\mu_{\ddot{e}} \qquad (1\text{-}11)$$

$$k=2\pi/\lambda=2\pi\nu_0/c$$

Moreover, for a constant density of injection current higher than the threshold for laser emission, the electrons' densities are equal to that of the threshold. Thus, for a small change in the gain and the electron density between the diode in the absence and presence of target, we can write the following relationship given by Petermann [18]:

$$\left(\frac{\partial\mu_{\ddot{e}}}{\partial n}\right)=-\frac{c}{4\pi\nu_0}\cdot\left(\frac{\partial g}{\partial n}\right)=-\frac{c}{4\pi\nu_0}\cdot\left(\frac{g_{thF}-g_{th0}}{n_F-n_0}\right) \qquad (1\text{-}12)$$

The relation between the emission frequencies of the laser diode (1-13) is then obtained by introducing the relation (1-12) into the relation (1-10), where α is the line-width enhancement factor, defined by the partial derivative of the real part of the effective refractive index as compared to its imaginary part.

$$\nu_F-\nu_0+\frac{c}{4\pi l\bar{\mu}_{e0}}\kappa\sqrt{1+\alpha^2}\sin(2\pi\nu_F\tau_{ext}+\arctan\alpha)=0 \qquad (1\text{-}13)$$

$$\text{with } \alpha=\left(\frac{\partial RE(\mu_e)}{\partial IM(\mu_e)}\right)=-\left(\frac{\partial\mu_{\grave{e}}}{\partial\mu_{\ddot{e}}}\right)$$

and $\bar{\mu}_{e0}=\mu_e+\nu_0\left(\frac{\partial\mu_e}{\partial\nu}\right)$ represents the group effective refractive index of the diode in the absence of target.

Now by introducing the feedback coupling coefficient C , defined by (1-14), where $\tau_l=\bar{\mu}_{e0}\frac{2l}{c}$ is the time of flight in the laser cavity, we obtain the expression for ν_F, the emission frequency of the laser subject to feedback [20].

$$C=\frac{\tau_{ext}}{\tau_l}\kappa\sqrt{1+\alpha^2} \qquad (1\text{-}14)$$

$$\nu_F - \nu_0 + \frac{C}{2\pi\tau_{ext}}\sin(2\pi\nu_F\tau_{ext} + \arctan\alpha) = 0 \tag{1-15}$$

The parameter C depends simultaneously on the time of flight through the external cavity τ_{ext} and therefore on the distance to the target, as well as on the target-laser diode coupling parameter κ and therefore on the quantity of light retro-diffused by the target.

I.1.2.c Influence of the Phase

In order to observe the influence of the phase, let us rewrite the relation (1-15) as the so-called phase equation:

$$\Delta\Phi_L = \nu_F - \nu_0 + \frac{C}{2\pi\tau_{ext}}\sin(2\pi\nu_F\tau_{ext} + \arctan\alpha) \tag{1-16}$$

$\Delta\Phi_L$ may be simulated (using MATLAB ®) and plotted as a function of (ν_F - ν_0) for different values of C (Fig. I:6). The zero crossings of these curves correspond to solution of the phase equation and thereby possible emission frequencies or modes of the laser.

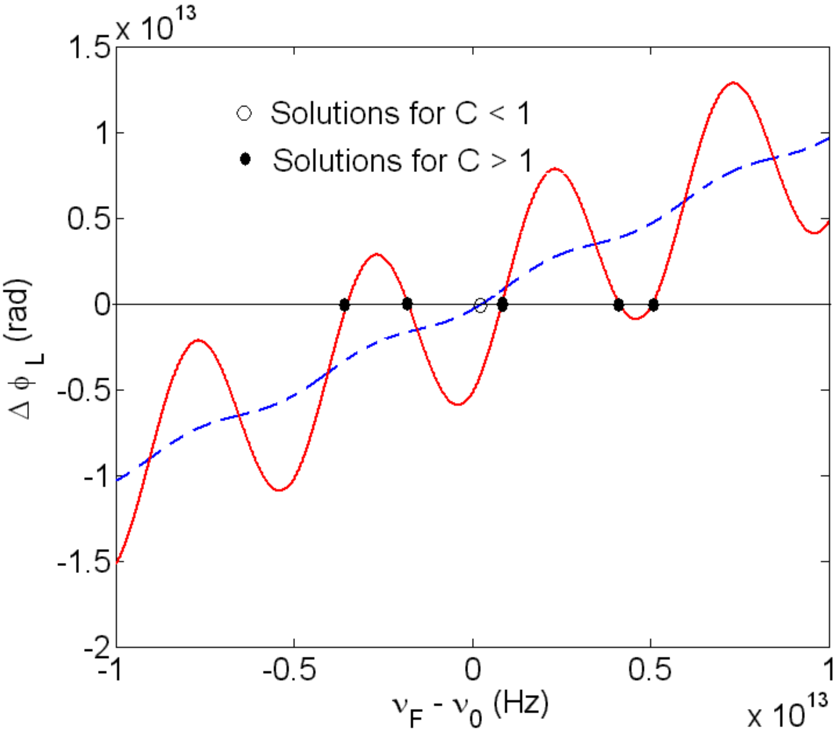

Fig. I:6 Solution of the phase equation for C=0.5(dashed line) and C=7.5(solid line). The white circle denotes only one solution for C<1 and black circles represent multiple solutions for C>1.

- The case of C < 1

As indicated in Fig. I:6, for values such as $C < 1$ corresponding to weak levels of feedback, only one solution can be found for equation (1.16) meaning that the laser will have one single lasing mode when subject to feedback which maybe encountered in the case of a lot of non-cooperative targets. Such a regime has often been described as the weak feedback regime.

- The case of C > 1

Now, for stronger feedbacks (i.e. $C > 1$) the phase equation may have several solutions. In fact, if the case of maximum 3 possible solutions is studied the limit of this regime may be found numerically by solving equation (1.16). C_a is the maximum value of C corresponding to only three solutions and which can be calculated and found to be $C_a = 4.7$ [21]. In this case, the laser is found to stay single-mode because, among the three possible modes, only the mode having the narrowest spectral width will be chosen by the laser [14]. The self-mixing signals obtained under such conditions are often referred to as belonging to the moderate feedback regime.

Thus, depending on the number of solutions, on which C has a major effect, the functioning of the laser can be divided into five regimes [22], as shown in Fig. I:7.

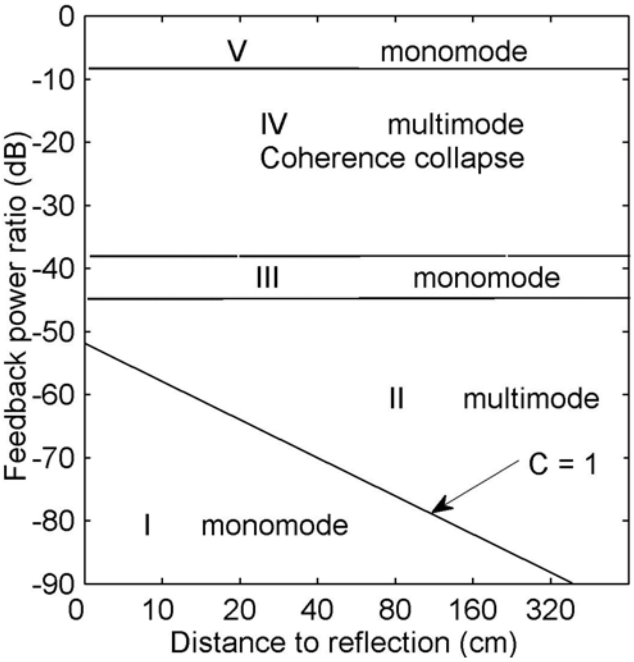

Fig. I:7 The 'regimes of feedback effects' showing the feedback power levels at which the output of a semiconductor laser transitions between unique modes of operation as a function of reflector distance [22].

Regime I	Very small feedback (the feedback fraction of the amplitude is less than 0.01%) and small effects. The linewidth of the laser oscillation becomes broad or narrow, depending on the feedback fraction.

Regime II	Small, but not negligible effects (less than ~ 0.1%). Generation of the external modes gives rise to mode hopping among internal and external modes
Regime III	This is a narrow region around ~ 0.1% feedback. The laser is perfectly single-mode and the spectral width is very narrow.
Regime IV	Moderate feedback (around 1%). It is the coherence collapse regime in which the laser diode loses all its coherence properties and the laser linewidth is broadened greatly.
Regime V	Strong feedback regime (higher than 10% feedback). The laser comes back to being single-mode with a very high rejection on the lateral modes of the laser cavity. This regime is characterized by a very narrow spectral width [23].

I.1.2.d Optical Output Power

Now, in order to formulate the expression of the optical output power of the laser diode under feedback, we must start from the equation of recombination of electrons in the laser cavity as a function of time [24]-[25]:

$$\frac{dn_0}{dt}=\frac{1}{e}\frac{\partial J}{\partial x}-v_g S_0 g(n_0)-\frac{n_0}{\tau_n} \tag{1-17}$$

where n_0 is the density of electrons for the stand-alone laser, t is time, e the elementary charge, J the current density, v_g the group velocity, S_0 the density of photons for the stand-alone laser and τ_n the electron half-life. This relationship assumes that all carriers are injected into the active zone of the diode laser. This is achieved by the help of a double hetero-junction (Fig. I:3).

Let us simultaneously consider the cases where the diode laser is single or in stand-alone condition (subscript 0) and subject to feedback (subscript F). Now, assuming that the diode is driven in both cases by a constant current density J and that its gain remains linear, we obtain the following set of equations:

$$\frac{J}{ed}=v_g S_0 \frac{\partial g_{lin}}{\partial x}(n_{th0}-n_{nul})+\frac{n_{th0}}{\tau_n} \tag{1-18}$$

$$\frac{J}{ed}=v_g S_F \frac{\partial g_{lin}}{\partial x}(n_{thF}-n_{nul})+\frac{n_{thF}}{\tau_n}$$

where d is the width of the laser cavity (Fig. I:3). The notation in subscript *th* represents a variable threshold and the notation *lin* indicates that the gain is linear. n_{nul} is the density of electrons that results in attaining a null gain.

Using such a system and assuming that $\Delta n_{th} = n_{thF} - n_{th0}$ is small, we can express the density of photons in the presence of a target as a function of the density of photons under free running conditions.

$$S_F = S_0 \left[1 - \Delta n_{th} \frac{v_g \left(\frac{\partial g_{lin}}{\partial n} \right) - \frac{1}{S_0 \tau_n}}{v_g \left(\frac{\partial g_{lin}}{\partial n} \right) (n_{th0} - n_{nul})} \right] \qquad (1\text{-}19)$$

Now, recalling equation (1-7) that gives the gain of the diode in the presence of target as a function of gain of the stand-alone diode, we can introduce the phase $2\pi \nu_F \tau_{ext}$ in the expression of the density of photons (1 -19).

$$S_F = S_0 (1 + m_{\text{mod}} \cos(2\pi \nu_F \tau_{ext})) \text{ with } m_{\text{mod}} = \frac{\kappa}{g_{th0} l} \left[1 + 1/v_g S_0 \tau_n \left(\frac{\partial g_{lin}}{\partial n} \right) \right] \qquad (1\text{-}20)$$

m_{mod} is a parameter representing the modulation of the laser diode.

So, considering that the power of laser emission is proportional to the density of photons, we arrive at the following relationship:

$$P_F = P_0 (1 + m_{\text{mod}} \cos(2\pi \nu_F \tau_{ext})) \qquad (1\text{-}21)$$

where P_F and P_0 are the optical power with and without feedback respectively.

Thus, we can notice that the optical power (1-21) and optical frequency (1-16) of the laser diode in the presence of a target are dependent on the phase $(2\pi \nu_F \tau_{ext})$, thereby involving the distance to the target by the help of the τ_{ext} parameter. Thus, the emission of the diode laser will be modified either if the injection current is modulated (ν_c is modulated) or if the target is in motion (τ_{ext} is modulated) or both. The photodiode integrated in the laser casing (Fig. I:2) is then used to detect variations in optical output power (OOP) that are induced by the phenomenon of “self-mixing”.

Fig. I:8 presents three OOP signals obtained for different values of the feedback parameter C. Fig. I:8(a) shows a very weak feedback regime signal (C=0.2) with its fringes of quasi sinusoidal shape. Such a SM signal closely resembles the signals obtained with classical interferometers.

Then, in Fig. I:8(b) is presented a weak feedback regime signal (C=1) that has slightly asymmetric fringes. This asymmetric shape of the saw-tooth like signal has consistently been experimentally observed [25]. It was found that the influence of the variation of the refractive index on the feature of fringe inclination is related to the linewidth enhancement factor α in equation (1.16).

Finally, Fig. I:8 (c) represents a moderate feedback regime signal (C=4) that has saw-tooth shaped fringes along with hysteresis. More details about this regime shall be presented in the next chapters as it has been one of the subjects of interest during this thesis. Thus, we get to see the three major regimes of the SM signals.

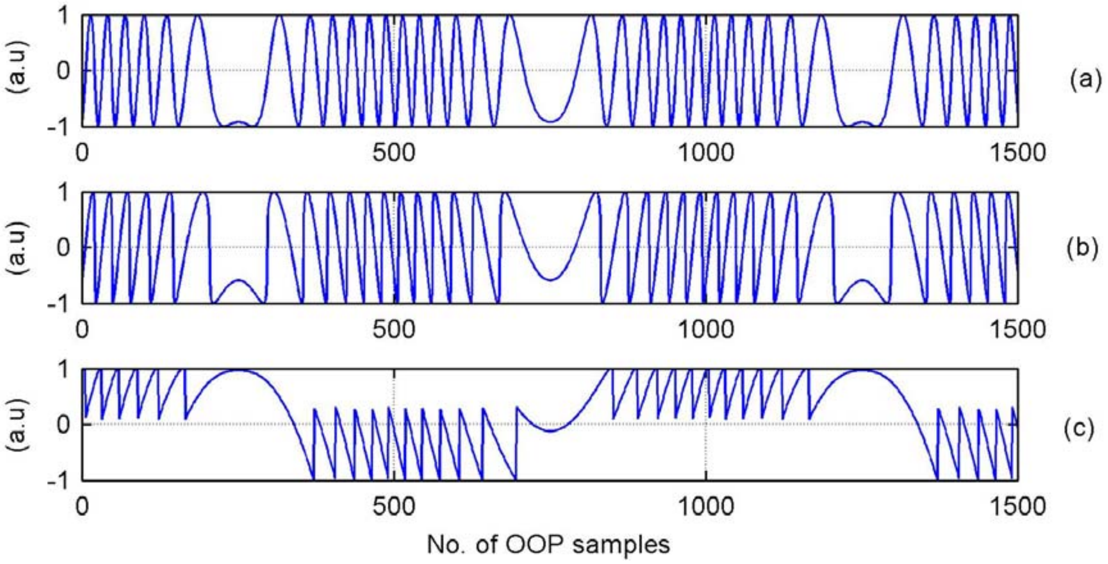

Fig. I:8 (a) OOP of a SM signal in the very weak feedback regime (C=0.2), (b) in the weak feedback regime (C=1), (c) in the moderate feedback regime (C=4).

Another quantity that is affected by self-mixing other than the laser optical power is the laser diode junction voltage V[26]. The change in laser junction voltage V can be related to the coupling coefficient of the external cavity and therefore to the feedback level and the location of the target [15], expressed as:

$$\Delta V = -K\cos(2\pi \nu_F \tau_{ext}) \tag{1-22}$$

where K is a constant of proportionality.

A comparison of (1-21) and (1-22) thus demonstrates that the self-mixing phenomenon can be observed either using the variations in the OOP or from the variations in the LD junction voltage. It is important to note that according to (1-21), output power varies proportionally with the change in target location while (1-22) exhibits an inverse relationship. This means that an increase in laser power coincides with a decrease in laser junction voltage – the two quantities are out of phase.

I.1.3 Conclusion

As mentioned earlier, the self-mixing (SM) signal was, and still is, considered as a parasite signal in applications like telecommunications and CD/DVD readers. The self-mixing causes the lowering of the efficiency of these systems. However, as can be verified from the expressions for the OOP in presence of a target, both the power (1.21) and the frequency (1.16) of the LD are modified by the variations of the distance separating the laser diode from the target, thus making SM very suitable for metrological measurements [6]-[10].

This last characteristic gives the SM effect a sensing ability which is accentuated by different other advantages such as:

- A simple and compact set-up as the sensor is self-aligned so there is no need for any of the expensive external optics used in traditional interferometry (Fig. I:1).
- No external photo-detector is required, because the signal is provided by the monitor photodiode already available in the laser diode package (Fig. I:2). Moreover, even this PD has been eliminated in some recent SM set-ups by directly monitoring the variations of the LD voltage.
- The sensitivity is very high, being a sort of coherent detection that easily attains the quantum detection regime (i.e. sub-nm sensitivity in path length is possible) [27].

I.2 Applications of the Self-Mixing Effect

The first demonstrations of this principle used gas lasers to detect the Doppler shift caused by a moving remote reflector [2]. After that, the first self-mixing interferometer that used heterodyne detection for a gas laser was presented [28], followed by the use of a laser diode as a source and a detector at the same time [29]. Remote sensing applications based on the self-mixing effect in low-cost commercial Fabry–Perot (FP) LDs appeared in the scientific literature first in 1986, demonstrating the feasibility of velocity, distance and displacement measurements [29]- [30]. A brief survey of the various self-mixing based applications is presented below.

I.2.1 Displacement Measurement

Displacement measurements are achieved in different domains using multiple sensing technologies like resistive, inductive, capacitive, ultrasonic, magnetic and piezoelectric technologies [31]. Various optical displacement measuring transducers such as those based on techniques of Michelson interferometry, light intensity, position detection, photoelectromotive force and optical incremental encoding have also been used [32]. On the other hand, due to its simplicity, self-mixing interferometry is being exploited more and more in different sensing domains such as in particular displacement measurement or vibration analysis. As the present thesis is based on the optimisation of a SM based displacement sensor so a comparison between the various displacement sensors in general and between the various optical displacement sensors in particular shall be undertaken after a presentation of the use of SM for displacement sensing.

I.2.1.a Basic Principle

As mentioned earlier, the equations (1.16) and (1.21) giving the expressions of the emitted frequency and optical power are important. Both of these depend on the distance separating the laser from the target and the injection current. In fact, these two parameters will stay constant if the LD is driven by a DC injection current and if the laser to target distance is kept constant. However, when a back-reflection is generated by a moving target in the direction of light emission, the optical length of the external cavity is varying and consequently the length of the equivalent cavity is modified too, thus affecting the spectral properties of the laser.

The Fig. I:9 represents saw-tooth like modulation of a self-mixing signal corresponding to a sinusoidal displacement.

The OOP was expressed in (1.21) as an amplitude modulation where the phase is given by $\phi = 2\pi \nu_F \tau_{ext}$. Moreover, similar to traditional interferometry, the full swing of power matches to a half-wavelength displacement (considered theoretically as corresponding to a phase-shift of 2π).

$$\left|2\pi\nu\Delta(\tau_{ext})\right| = 2\pi \Leftrightarrow \left|\Delta D\right| = \lambda/2 \qquad (1.23)$$

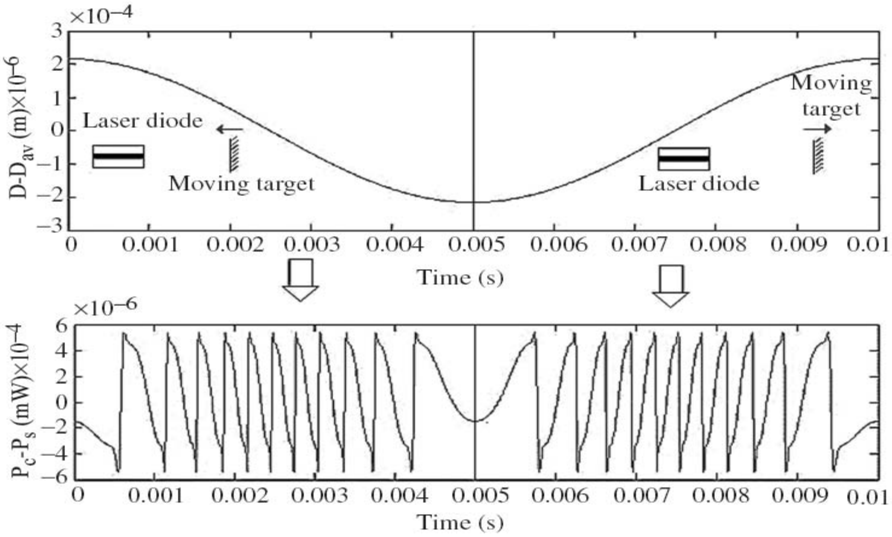

Fig. I:9. Saw-tooth like fluctuations for a sinusoidal displacement.

I.2.1.b Fringe Counting

A method traditionally used to retrieve the displacement with a basic resolution of *λ/2* is the fringe counting method based on the consideration that the number of saw-tooth like fringes is directly proportional to the displacement. It consists in counting these power fluctuations and adding them with their proper sign. Thus, for a motion in one direction, if *N* fluctuations are detected, the corresponding displacement *D* of the target is theoretically given by $D=N(\lambda/2)$. The asymmetric shape of the saw-tooth like signal permits to directly recover the target direction of displacement.

Such a method has been used even in 2008 by Ottonelli for a 3 Degrees-of-Freedom motion sensor based on SM effect [33] for the simultaneous measurement of the linear displacement and two rotation angles (yaw and pitch) of a moving object using a laser head that includes three commercial laser diodes for a target that has a plane mirror attached to it.. However, it will be demonstrated later in this manuscript that this method should normally be limited to the weak feedback regime.

In order to compare this set-up with a conventional system, such information can be conventionally achieved with two interferometry channels. In the case of single-channel optical feedback interferometry, the only optical component required is a lens used to collimate the laser source with the purpose of focusing the emitted light on the remote target, thus showing the advantage of simplicity of these systems.

I.2.1.c Increase of Resolution

Other methods exist for increasing the basic half-wavelength resolution of displacement measurement. A fast modulation of the optical path difference of a feedback interferometer will modify the round-trip external delay. For example, this can be achieved by using the electro-optical properties of a lithium Niobate crystal acting as a phase modulator [34]. Theoretically, *W* self-mixing signals can be used with phases spaced by $2\pi/W$. A sampling of these signals then results in a displacement with a resolution of $\lambda_0/2W$. Experimentally, a DSP card has been used for simultaneous monitoring in order to achieve a resolution of $\lambda_0/10$ with 5 phase-shifts.

Another sensor has been developed with a resolution of $\lambda_0/12$ that consists in the linearization of the normalized optical power which has been approximated by an ideal saw-tooth signal [35]. Even if there is no need for preliminary measurements of parameters, this solution is limited to moderate feedback.

Likewise, a different approach has been the use of a pair of laser diodes, each with its own external cavity [36]. The first is used as a reference where as the other is perturbed by the target displacement. A spectrum analyser and a counter are however needed to count the beat frequency and visualize the spectrum. The reported reconstructed displacement has a resolution of 5 nm.

As a slight angle between the laser beam and the normal of the target favors multiple reflections of the beam before entering in the laser cavity so in this case one can double or even triple the self-mixing fringes. Thus, using a VCSEL of 850 nm, a resolution of $\lambda_0/6$ has been achieved for the case of a triple reflection for a target at 47mm from the laser diode [37].

Such a multiplication of the self-mixing fringes has also been reported for multi-mode laser diodes.

According to [38], depending on the amount of optical feedback, a subperiodicity appears in the amplitude modulation of the output power of laser under self-mixing. The experiments have shown that a subperiodicity appears independently of the length of the external cavity and is due to mode hopping between different longitudinal laser modes. A duplication or triplication of the fringes can then be used to increase the vibration measurement resolution.

Different signal processing methods have also been proposed to increase the basic resolution beyond half-wavelength such as the phase demodulation or un-wrapping method [39] that will be explained in detail in chapter II or the use of extended Kalman filters [40], the use of wavelets transforms [41] or even genetic algorithms [42].

I.2.1.d Vibration Measurement

Vibration measurement is essential in many mechanical or mechatronics fields where it can be used to minimize or eliminate the vibration noise. There are also examples where the noise is not the key parameter, but rather a parameter for quality control of the manufactured products. For example, excessive vibration can damage the product, limit processing speeds, or even cause catastrophic machine failure.

The study of self-mixing principle for the design of sensors in order to measure vibrations is reported since 1996 [44] where the small dimensions and the low-cost of such sensors are among the main practical reasons why researchers have concentrated their attention on this technique.

Self-mixing sensors were privileged in this type of applications because of different characteristics such as its high sensitivity, large bandwidth and a large dynamic range up to 70 KHz and 100 dB [45]. Moreover, it is able to function on different types of surfaces without any optical modulation and equally permits to measure low frequency vibrations. The sensor developed in [44] permitted to measure vibrations of approximately all types of surfaces with a bandwidth between 0.1 Hz and 70 KHz with a maximal peak to peak amplitude of 180 µm. A special algorithm was developed in order to analyse in real time the self-mixing signal permitting thereby to track the velocity variations of the target. The set-up, however, was quite complex with many optical components such as polarizing beam-splitters, half-wave plates and mirrors.

In 2004, a self-mixing sensor used in piezoelectric transducers characterization [46] permitted to measure the velocity and vibrations of solid targets with results comparable to those obtained by the conventional Laser Doppler Velocimeter (LDV). The technique used was similar to the one used in LDV where it was able to treat the signals even in presence of speckle with the simplicity of self-mixing sensors.

More recently, a new technique for signal recovery in an SM vibrometer has been published in 2008 [47]. The method of extracting the single beat frequency over a period containing at least a few fringes has allowed to rectify the problems of speckle, electromagnetic interference and mechanically induced parasitic signal fluctuations for an ultrasound solder vibrating at 20 kHz with an amplitude of 40µm.

I.2.1.e Comparison of Displacement Sensors

After a description of the use of self-mixing for displacement and vibration sensing, let us compare the merits of such a sensor with respect to others. As the self-mixing based sensors are of a compact, contact-less and auto-aligned nature so these become instantly attractive for many industrial applications. Such displacement sensors hold an advantage over in-contact sensors (such as accelerometers or strength gauges) in that these allow an inspection of parts that have complex geometry or are machined under hostile conditions (e.g. in furnaces). Likewise, these allow us an on-line control without fear of damaging the parts. Thus, the non-contact displacement sensors provide a non-intrusive and/or “on the fly” measurement for many industrial applications. Within this context, Table I-1 presents a comparison between the optical displacement measurement techniques with other existing methods [48].

Table I-1 A comparison between the optical displacement measurement techniques with other existing methods

Type	**Contact**	**Eddy current**	**Ultrasonic**	**Optical**	**Laser**
Target	Solids	Metal	Most objects	Most objects	Most objects
Distance	Short	Short	Long	Normal	Normal*
Accuracy	High	High	Low	High	High
Response Time	Slow	Fast	Slow	Fast	Normal
Robustess	High	High	Normal	Normal	Normal
Measured Zone	Small	Normal	Large	Small	Small

* with our technique, Short otherwise

Let us now analyse the characteristics of the main optical displacement sensors:

- Fibre optic based upon Reflection type: Such sensors (e.g. Philtec) are very precise and inexpensive but not flexible (very limited range: the sensor must be very close to the target).

- Diffractive interferometric sensors: These have a resolution of only several microns and are inflexible to use [49].

- External interferometer: Such sensors are very accurate but remain expensive and fragile due to very precisely aligned optical components and require a stable base.

- Optical fiber based interferometer: These are accurate in measurement but require many optical components which make these quite expensive to install and maintain. These sensors also need a stable base.

- PSD (position sensitive detector): These require a laser to illuminate the PSD, which acts as a photodetector. These allow a possibility to measure linear displacements in XY but loss of accuracy for non-cooperative targets remains an issue.

- Triangulation based Sensors: These allow an absolute distance measurement at a low cost but are hampered by the risk of a shadow zone due to their non-aligned and cumbersome nature.

A comparison of the limitations of the above-mentioned techniques with the SM based sensor developed over the course of this thesis is given below:

- Cumbersome: Diffractive interferometric sensors, Triangulation, and PSD.
- Cost: Interferometer, PSD
- Shadow zone: Triangulation
- Small range: Fiber optic based reflection type sensors
- Stable base: Interferometer, fiber optic reflection

I.2.2 Velocity Measurements

Velocity measurement is an essential parameter for safety and profitability of manufactured systems in different areas like aerospace, automotive, metallurgy or paper industry. In fact, there is an increasing need for remote sensing with rough targets in hostile environments or for in-line assembly processes.

Non-contact measurements can be performed with ultrasonic or microwaves devices but with poor spatial definition and therefore optoelectronic systems are an alternative solution of great interest. LDV is a very accurate method extensively developed for surface speed measurements but it is expensive because it requires high stability of both optics and mechanics [50]. An emerging method is the Tracking Laser Doppler Velocimetry (TLDV) which optimizes the tracking algorithm strategy compared to the LDV. Feedback interferometry presents the significant advantages of being compatible with a wide range of target characteristics (roughness, colour …) still at a very low-cost.

I.2.2.a Physical Principle

The technique of velocity measurement using self-mixing sensors is based on the Doppler-Fizeau effect

$$F_D = \frac{2V_F}{\lambda} \tag{1.24}$$

where F_D is the Doppler frequency that corresponds to the frequency of the saw-tooth like self-mixing signal and V_F is the velocity of the target. In fact, velocimetry was the first application of the self-mixing effect as the first realizations were accomplished using a gas laser He-Ne [2] and with CO2 lasers [3]. However these sources were able to determine the Doppler frequency only in a reduced frequency span.

It was not until the mid 80's [51] that laser diodes were first used in the weak feedback regime in order to determine the Doppler frequency with a spectrum analyzer or in the moderate feedback regime in order to determine the motion direction by using the peak inclination.

Recently VCSELs (Vertical Cavity Surface Emitting Lasers) have also been used, such as in the form of a miniaturized VCSEL based sensor platform for velocity measurement [52] as well as for their use in velocimetry around their bias point [53]. Although their signal to noise ratio (SNR) would have increased in their bistable mode but the signal in this case would lose his sawtooth like shape and will have instead a square shape causing thereby the loss of information about the displacement's direction.

I.2.2.b Rotation Velocities and in-plane Translation

The self-mixing sensors may also be used in order to measure velocities of displacements that are not necessarily in the propagation direction. In this case the Doppler frequency is given by the following equation:

$$F_D = \frac{2V_F}{\lambda}\cos(\Psi) \tag{1.25}$$

where in this case, V_F is the module of the velocity vector having Ψ as an angle with the propagation direction (Fig. I:10). This Doppler frequency can be easily determined by applying a real time Fast Fourier Transform (FFT) to the self-mixing signal.

An onboard velocity sensor using the self-mixing effect has been recently developed. Roughness of the target surface, wet target surfaces, non-controlled changes of incident angle, and speed vector vertical components have all been considered and a first prototype has been designed for automotive applications. In order to improve the accuracy as well as the robustness of the system, a double-laser diode sensor has also been successfully tested by removing the influence of the pitching and the pumping effects [54]. Furthermore, a second order auto-regressive algorithm has also been applied to the SM signal in order to ameliorate the system resolution by a factor of 10 in the case where the rough surface of the target strongly affected the Doppler frequency measurement [55].

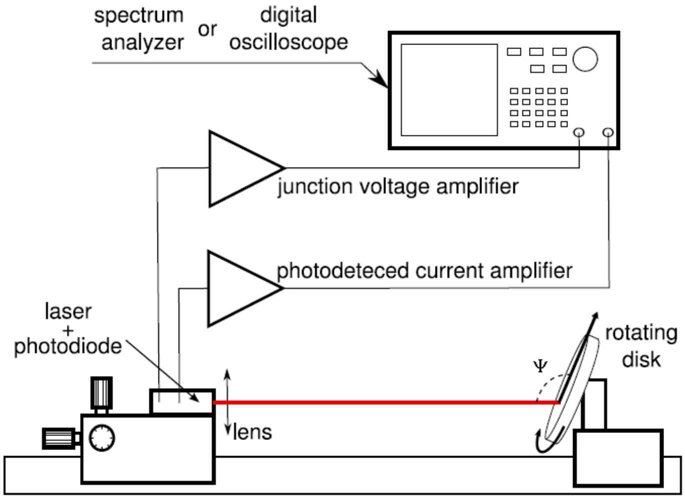

Fig. I:10 Rotating velocity found by SM using the PD current and the LD junction voltage.

Furthermore, a commercial 850nm VCSEL has been used in 2008 for SM velocimetry where the LD junction voltage has been amplified to extract the information [17] as seen in Fig. I:10. The signal-to-noise ratio of the laser diode voltage signal is comparable to the photodiode signal. The elimination of the photo-diode thus allows the design of bi-dimensional arrays of vertically emitting LD-based SM sensors.

I.2.2.b.1 Speckle Velocimetry

The speckle effect, which is normally of a detrimental influence for certain applications, can be used for detection of velocities of rough remote targets performing in-plane translation across the laser beam. The basic principle consists of a laser beam illuminating perpendicularly a non-cooperative surface in order to minimize the Doppler effect. When this surface is transversely translated, part of the reflected beam re-enter the laser cavity. As the speckle effect occurs, it causes random variations in the optical output power which is monitored by the photodiode within the laser package.

The first self-mixing laser speckle velocimeter was presented during the mid-1990s [56]. Unfortunately, this set-up needed for every surface type a preliminary calibration of parameters such as the beam spot size or the surface characteristics of the target. As a matter of fact, the frequency of optical power fluctuations varies notably for different surfaces moving at the same velocity. However, a linear relation between the autocorrelation time of the speckle signal from self-mixing velocimeter and the velocity of the rough remote target exists. This property has been used to ameliorate the calibration procedure and to optimise this sensor in terms of reproducibility and accuracy [57]. Such a sensor has been applied to characterize the surface roughness and their classification by the way of an artificial neural network [58].

I.2.3 Medical Applications

Self-mixing sensors have been exploited in different medical fields because of the multiple advantages previously described, especially their compact size and their ability to access measurement points without direct contact. For example, Zakian et al have recently reported a self-mixing interferometry configuration with a laser diode in order to generate flow maps by using Laser Doppler imaging technique [13]. The experiment was carried out by sensing the laser intensity power spectrum at each pixel as the laser was scanned over a model mimicking the properties of skin and circulating blood. Some other medical applications based on the self-mixing effect will be presented below.

The SM effect is used in conjunction with an optical fiber that allows one to remotely access intra-vessel points of measurement for local intra-arterial blood flow and velocity. In particular, the fiber is positioned in a blood vessel and the laser light coming out of the fiber tip penetrates into the blood and is scattered by the moving blood cells. A small part of the laser radiation is coupled back into the fiber and thanks to the interaction with moving cells providing the Doppler-shift, it will interfere inside the semiconductor cavity with the original frequency. A typical set-up is shown in Fig. I:11. A practical use of SM optical fiber set-up has been demonstrated with blood flow measurement of a pig [59].

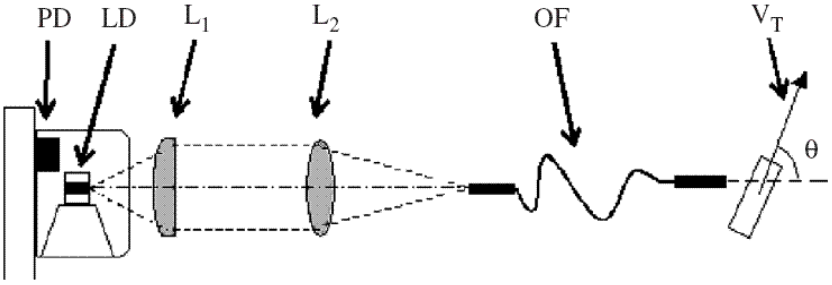

Fig. I:11 A typical fiber optic SM set-up for intra-arterial blood velocimetry. PD, photodiode built-in the laser diode case; LD, laser diode; L_1*, collimating lens;* L_2*, focusing lens; OF, optical fiber;* V_T*, velocity of the measured target.*

Likewise, a great interest from medical specialists is concentrated on the measurement of blood velocity in single microvessels. The main limit to the use of such methods was due to the maximum frequency band (less than 3 Hz) which did not permit the study of flow in animals with high heart rates. A standard SM optical fiber set-up, similar to the one reported in the previous paragraph, has been used for external measurement of the artery blood flow of sheep [60].

A complete non-invasive method for determination of local skin blood flow is also possible [61] by using SM set-up. The possibility to relate the autocorrelation speckle signals, generated on the built-in photodiode, and the blood flow velocity for the fingertip has thus been demonstrated. The latest comparative study with a commercially available Doppler flowmeter [62] has shown that the SM-LD-based system is capable of measuring the velocity of flow and identifying different blood flow regimes over the surface of human skin.

Another promising field of application in medicine for SM kind of sensors has been reported in the measurement of muscle vibration [63], known as mechanomyographic (MMG). MMG is used in sport medicine and to investigate the effect of neuromuscular diseases and age on muscle structure and state.

I.2.4 Absolute Distance Measurements

Laser range finder techniques can be classified in to three broad categories [64]:

- The geometric technique of triangulation is widely used for industrial applications due to its low cost, ease-of use and robustness. However, there is no auto-alignment in such a sensor as the source and the receiver are laterally separated. This may thus result in the shadow effect that can cause a missing of data because of directional occlusion. Moreover, the sensitivity is strongly dependent on the distance, and thus the measurement range is limited as a loss of precision happens for the distances greater than 1 meter.

- The time-of-flight (TOF) technique includes the pulsed technique which is similar to the one used with microwave radars or ultrasonic systems. It provides good results for long distance measurements of up to tens of km. The phase-shift based TOF measurement of a continuous wave and the FMCW (frequency modulated continuous wave) method (once again optical equivalent of the microwave technique) are appropriate for 1 to 100 meters target ranging. Generally, all of these time-of-flight devices are not the most accurate but their sensitivity is uniform throughout the whole measurement range.

- Interferometric technique provides us with the most accurate approach but it is very expensive and not so easy to implement. Such a method is mostly used for metrological applications when high accuracy is imperatively required. On the other hand, the self-mixing interferometry offers a low-cost and compact alternate solution that is quite easy to put into practice.

In this type of sensors, and contrary to all the other types introduced in this manuscript, the injection current is not constant but modulated with a properly shaped triangular waveform in order to perform absolute distance measurement in a very simple way. Thereby, in this case, the external cavity length can be constant, however the equivalent Fabry-Perot cavity's length will be modified because of variations in the active cavity's length caused by the current modulation. Thus, the length of the active cavity is modified and even for a stationary target the length of the Fabry-Perot equivalent cavity will consequently be changed. Both the power and the wavelength undergo a modulation. This induces a triangular variation $\Delta\lambda$ of the emitted optical wavelength λ and the corresponding wave number $(2\pi/\lambda)$ will then be changed by the amount $(-2\pi\Delta\lambda/\lambda^2)$ [9]. Variations of the optical power P_F due to the self-mixing signal will therefore be superimposed on the triangular carrier corresponding to P_0, the optical power without feedback (Fig. I:12). By performing a derivative of this self-mixing signal and then by digitalizing it, the distance can be calculated by several methods. The first sensor of this type was conceived by Berheim and Fritsch in 1986 [30] having a resolution of 15mm over a distance of 1.5m.

Initially, the distance *D* was calculated simply by counting the integer number of optical power fluctuations (also called peaks, spikes, pulses or modes) due to the feedback. Let us consider the case of a stationary target. N_1 and N_2—respectively the number of pulses recorded during the increasing and decreasing triangular semi-period—are then equal. Let us consider that $(N_1 + N_2)$ is equal to N, the total number of pulses during a complete period T of the triangular signal. The distance can then be expressed by the approximate relationship [9]:

$$D \approx \frac{\lambda^2}{2\Delta\lambda} N \left(= \frac{c}{2\Delta\upsilon} N \right) \tag{1-26}$$

where c is the speed of light and Δν the optical frequency shift.

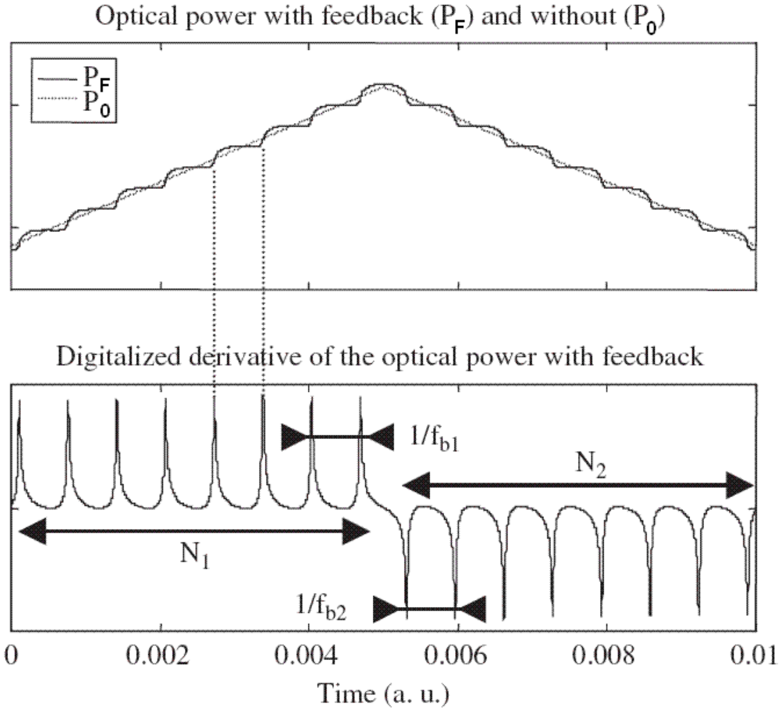

Fig. I:12 Integer number of optical power variations and their corresponding beat frequencies for a triangular injection current.

The simple pulse counting method is adequate to demonstrate the feasibility of absolute distance measurement with a self-mixing sensor. The maximum error on distance measurement is given by c/(2Δν) that corresponds to a ±1 pulse uncertainty per semi-period of modulation. This error depends directly on the wavelength (or frequency) shift of the laser source, without mode hopping. Considering a typical Fabry-Perot laser diode like the LD64110N continuously tunable up to 36 GHz without mode hops, the obtained resolution was around 4 mm for distances up to 3 m [65]. Accuracy improvement up to 0.5 mm at a distance of 60 cm has been achieved with a sensor based on a 3-electrodes distributed Bragg reflector (DBR) laser structure with a wide continuous optical frequency excursion of 375 GHz [66].

However to ameliorate the accuracy of self-mixing range finders, “beat frequencies” f_b between the pulses of the upward and downward triangular signal (Fig. I:12) have to be determined as the distance is then given by the following exact relationship [67]:

$$D=\frac{c}{4(d\upsilon/dt)}(f_{b1}+f_{b2}) \text{ or possibly } D\approx\frac{cT}{8\Delta\upsilon}(f_{b1}+f_{b2}) \qquad (1\text{-}27)$$

where ν is the optical frequency.

This method has a theoretical null error and for the considered case of a stationary target, f_{b1} is equal to f_{b2} in theory. In the perspective of designing a low-cost rangefinder achieving a resolution similar to the set-up designed with the DBR laser, this method is of great interest but its experimental implementation is rather complicated. As an example, first published results report an accuracy of only 2 cm from 0.25 cm to 2.35 m [67].

Another method has also been proposed that is based on FFT and reports to have better performance than the traditional peak spacing methods [68]. Such a range finding system has been built using a VCSEL and the FFT to measure a range of distances from 20 cm to 1 m with a maximum error of 1.5% and a resolution of 5 mm.

I.3 Conclusion

In this chapter, the theory of self-mixing was introduced showing its advantages for different sensing applications such as displacement or velocity measurements.

One of the main advantages of this type of sensors is the simplicity of the system that is being simplified more and more by using new light sources. For example, VCSELs present a low threshold current ideal for embedded systems. New self-mixing VCSEL sensors are now being conceived without a photodiode where the variations of the OOP are monitored by looking directly at the changes of the voltage across the laser diode itself [15]-[16]. Furthermore, these vertically emitting laser SM sensors that do not use photo-diodes can be used to grow two-dimensional sensor arrays for flow cartography. For example, a self-mixing imaging sensor using a monolithic VCSEL array with parallel readout has been published in 2009 [69].

First commercialized self-mixing sensors have already been launched by Philips through their

"Twin-Eye" laser sensor adopted by different computer mouse manufacturers such as the new high resolution A4tech gaming mouse or the Logitech V400 mouse [70]. This same sensor was initially designed by Philips for its possible use in mobile phones [71], PDAs or laptop computers in order to reduce the size and price occupied by usual inputs such as touch screen, mechanical joysticks or touch pads.

As a conclusion, self-mixing is an emerging technique which is newly commercialized, proving its interest in terms of cost and simplicity for future mass-market applications ranging from medicine to transportation.

The following chapters shall present the work undertaken to develop advanced displacement measurement techniques by using the self-mixing interferometry. We shall present new signal processing techniques used either to reduce the calculation time needed for displacement reconstruction (e.g. the hybrid displacement optimisation algorithm) or to improve the displacement measurement accuracy (e.g. the detection and correction of SM fringe disappearance in case of increased feedback) or to improve the adaptability of displacement reconstruction in case of SM feedback regime change (e.g. the adaptive SM fringe transition detection algorithm). Likewise, we shall present the results of the use of hardware components (adaptive optics in the shape of a liquid lens as well as a solid-state accelerometer coupled with the SM sensor) that have been added to the standard minimal sensor set-up (LD package with a focusing lens) in order to have better range, accuracy and robustness.

II Ameliorations in SM Displacement Algorithm

The use of SM for the case of displacement measurement has already been presented in the introductory chapter. The first measuring technique has been the fringe counting method but there exist various other methods that allow even better resolution as detailed in the introductory chapter.

The present thesis started with the objective of implementing a displacement measurement technique that would provide a resolution better than the basic half-wavelength and that could be used to develop a real-time displacement sensor that would be robust to changes in optical feedback regime and unfavorable operating conditions. This present work thus followed the important research work done in the field of SM signal processing [39]-[42] by a doctorate student of our research laboratory [72]. Among the various published methods, it was decided to base this work on the Phase Unwrapping Method (PUM) [39].

The advantage that this method holds over the others is the fact that these other methods require approximation and local Photodiode output signal linearization and/or external optical components and/or preliminary separate measurements of two fundamental SM parameters, namely 1) the feedback coupling factor C and 2) the linewidth enhancement factor α [35]-[34], [43]. These different methods can thus be more costly and are not fully compatible with real-time displacement measurements, all of which drastically reduces the interest of using SM sensors for industrial applications. PUM, however, has none of these constraints and has the added advantage of correctly approximating the C and α parameters.

So, the present work started by dissecting the PUM so as to have a faster and robust algorithm that could be used in a real-time system on chip. This detailed study presented its own results that demanded subsequent modifications. Thus, this chapter starts by presenting the PUM, followed by the work done to improve the algorithm.

II.1 Phase Unwrapping Method

PUM is a signal processing method for an adaptive estimation of the target displacement using a LD SM sensor in moderate feedback regime. The various operations of the signal processing are illustrated in Fig. II:1 and can be split up into two principal steps [39]. These shall be further elaborated after a basic theoretical development.

Let *D(t)* represent the displacement between the LD driven by a constant injection current and a remote surface which back-scatters a small amount of optical power back into the LD cavity. When this optical feedback phenomenon occurs, the laser wavelength is no longer the constant λ_0 but is slightly modified and becomes a function of time $\lambda_F(t)$ when *D(t)* varies (where the subscript ‘F’ denotes Feedback and ‘0’ denotes No feedback). The wavelength fluctuations can be found by solving the phase equation (1-16):

$$\nu_F - \nu_0 + \frac{C}{2\pi\tau_{ext}} \sin(2\pi\nu_F\tau_{ext} + \arctan\alpha) = 0 \qquad (2\text{-}1)$$

$x_F(t)$ and $x_0(t)$ represent two phase signals written as a function of the wavelengths $\lambda_F(t)$ and $\lambda_0(t)$, respectively.

$$x_F(t) = 2\pi \frac{D(t)}{\frac{\lambda_F(t)}{2}} = 2\pi\nu_F(t)\tau\ (t) \qquad (2\text{-}2)$$

$$x_0(t) = 2\pi \frac{D(t)}{\frac{\lambda_0(t)}{2}} = 2\pi\nu_0(t)\tau\ (t) \qquad (2\text{-}3)$$

So, (2-1) becomes:

$$x_0 = x_F + C\sin(x_F(t) + \arctan\alpha) \qquad (2\text{-}4)$$

$$x_0 = G\left[x_F(t); C, \alpha\right] \qquad (2\text{-}5)$$

The equations (2-4) and (2-5) thus indicate that the free running phase can be found by correctly estimating $x_F(t)$, *C* and α.

Furthermore, (2-3) indicates that once (2-5) is resolved, we can determine *D(t)* by

$$D(t) = x_0 \frac{\lambda_0}{4\pi} \qquad (2\text{-}6)$$

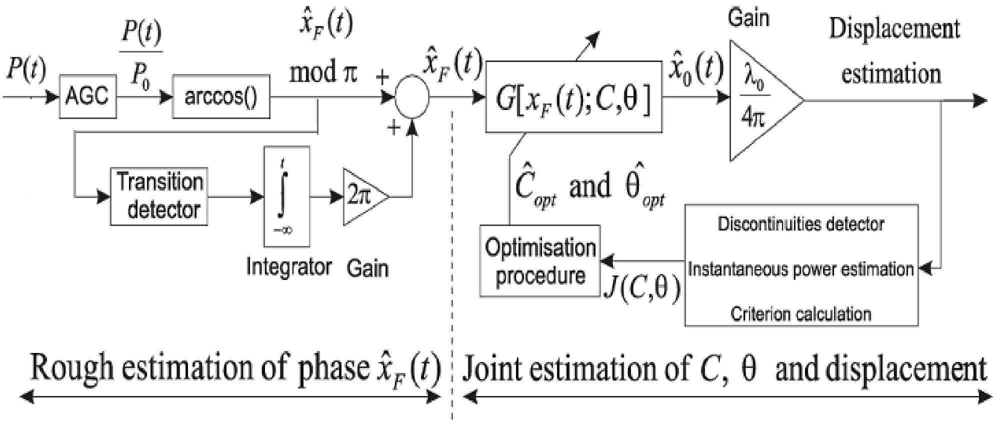

Fig. II:1. Block diagram of the signal processing for the estimation of the displacement using the Phase Unwrapping Method.

So, we can resume by stating that the displacement measurement for a constant current injection diode under self-mixing can be achieved by correctly estimating the three parameters, namely: the phase under feedback, C and α.

Let us start by estimating the phase under feedback $x_F(t)$.

II.1.1 Rough Estimation of Phase

Using (2-2) in (1-21) that gives the laser diode optical output power OOP, we arrive at

$$P(t)=P_0\,(1+m_{\text{mod}}\cos(x_F(t))) \tag{2-8}$$

P(t) is then brought into the range [1 –1] to give the normalised OOP *P'(t).* Then, using (2-8), we can easily retrieve “ $\hat{x}_F(t)$ $_{\text{mod } \pi}$”, which is the modulus π phase under feedback:

$$\hat{x}_F(t)_{\text{mod } \pi}=\arccos(\,P'(t)) \tag{2-9}$$

Now, according to [73] and [74], each of the discontinuities seen in “ $\hat{x}_F(t)$ $_{\text{mod } \pi}$” represents a phase jump of 2π. So, by adding or subtracting 2π at each of these phase shifts, we can estimate $\hat{x}_F(t)$. In fact, it is this operation of unrolling or unwrapping the phase around each phase shift (or Self-mixing fringe) that has led to the name of PUM.

The rough feedback phase reconstruction is thus elaborated in Fig. II:2, where (a) presents the normalised OOP *P'(t),* (b) shows the corresponding “ $\hat{x}_F(t)$ $_{\text{mod } \pi}$”, (c) indicates how a simple derivative helps to identify SM fringes, where as (d) is the roughly estimated phase $\hat{x}_F(t)$.

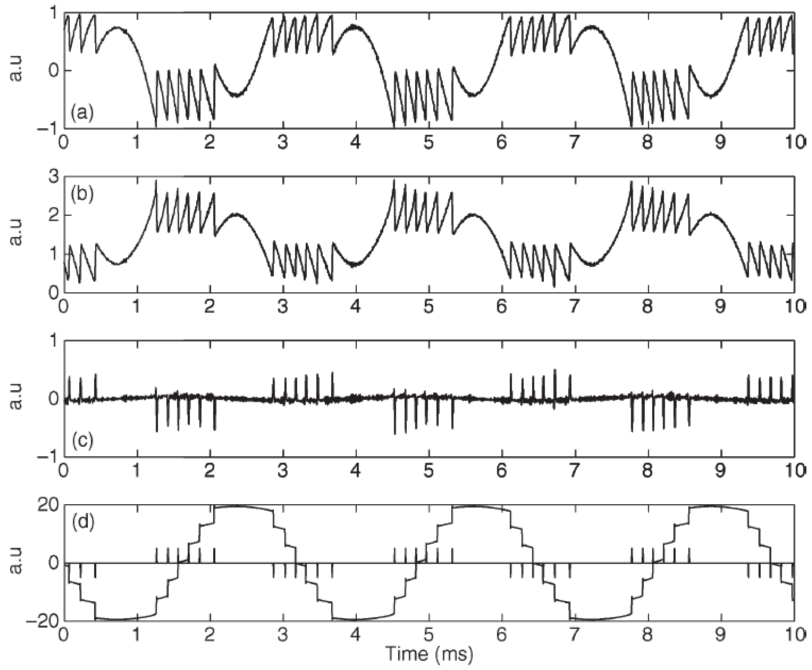

Fig. II:2 First step of the algorithm is the unwrapping of the phase estimation. (a) Normalized OOP P'(t), (b) " $\hat{x}_F(t)$ *mod* π*", (c) derivative of "* $\hat{x}_F(t)$ *mod* π*", and (d) Transitions and rough reconstruction of* $x_F(t)$*.*

If we compare the result of this rough phase estimation with the method of fringe-counting then it is evident that a simple detection and subsequent accumulation (as shown in Fig. II:2, (c)) would give the same result as that given by fringe counting. However, $\hat{x}_F(t)$ (shown in Fig. II:2, (d)) is more precise than a simple fringe counting and hence closer to the actual target displacement as it is calculated by the addition of "$\hat{x}_F(t)$ mod π" to the value obtained by the simple fringe-counting.

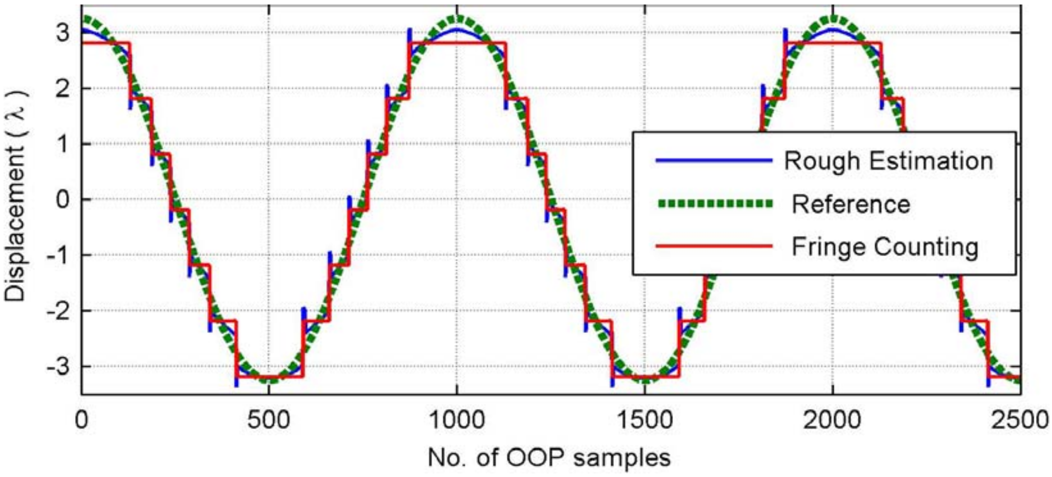

Fig. II:3 The result provided by the rough estimation and the fringe counting for a simulated reference target displacement of 6.5(λ/2) and C=1.5.

The same result can be observed in Fig. II:3 where for a simulated target displacement of 3.25λ and C=1.5, the rough estimation provides a result of 3.05λ where as fringe counting has a result of 2.817λ at the signal maxima. It can also be noticed that the rough estimation, though better than the fringe counting, is still inaccurate with respect to the true target displacement.

This rough estimation would be optimised in the next step to further match the actual target displacement.

Now, once $\hat{x}_F(t)$ is estimated, we need only estimate C and α in order to resolve (2-4).

II.1.2 Joint Estimation of C and α

The second signal processing step deals with the joint estimation of C, α, and $D(t)$. It is based on the idea that target displacement discontinuities are far less frequent than discontinuities of $P(t)$ and $x_F(t)$ caused by the non-linear behaviour of (2-4) and (2-7).

As $\theta = x_F(0) + \arctan(\alpha)$ remains constant, so (2-4) becomes

$$x_0 = x_F + C\sin(x_F + \theta) \qquad \forall \; t > 0 \qquad \text{(2-10)}$$

So, we can now choose an optimal set of parameters $\hat{C}_{opt}$ and $\hat{\theta}_{opt}$, that would lead to a discontinuities minimization of the reconstructed phase $\hat{x}_0(t)$ by using (2-10). This procedure thus helps to correct the roughness inherent in the 2π phase unwrapping used in the first step of the method.

It is also brought forward that as long as $x_F(0)$ is unknown, α can only be approximated. However, the influence of α on the shape of the SM signal remains secondary and has no important consequence on the displacement measurement with PUM.

$\hat{C}_{opt}$ and $\hat{\theta}_{opt}$ are given by the optimisation of a criterion $J(C, \theta)$, which is written as [39]

$$J(C,\theta) = \sum_{k=0}^{K} [\hat{x}_0(k) - \hat{x}_0(k-1)]^2 \qquad \text{(2-11)}$$

where $\hat{x}_0(k)$, $k \in \mathrm{N}$, is the discrete form of the phase $x_0(k)$. The criterion is evaluated over a temporal window containing K points of the time derivative of $\hat{x}_0(k)$. Hence the optimal couple $\hat{C}_{opt}$ and $\hat{\theta}_{opt}$ is the one which minimises $J(C,\theta)$ in order to allow the reconstruction of optimal displacement:

$$\underset{C,\theta}{Arg\min}[J(C,\theta)] = Arg\min \sum_{k=0}^{K} [\hat{x}_0(k) - \hat{x}_0(k-1)]^2 \qquad \text{(2-12)}$$

Fig. II:4 presents the criterion $J(C, \theta)$ for an experimental SM OOP signal. The minimum point found in the function space leads to the approximation of the couple(C, θ). These values are then used in (2-10) to finally calculate $x_0(t)$ which leads to $D(t)$.

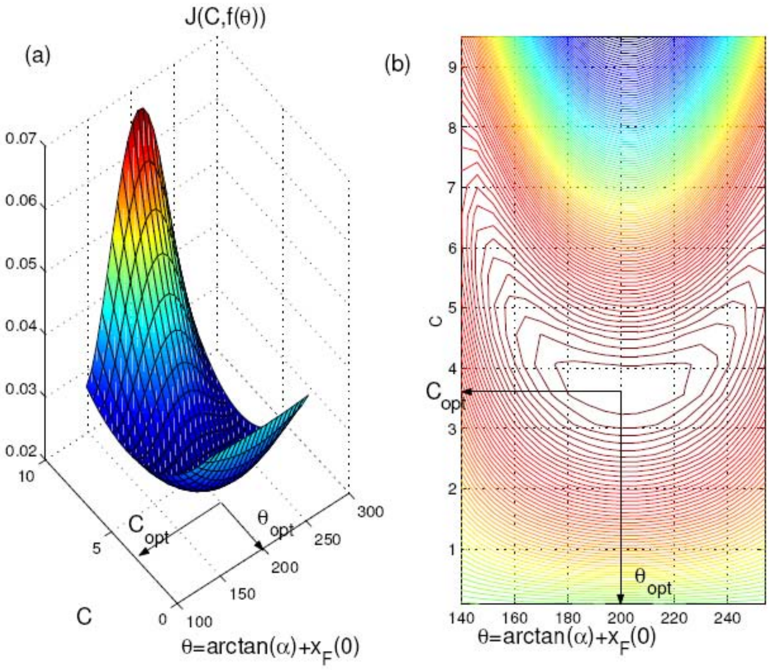

Fig. II:4 The criterion $J(C,\theta)$ corresponding to an experimental SM OOP signal, that allows the estimation of the (C,θ) couple.

II.1.3 Conclusion

As stated previously, an objective of this thesis was the design of a SM displacement measurement technique that could be implemented as a sensor on chip. The choice of the PUM seemed appropriate as a starting block as it catered to the most usually encountered SM signals in free space i.e. moderate regime signals while giving a precision of around $\lambda/16$ for experimental acquisitions.

So, after a detailed study of PUM, it came to light that the most time-consuming and complex step remained the joint optimization procedure (shown in Fig. II:1). As presented in the last section, it consists in the minimization of a multivariable space (Fig. II:4), which in itself is based on nonlinear mathematical equations.

Now that an introduction to the SM interferometry as well as to the PUM has been presented, the rest of the manuscript will present the research work undertaken during this thesis. Thus, by the help of the solid grounding provided by previous research, the author shall from now on detail his endeavors that take forward the research work in the field of SM interferometry.

Let us begin with the next section, where an approach will be presented that would replace the before mentioned optimisation process by a Fourier transform based technique.

II.2 Fourier Transform based Phase Retrieval

As the optimization needed for the Phase-Unwrapping method turns out to be time-consuming so the method of arriving at the displacement *D(t)*from the self-mixing optical signal *P(t)* was re-evaluated.

Then, it became apparent that the first step of rough phase estimation does not need complicated calculations and it may be used as a basis to arrive at the final phase without going through the time-consuming joint-optimization step. This can be seen in Fig. II:5 where the final phase achieved by the optimization is shown alongside the roughly estimated phase. It is observed that the optimization results in the smoothing out of the higher frequency components of the rough phase and eliminates the stair-case shape of the roughly estimated phase.

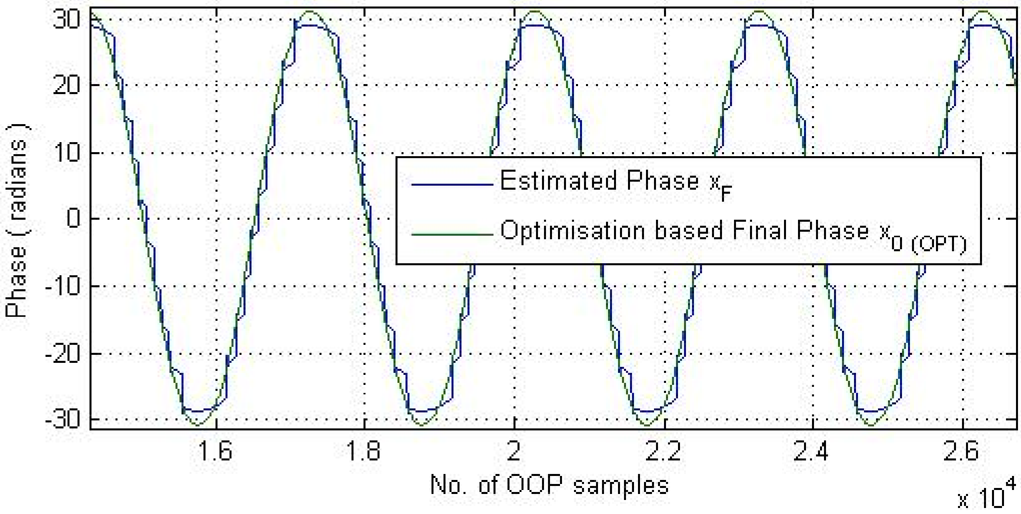

Fig. II:5. The estimated phase x_F obtained after the rough estimation and the final phase $x_{0(OPT)}$ based on the Nelder-Mead optimization of the rough estimation.

This led to the idea of analyzing the frequency spectrum of the rough phase by doing a FFT and using only the frequency component related to the target oscillation frequency (called f_{base}) while rejecting all the other frequency components.

Thus, once the right component is selected, the Inverse FFT may reproduce the final phase, which can be used to calculate the displacement.

So, the PU method has been modified to replace the joint-optimization step with the FFT based analysis of the Power Spectral density (PSD) of the rough phase, followed by the selection of the frequency component having the highest Power (which gives us f_{base}), and the subsequent recreation of the final phase using an IFFT, as shown in Fig. II:6.

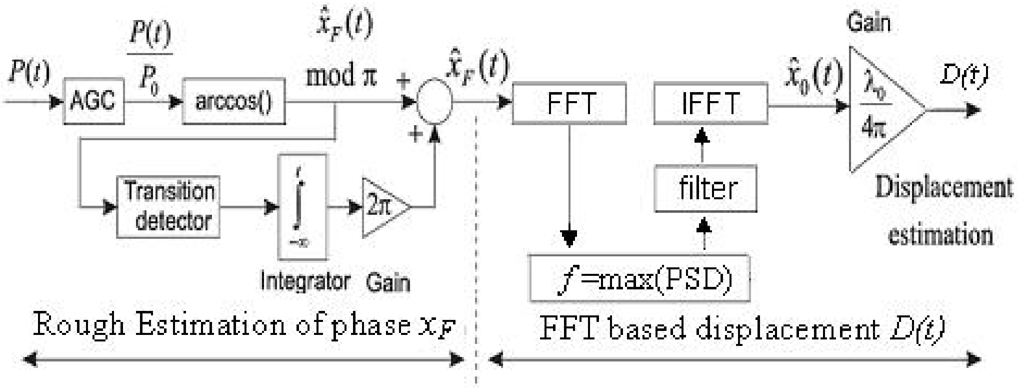

Fig. II:6. Fourier Transform based Phase Retrieval Algorithm

To present the working of this FFT based algorithm, a simulated Self-mixing signal for a target excitation frequency of 333Hz and a target excitation amplitude of 10*(λ/2) has been used. The PSD of the roughly estimated phase is presented in Fig. II:7 where, the highest Power density is found for the FFT signal corresponding to f_{base} = 335Hz. Thus, once selected, only f_{base} component is retained in the FFT signal and all the rest are rejected by using the filter block shown in Fig. II:6.

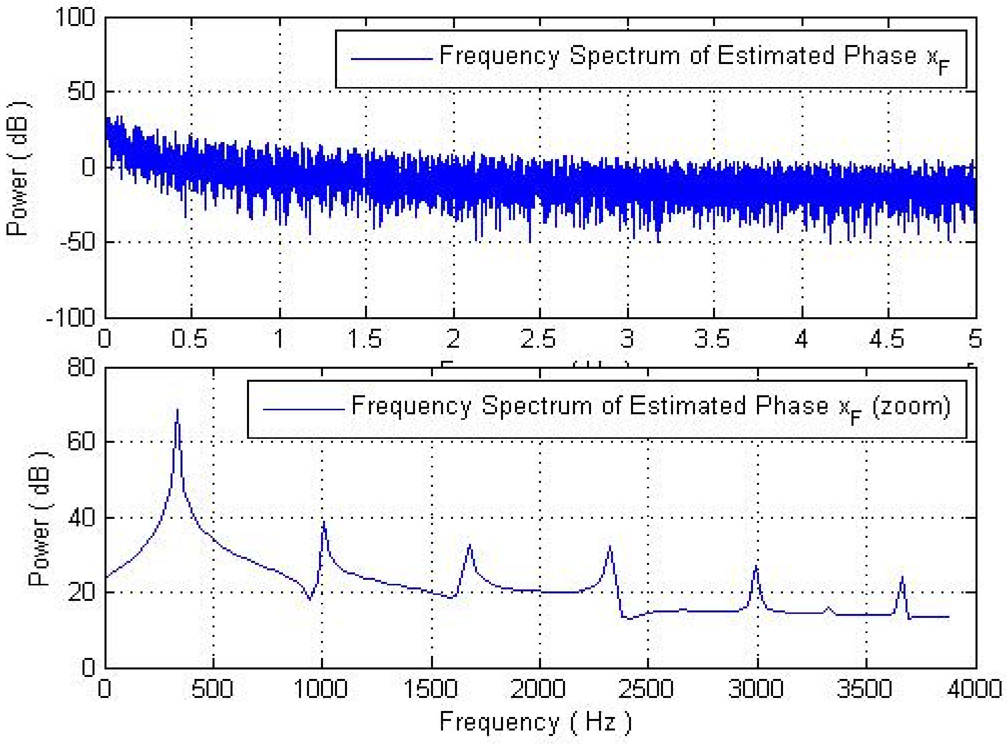

Fig. II:7. The Power density of the frequency spectrum of the estimated phase x_F where the maximum peak is found for 335Hz.

Inverse FFT (IFFT) is finally performed on the filtered FFT signal to retrieve the final phase based on FFT analysis of the rough phase. Fig. II:8 presents these two signals, where it is observed that the FFT based phase $x_{0(FFT)}$ faithfully reproduces the target oscillation frequency and the amplitude of the reproduced signal closely matches that of the rough phase.

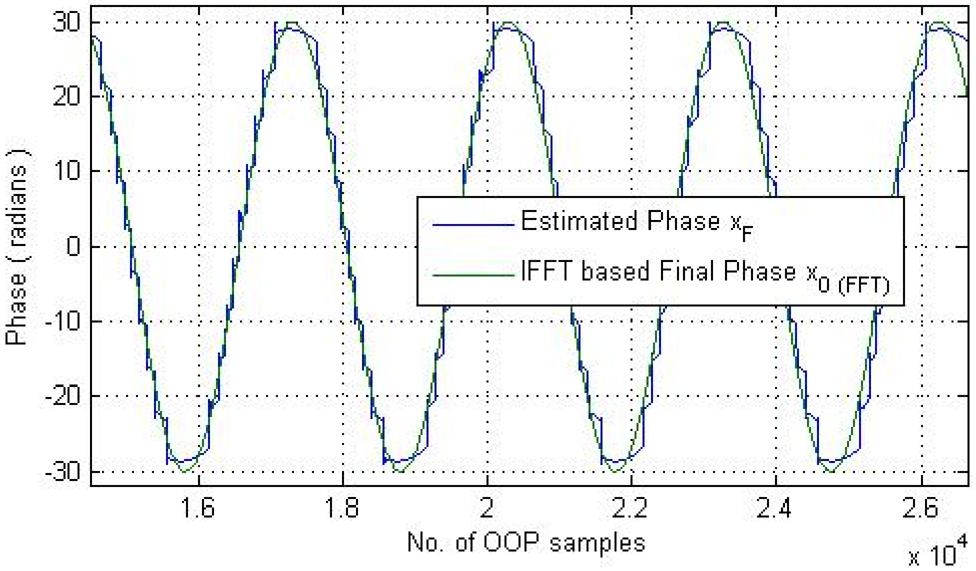

Fig. II:8. Final phase $x_{0(FFT)}$ *obtained by using IFFT on only the maximum power density frequency component of the FFT signal of estimated phase* x_F.

However, once the displacement value is calculated based on $x_{0(FFT)}$, the error as compared to the target excitation signal is larger as compared to the error obtained by the displacement calculated by using joint optimization based final phase $x_{0(OPT)}$. Fig. II:9 shows these curves where an error of 3.8% is seen for the FFT based algorithm whereas the error is of 0.3% for the PU method.

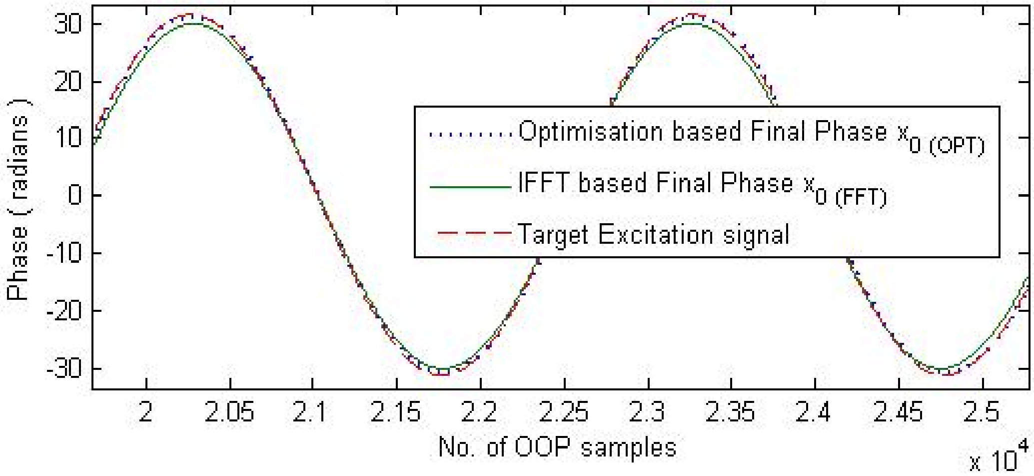

Fig. II:9. IFFT based final phase $x_{0(FFT)}$ *and Optimisation based final phase* $x_{0(OPT)}$ *for a target excitation signal of* $10*\lambda/2$.

Thus, despite its simplicity and the correct calculation of the target oscillation frequency, the FFT based algorithm cannot be used for a displacement measurement implementation, as the increased error in displacement calculation cannot be acceptable.

II.3 Adapted Nelder-Mead Algorithm

As the higher accuracy of PUM as compared with the FFT based method comes from the joint-optimization step, so a detailed study of this process was undertaken in order to possibly optimize this step.

So, in this section, we explain the signal processing required for the joint estimation of C and θ in order to reach a λ/16 precision of displacement measurement. The said optimization is based on the use of the Nelder-Mead simplex method that has been consequently modified to better suit our application. This analysis leads to optimize the number of optical power samples necessary for joint estimation as well as to the adaptations of Nelder-Mead method, all of which result in an important reduction in computing time necessary for convergence to the optimum values [75]. Furthermore, influence of initial step size parameter η on the reduction in the convergence time as well as on the possibilities of introducing parallelism in the method have been studied for implementation in a future integrated sensor [76].

Thus, in this section, the Nelder-Mead simplex method is presented followed by the application of its adapted version to the PUM, the influence of η and finally the implementation of the algorithm in Stateflow® and VHDL.

II.3.1 The Nelder-Mead Simplex Method

The Nelder-Mead Simplex Method (NM) [77] is one of the most widely used direct search methods for multidimensional unconstrained minimization and non-linear optimisation. It attempts to minimize a scalar-valued non-linear function of n real variables using only function values, without any derivative information (explicit or implicit). The NM method thus falls in the general class of direct search methods.

A large subclass of direct search methods, including the NM method, maintain at each step a non-degenerate simplex; a geometric figure in n dimensions of nonzero volume that is the convex hull of $n + 1$ vertices (i.e. a pyramid in the case of 3D objective function). Each iteration of a simplex-based direct search method begins with a simplex, specified by its $n + 1$ vertices and the associated function values. One or more test points are computed, along with their function values, and the iteration terminates with a new (different) simplex such that the function values at its vertices satisfy some form of descent condition compared to the previous simplex. Among such algorithms, the NM algorithm is particularly parsimonious in function evaluations per iteration, since in practice it typically requires only one or two function evaluations to construct a new simplex. Several popular direct search methods use *n* or more function evaluations to obtain a new simplex [78].

The NM method is proposed as an algorithm for minimizing a real-valued function *f*(x) for $x \in \Re^n$. Four scalar parameters must be specified to define a complete NM method: coefficients of reflection (ρ), expansion (χ), contraction (γ), and shrinkage (σ). According to the original NM paper [77], these parameters should satisfy:

$$\rho > 0,\ \ \chi > 1,\ \ \chi > \rho,\ \ 0 < \gamma < 1,\ \ 0 < \sigma < 1 \qquad \text{(2-13)}$$

The nearly universal choices used in the standard NM algorithm are $\rho = 1, \chi = 2, \gamma = ½$ and $\sigma = ½$ which are also used in our method.

At the beginning of the *k*th iteration, $k \geq 0$, a non-degenerate simplex Δ_k is given, along with its *n* + 1 vertices, each of which is a point in $\Re^n$. It is always assumed that iteration *k* begins by ordering and labelling these vertices as $x_1^{(k)},\ldots,x_{n+1}^{(k)}$, such that

$$f_1^{(k)} \leq f_2^{(k)} \leq \ldots \leq f_{n+1}^{(k)} \qquad \text{(2-14)}$$

where $f_i^{(k)}$ denotes $f(x_i^{(k)})$. The *k*th iteration generates a set of *n* + 1 vertices that define a different simplex for the next iteration, so that $\Delta_{k+1} \neq \Delta_k$. Because we seek to minimize *f*, we refer to $x_1^{(k)}$ as the *best* point or vertex, to $x_{n+1}^{(k)}$ as the *worst* point, and to $x_n^{(k)}$ as the *next-worst* point. Similarly, we refer to $f_{n+1}^{(k)}$ as the worst function value, and so on.

A single generic iteration is specified, omitting the superscript *k* to avoid clutter. The result of each iteration is either (1) a single new vertex- the accepted point - which replaces x_{n+1} in the set of vertices for the next iteration, or (2) if a shrink is performed, a set of *n* new points that, together with x_1, form the simplex at the next iteration.

II.3.1.a An iteration of NM algorithm

Order. Order the *n* + 1 vertices to satisfy: $f(x_1) \leq f(x_2) \leq \ldots \leq f(x_{n+1})$.

Reflect. Compute the *reflection point* x_r from

$$x_r = \bar{x} + \rho(\bar{x} - x_{n+1}) \qquad \text{(2-15)}$$

where $\bar{x}=\sum_{i=1}^{n} x_i / n$ is the centroid of the *n* best points (all vertices except for x_{n+1}). We evaluate $f_r = f(x_r)$. For $f_1 \le f_r < f_n$, we accept the reflected point x_r and terminate the iteration.

Expand. If $f_r < f_1$, the *expansion point* x_e is calculated:

$$x_e = \bar{x} + \chi(x_r - \bar{x}) \tag{2-16}$$

and $f_e = f(x_e)$ evaluated. For $f_e < f_r$,we accept x_e and terminate the iteration; otherwise (if $f_e \ge f_r$), x_r is accepted and we terminate the iteration.

Contract. If $f_r \ge f_n$, perform a *contraction* between $\bar{x}$ and the better of x_{n+1} and x_r .

- **Outside.** For $f_n \le f_r < f_{n+1}$ (i.e., x_r is strictly better than x_{n+1}), we do an outside contraction:

$$x_c = \bar{x} + \gamma(x_r - \bar{x}) \tag{2-17}$$

and evaluate $f_c = f(x_c)$. For $f_c \le f_r$, x_c is accepted and we terminate the iteration; otherwise, we perform a shrink step.

- **Inside**. If $f_r \ge f_{n+1}$, perform an inside contraction:

$$x_{cc} = \bar{x} - \gamma(\bar{x} - x_{n+1}) \tag{2-18}$$

and evaluate $f_{cc} = f(x_{cc})$. For $f_{cc} \le f_{n+1}$, we accept x_{cc} and terminate the iteration; otherwise, we do a shrink.

Perform a shrink step. Evaluate *f* at the *n* points $v_i = x_1 + \sigma(x_i - x_1)$, where $i = 2,...,n+1$. The (unordered) vertices of the simplex at the next iteration consist of $x_1, v_2, ..., v_{n+1}$.

Fig. II:10 and Fig. II:11 show the effects of reflection, expansion, contraction, and shrinkage for a simplex in two dimensions (a triangle), using the standard coefficients [78].

The algorithm is run until the optimised point is reached which may be specified as the obeying the condition, $abs(f_1 - f_{n+1}) \le tol$ where '*tol*' is an infinitesimally small value, approaching machine-level precision for the hardware implementations of the algorithm.

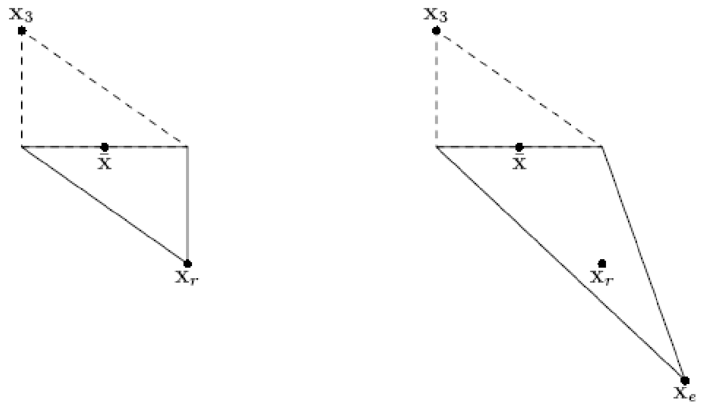

Fig. II:10. Nelder-Mead simplexes after a reflection and an expansion step. The original simplex is shown with a dashed line.

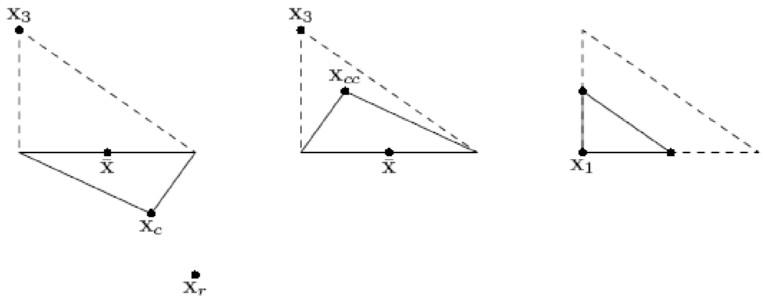

Fig. II:11. Nelder-Mead simplexes after an outside contraction, an inside contraction, and a shrink. The original simplex is shown with a dashed line.

II.3.1.b Application of the NM algorithm

Restricting the NM method to two dimensions (as only C and θ are being optimized), the number of vertices becomes 3 which can be ordered as B (best or the minimum point), G (good or the next minimum point) and W (worst or the highest valued point), such that $f(B) \leq f(G) \leq f(W)$. The iterations of the algorithm generate further points in 2D space, such as R (reflect), E (expand), C (outside contract), Ci (inside contract), S (shrink) or M (mid-point of B and G).

We observe that the NM method has an adaptive feature that enables the simplex (see Fig. II:12 for an example in two dimensions) to reflect, expand, contract or shrink so as to conform to the characteristics of the response surface.

These actions are based on the conditions summarized in the Table II-1 [79] and are applied repeatedly until a termination criterion is reached. For the particular case illustrated in Fig. II:12, reflection of point W (corresponding to the highest result) through the centriod M of the opposite side locates point R. In this instance, an expansion would then follow making the next simplex GBE.

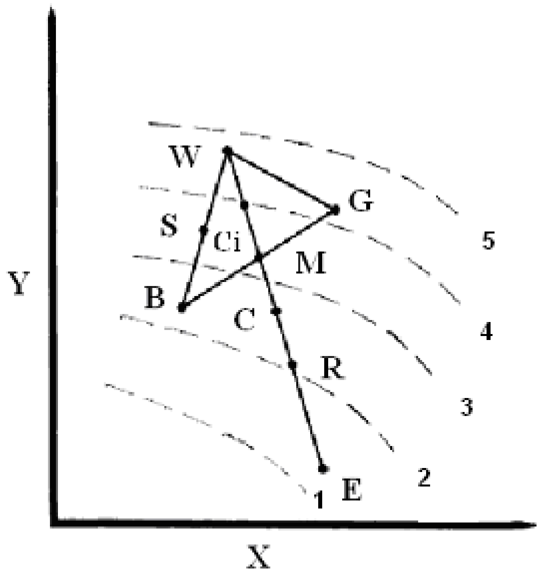

Fig. II:12 A Two Dimensional NM Simplex (triangle) on the XY surface with possible subsequent points (see Table II-1), where curves 5 to 1 represent descending values of the objective function [79].

In contrast to other minimization procedures, the simplex procedure approaches the minimum by moving away from high values of the objective function rather than by trying to move in a line toward the minimum [79].

Condition	**Action**	**New Simplex**
f(B) ≤ f(R) ≤ f(G)	Reflect	G B R
f(R) < f(B)	Extend	G B E
f(W) < f(R)	Inside Contract	G B Ci
f(G) < f(R) ≤ f(W)	Outside Contract	G B C
f(W) ≤ f(Ci) or f(R) ≤ f(C)	Shrink	S M B

Table II-1. Conditions governing the formation of subsequent simplexes (where f(x) designates the value of the objective function at point x).

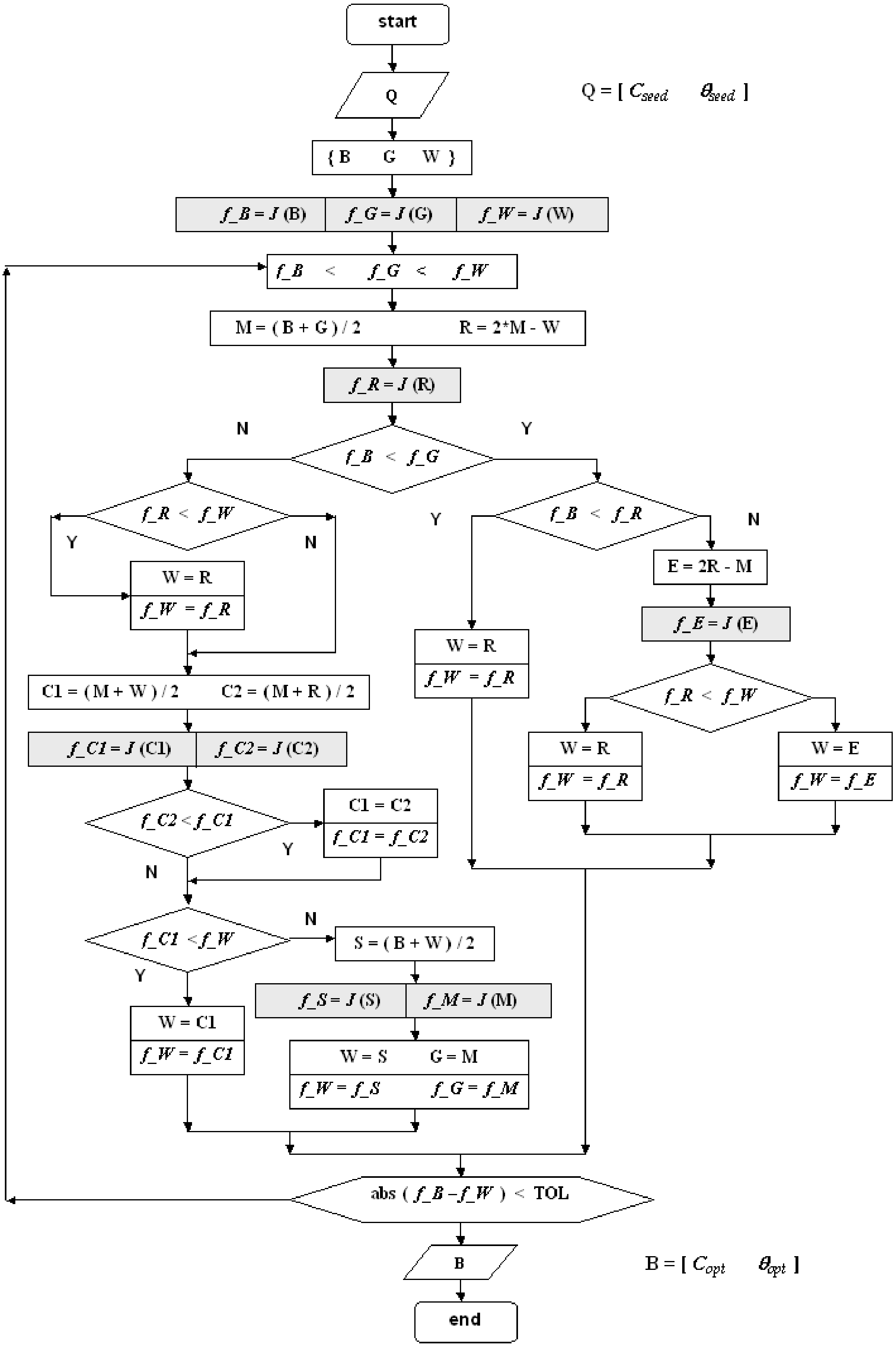

Fig. II:13. Schematic diagram of the Nelder-Mead simplex algorithm for joint optimisation of C and θ. The shaded blocks represent an objective function call to one of the standard NM steps.

II.3.2 Application to the Self-Mixing Signal

Let us rewrite the condition for the optimization of the couple *(C, θ)* using the criterion *J(C, θ)*:

$$\underset{C,\theta}{Arg\min}[J(C,\theta)] = Arg\min\sum_{k=0}^{K}[\hat{x}_0(k) - \hat{x}_0(k-1)]^2$$

As the criterion is evaluated over a temporal window containing *K* sampled points, so K has a direct influence on the total time needed to converge.

Secondly, every time the value of *C* or *θ* is varied, the equation $x_0(k) = x_F(k) + C\sin\left[x_F(k) + \theta\right]$ (denoted from hereon as the 'Objective Function') has to be recalculated so that its value may be inserted into *J(C, θ)*. So, a change in *C* or *θ* results in a new Objective Function Call, necessitating a recalculation of *K* corresponding sampled points. Thus, reducing the number of Function Calls shall lead to a direct reduction in the total computation time.

II.3.2.a Reduction of the Number of Samples

It has been observed during the optimization of the PUM that the window size of *K* points in time domain can be drastically reduced to one-third or even one-fourth size with only a cost of less than 5% error in the accuracy of the $\hat{C}_{opt}$ and error of less than 1% in the estimation of $\hat{\theta}_{opt}$. The evolution of %age error in $\hat{C}_{opt}$ and $\hat{\theta}_{opt}$ as against the window size can be seen along the y-axis of Fig. II:14 respectively. Thus, considerable gain in the speed of execution of the algorithm can be achieved without an excessive error in the evaluation of the desired parameters.

II.3.2.b Influence of the Tolerance Parameter

During the optimizations, the influence of the tolerance parameter '*tol*' was also observed. Actually, it is the parameter that defines when the optimization process should stop. This parameter actually helps to finally identify *the final optimized point* obtained in the multidimensional simplex space. Thus, it ensures the proximity of *n +1* vertices as to when they are sufficiently close to terminate the execution of the NM iterations.

Hence, with a very small '*tol*' value, the NM algorithm continues to evaluate the objective function for a long period of time (i.e. increased number of iterations and objective function evaluations) as opposed to a small period of time for a relatively large *'tol'* value.

This parameter is theoretically close to zero and is normally set close to machine precision level in the commercial software adaptations of NM method in order to ensure the validity of the 'minimum' reached by the NM method. However, in our case, the influence of '*tol*' has been evaluated with a range from 10^{-1} to 10^{-9}. The objective has been to adapt this parameter value in order to decrease the number of function evaluations while maintaining the same levels of accuracy of $\hat{C}_{opt}$ and $\hat{\theta}_{opt}$. It is observed that with a value close to 10^{-3}, the number of objective function evaluations are approx. halved while maintaining the error induced in $\hat{C}_{opt}$ and $\hat{\theta}_{opt}$ to less than 0.5%, as seen along the x-axis of Fig. II:14 respectively.

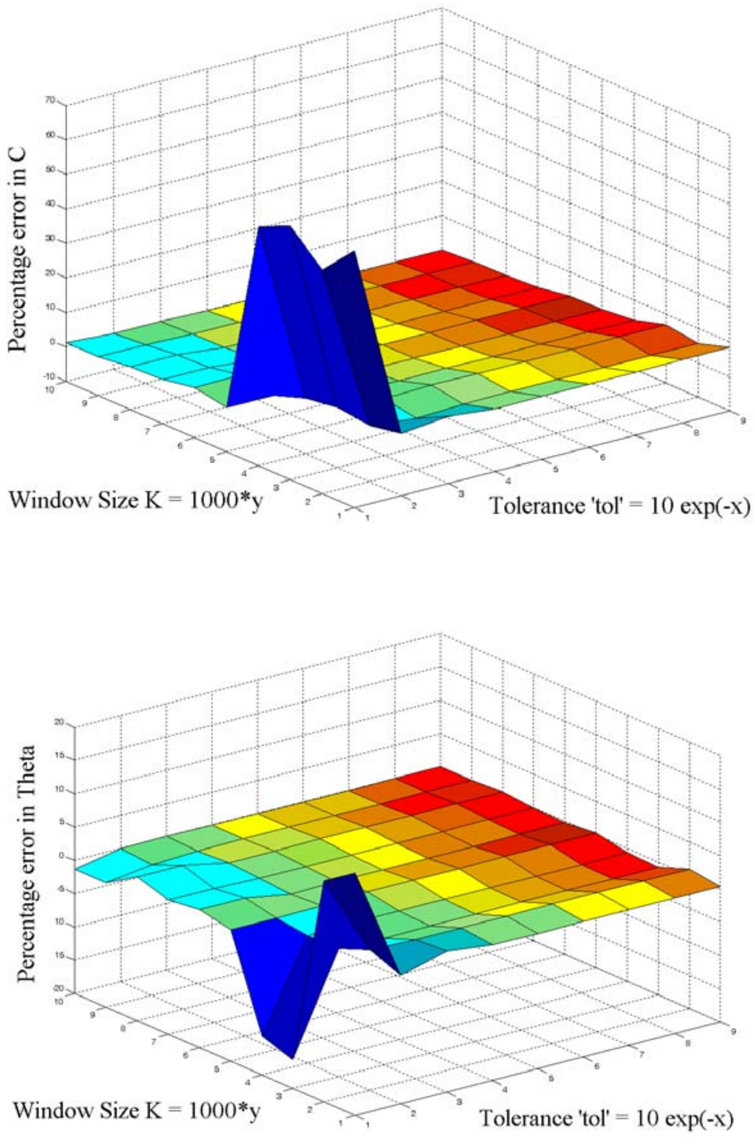

Fig. II:14. Percentage error in $\hat{C}_{opt}$ and $\hat{\theta}_{opt}$ as a function of Tolerance 'tol' of NM method (x-axis) and Window size K of $J(C,\theta)$ (y-axis). The color coding represents the number of objective function utilisations which increases from 8 (blue) to 104 (red) as a function of x and y.

II.3.2.c Redundant Contraction Step

Lastly, the NM method was adapted to our displacement measurement application with respect to its contraction steps.

As already explained, the NM method utilises two types of contraction, the inside contraction as well as the outside contraction. However, it has been observed that the removal of the 'inside contraction' step actually helps to decrease the number of objective function calls by approx. 25% (Fig. II:15) as far as its adaptation to our application is concerned. It is noted that this factor gain is achieved without any error introduced in the joint estimation of $\hat{C}_{opt}$ and $\hat{\theta}_{opt}$.

This can be explained by the fact that our objective function is in two-dimensional space and the general shape of the criterion $J(C,\theta)$ is a parabolic valley (Fig. II:4) in 3 dimensions, where the utilisation of 'inside contraction' would normally lead to a new vertex leading away from the optimal point which is an undesirable result.

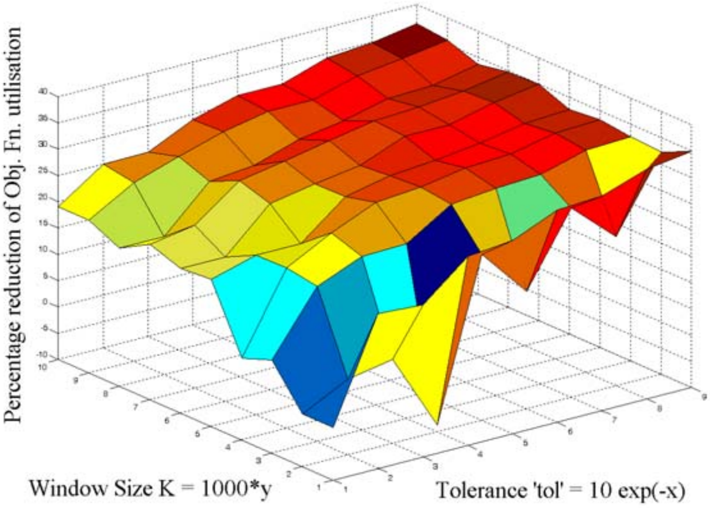

Fig. II:15. Percentage reduction in objective function utilisation without using 'inside contraction' step of NM method as a function of Tolerance 'tol' (x-axis) of NM method and Window size K of $J(C,\theta)$ (y-axis). The colour coding represents the same percentage error.

Even though the three steps mentioned before have resulted in a gain in the calculation time but the total time needed in the optimisation still remains quite long. Furthermore, the iterative but sequential nature of NM makes it quite difficult to parallelize the method. Hence, further work was undertaken to still improve the optimisation time. This is specifically based on the reduction of the total number of objective function calls by effectively using initial step size parameter of the NM method. Introducing parallelism, as seen in the next section, can then reduce the overall computing time in NM iterations.

II.3.3 The Step-size Parameter η

The initial step size parameter η is used to initialise the starting simplex in the Nelder-Mead Simplex method. This simplex (a triangle in 2D space and a Pyramid in 3D space) is constructed based on an arbitrary initial point in the simplex space. The required $n + 1$ points needed to create a simplex for an n variable function are thus derived based on the value of η.

Thus, for an initial starting point q_{seed}, the other n points can be found using

$$q_{seed} = q_{seed} + \eta e_i \qquad (2\text{- }19)$$

where the e_i's are N unit vectors in the simplex space and where η is a constant which is a guess of the objective function's characteristic length scale.

II.3.3.a Influence of η on Total No. of Objective Function Calls

It has been observed by simulations on the experimental OOP data that this parameter has direct effect on the time needed to find the optimum values (in our case, the values of C and θ that minimize our objective function or the criterion $J(C, \theta)$) through the Nelder-Mead Method.

X AXIS	[C Theta]
1	[2 2]
2	[2 4]
3	[2 8]
4	[4 2]
5	[4 4]
6	[4 8]
7	[8 2]
8	[8 4]
9	[8 8]

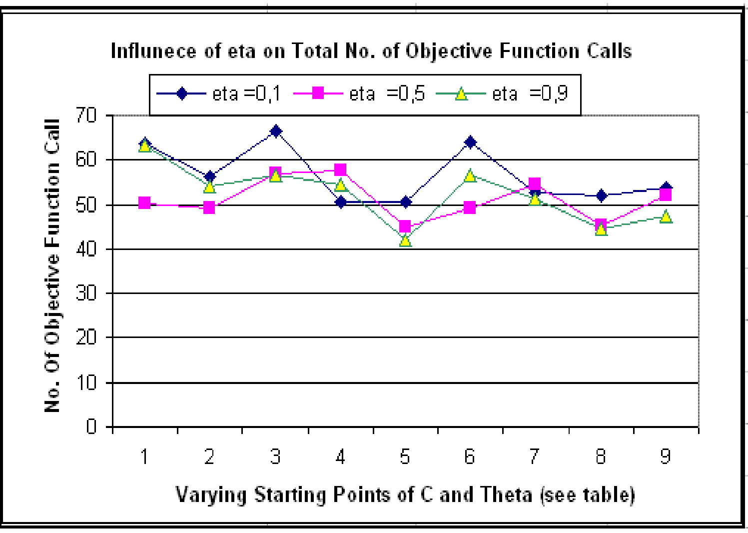

Fig. II:16. Influence of η on the total number of objective function calls needed in order to converge to the optimised values of C and θ for varying starting points of the same two parameters (i.e. $q_{seed} = [C_{\text{seed}}\ ,\ \theta_{\text{seed}}\ ]$) in Nelder-Mead Simplex Algorithm.

The simulations have been conducted using three different values of η, e-g η = 0.1, η = 0.5 and η = 0.9.

In order to study only the influence of η, the starting values were varied in the objective function space so that its influence on the final convergence can be evened out.

For each starting point e-g $C = 4$ and $\theta = 4$ etc, 90 simulations were carried out for varying tolerance factor '*tol*' and total number of Laser Diode Power samples *K*. The averaged total number of objective function calls for these 90 simulations for a given starting point $q_0 = [C_0 , \theta_0]$ was used.

Thus, using the same method, averaged numbers of objective function calls were calculated for 9 different starting points and the resulting curves are plotted in Fig. II:16. The same practice has been used for all subsequent data based on varying starting points.

The varying starting points have been selected keeping in mind the usual variation of C and θ for the case of moderated feedback in a self-mixing laser diode.

If the mean of these curves is taken, it is seen in the Table II-2 that for $\eta = 0.5$, the total number of objective function calls is minimized as compared to other values. This in turn shall lead to a quicker establishment of optimised values of C and θ for our phase-unwrapping algorithm of displacement measurement using the Nelder-Mead Method.

η	0.1	0,5	0,9
Objective function Calls	56.6	51	52.3

Table II-2. The mean of total number of objective function call values shown in Fig. II:16 .

II.3.3.b Percentage Distribution of Standard NM steps for varying η

Simulations on the same experimental OOP data have been carried out to measure the percentage distribution of the standard NM step related function calls (Reflect, Expand, Contract and Shrink) in the over all number of function calls.

It has already been presented that in any given NM iteration, one step out of the standard four steps; "*reflect, expand, contract and shrink*" is chosen. (Please see Fig. II:13 where the shaded blocks represent the Standard NM steps).Thus, every new iteration begins by a call to the reflect step (*f_R*), followed by a call to the expansion step (*f_E*) or iteration termination in one case (i.e. the right hand side of the iteration loop shown in Fig. II:13) OR a call to the contraction step (*f_C1 and f_C2*) and/or a call to the shrinkage step (*f_S and f_M*) in the other case (i.e. the left hand side of the iteration loop shown in Fig. II:13).

Thus, an averaged percentage distribution can be assumed to contain 50 % reflection function calls and 25% each for expansion as well as contraction-shrinkage function calls.

However, these percentages can be altered depending on the function space topography, its initial starting point as well as the parameter η.

In Fig. II:17 are given the percentage distributions for 3 different values of η for the 9 different starting points while using the same experimental OOP signal.

It is observed that the reflect step percentage is always close to 50 irrespective of the value of η, where as the percentages for contract and expand steps vary according to η. The shrink percentage remains close to zero.

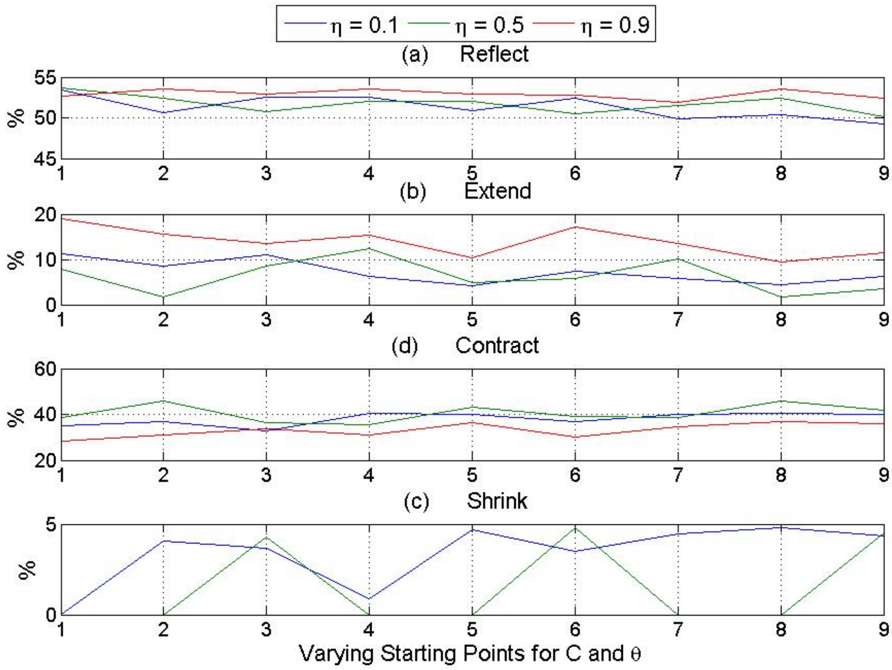

Fig. II:17. Percentage distribution of the four basic NM steps Reflect (a), Extend (b), Contract (c) and Shrink (d) in the total number of objective function calls for varying η and starting points.

II.3.3.c Influence of η on the Shrink Step

The number of Shrink Step function calls can also be controlled by varying the parameter η. This can be seen in Fig. II:17 representing percentage distributions of the four standard NM steps. For example, for η = 0.9, the vertices of the created simplex are fairly close and a shrink step is never needed.

The averaged shrink step function call percentage for different starting points is given below. Once again, a very small value is seen for η = 0.5.

The advantage of a very small shrink function call percentage is that its elimination leads to elimination of two function calls per iteration (shown as *f_S* and *f_M* in Fig. II:13) for an objective function in 2D space. Thus for any arbitrary NM iteration, only 3 out of 5 next function calls (*f_R*, *f_E* or *f_C* in Fig. II:18) remain to be possibly executed.

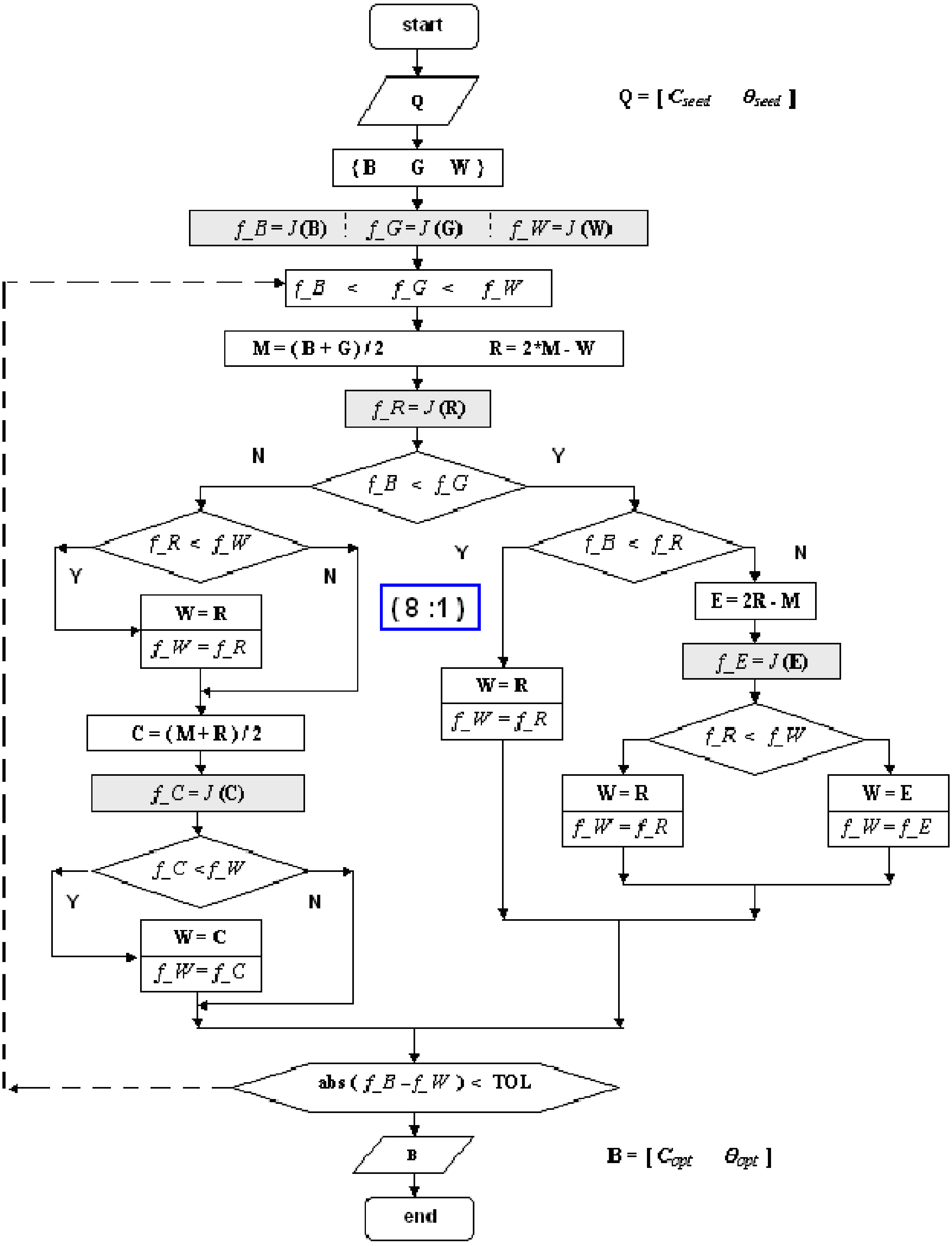

Fig. II:18 Schematic diagram of Adapted Nelder-Mead algorithm where “Inside Contract” and “Shrink” steps have been removed. The NM ***iteration*** *(shown by dashed arrows) can now only call f_R , f_E or f_C. The probability (f_C : f_E :: 8 : 1) is for* $\eta = 0.5$.

This leads to a direct reduction of total time needed to find optimized values by a factor of 2 (i.e. 50%) by deploying 3 objective function calls in parallel in hardware. The obvious disadvantage is the threefold expense of hardware resources used for implementing the objective function call block for a gain in time of a factor of two.

The mean of shrink percentages of 9 simulations is given in Table II-3.

It is evident that the reduction in the shrink percentages results in the increase of the remaining three step percentages and hence allows us to deploy 3 parallel function blocks.

η	0.1	0,5	0,9
Mean percentage of Shrink function calls	3.4%	1.5%	0%

Table II-3. The mean of percentage value of Shrink function call curves for varying starting points and η.

II.3.3.d Influence of η on the Contraction to Expansion Ratio

It is observed that η has also an influence on the ratio of contraction steps to expansion steps, which are executed in any given NM iteration.

By varying η, a higher ‘contraction to expansion’ ratio is obtained. Fortunately, as seen in Fig. II:19, the best value is again found by η = 0,5. Thus the same parameter reduces the number of function calls needed to optimize C and θ as well as to increase this ratio.

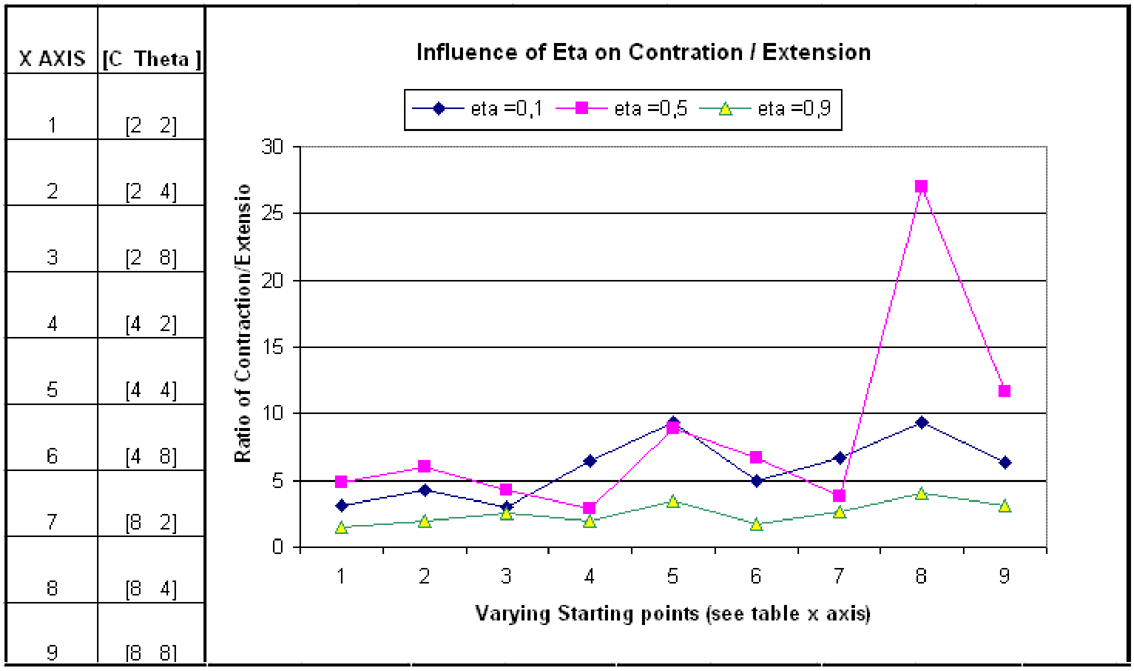

X AXIS	[C Theta]
1	[2 2]
2	[2 4]
3	[2 8]
4	[4 2]
5	[4 4]
6	[4 8]
7	[8 2]
8	[8 4]
9	[8 8]

Fig. II:19. Influence of η on the Contract–Expand Ratio for varying starting points.

This ratio becomes important when parallel calls to the objective function block are to be used to reduce the total time needed to find the optimum values. So by using a forward prediction, a contraction step function might be called at the same time as the call for a Reflection step. (It is reminded that a call to the Reflection step is always done at the beginning of each new NM iteration).

With a large probability of a contraction step rather than an expansion step, the parallel call helps to speed up the time needed. The cost of this increase is paid by the duplication of the hardware resources needed to implement the objective function in a real time system.

For example, using η=0.5, and with a quasi elimination of shrink step, the probability of the next function call being a Contraction step after a Reflect step is 8 to 1 as compared to an expansion step, as shown in Table II-4 and in Fig. II:18. Thus by using double parallel calls to the Reflect and Contract steps, this could lead to a reduction in total time for optimization by 43.75 %.

η	0.1	0,5	0,9
Contraction to Expansion ratio	5.9	8.4	2.5

Table II-4. The mean of contraction/expansion ratios for varying starting points and η.

II.3.4 Implementation of Adapted Nelder Mead FSM in StateFlow®

The adapted Nelder Mead Algorithm in the shape of a Finite State Machine (FSM) has been successfully implemented in StateFlow® in MATLAB®. The objective function calls have been executed using estimated phase samples of laser diode power in MATLAB.

The comparison of our FSM with the standard ‘fminsearch’ function of MATLAB is presented in Fig. II:20.

As indicated in Table II-5, the FSM implementation has provided excellent results while significantly reducing the total number of objective function calls.

No. of samples * 1000	1	2	3	4	5	6	7	8	9	10	**Mean**
Fn calls for ‘*fminsearch’*	88	88	93	82	87	83	85	83	87	89	**86.5**
Fn calls for FSM	40	41	52	53	62	56	55	58	55	58	**53**

Table II-5. The number of function calls used to optimise C and θ using two methods.

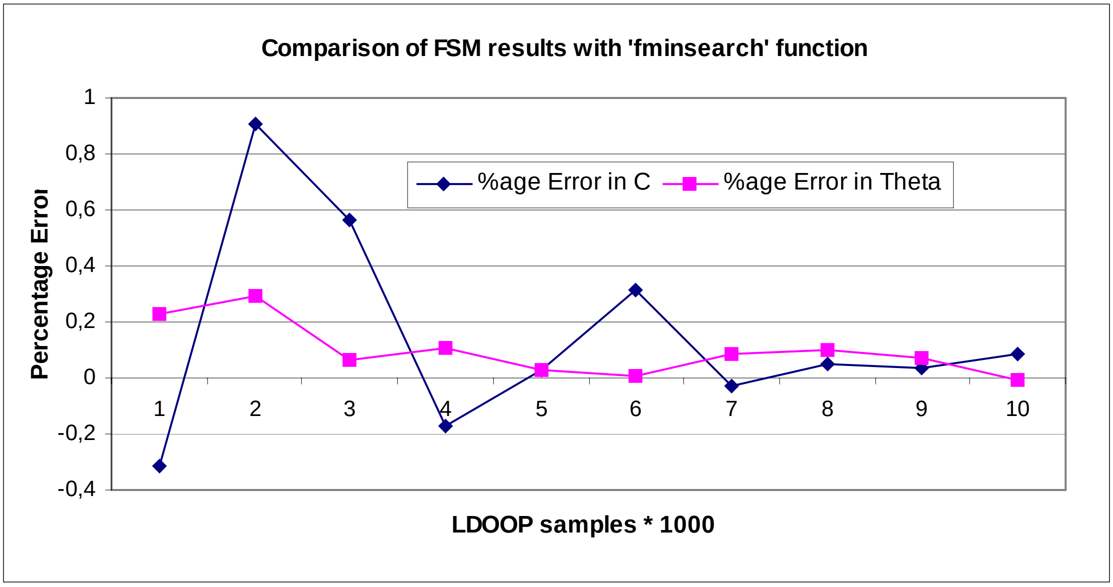

Fig. II:20. Percentage error in the optimisation of C and θ by the adapted NM FSM as compared with the 'fminsearch' MATLAB function from 1,000 to 10,000 samples along x-axis.

II.3.5 Implementation of the FSM in VHDL

Based on the FSM tested in StateFlow®, the algorithm has been coded in VHDL. The resulting code has 44 states and assuming a Spartan III Xilinx® FPGA, maximum frequency of 106.022MHz has been reported by the simulations.

The FSM used for the coding does not use pipelining of the objective function call block and hence this has been coded using a sequential approach.

Out of the total 44 states seen in Table II-6, the first 16 states are used to set up the initial simplex and the next 28 states execute a general NM iteration made up of the four basic steps.

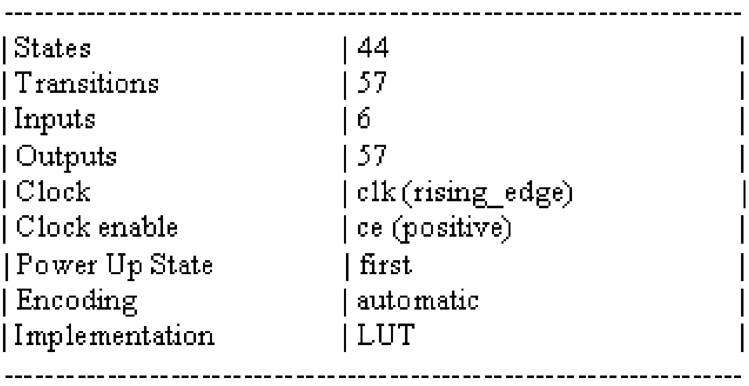

```
-----------------------------------------------------------------------
| States               | 44                                |
| Transitions          | 57                                |
| Inputs               | 6                                 |
| Outputs              | 57                                |
| Clock                | clk (rising_edge)                 |
| Clock enable         | ce (positive)                     |
| Power Up State       | first                             |
| Encoding             | automatic                         |
| Implementation       | LUT                               |
-----------------------------------------------------------------------
```

Table II-6. Extract from the Synthesis Report for the VHDL code of the NM FSM.

The previous results of Stateflow® simulations indicate that a mean value of 53 objective function calls (see Table II-5) was needed to find the optimised values. These calls were executed from 26 iterations of the NM algorithm (a typical iteration is indicated by the dashed arrows in Fig. II:18). So, by calculating the time for one NM iteration, one can approximate the total time needed to find the optimised values of C and θ.

Now, by assuming that the objective function call block is constructed by using only combinational logic and using one clock cycle of 10ns for execution of each state;

44 states * 10ns + 28 states * 26 iterations * 10ns = 7.72µs

are needed to converge to the optimised values by using a totally combinational logic based objective function block.

If, on the other hand, in order to reduce the hardware resources inside the objective function block, we use a sequential approach to process data, and assuming that the objective function block consumes 100 clock cycles for one execution (this value would in itself be subject to the number of laser diode phase samples to be stored and processed etc); for 53 function calls, the additional time amounts to 53 calls * 100 cycles * 10ns = 53µs.

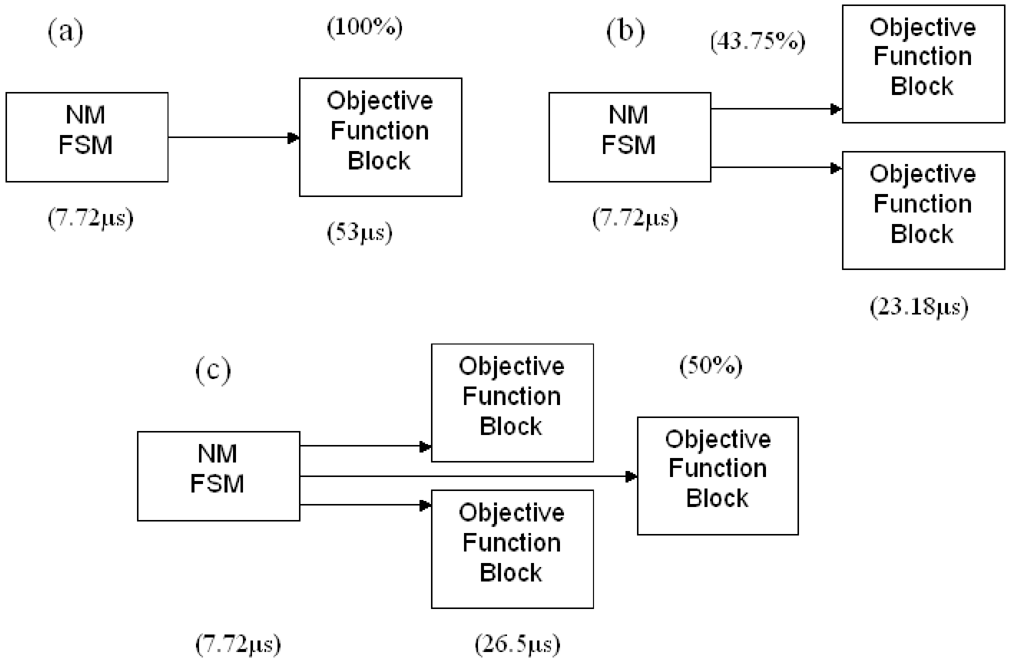

Fig. II:21 Use of parallelism for reducing the total time needed for joint optimisation. (a) no parallelism (b) double deployment of objective function block resulting in 43.75% improvement (c) triple deployment of objective function block resulting in 50% improvement.

This additional time can be reduced by 50 % using the Triple deployment of objective function block or by 43.75 % by using a Double deployment of objective function block by choosing a favorable value of η=0.5 and assuming that the shrink step is eliminated. However, it is noted that for 50 % gain in time as compared to an implementation of NM FSM without parallelism, the hardware resources consumed to implement the objective function block are tripled and are doubled for a gain of about 43.75 % (see Fig. II:21).

So, by a triple deployment of objective function block, we could gain only about 6 % in time at an increase in hardware cost of 33% as compared to a double deployment.

II.3.6 Assessment of Adapted Nelder-Mead

The signal processing required for the optimised joint estimation of the coupling coefficient characterizing the feedback regime and the line-width enhancement factor of the laser diode under moderate feedback has been done using the Nelder-Mead simplex method.

The optimization has led to a decrease in the number of LD optical power samples needed as well as in the reduction of the computing time for the signal processing of the said sensor.

Furthermore, influence of η on the implementation of the Nelder Mead Method for the optimisation of C and θ in a moderated feedback self-mixing laser diode sensor has been detailed. It has an influence on the number of objective function calls needed to optimize the parameters and is also important in order to obtain a high contraction to expansion ratio as well as on the reduction of the percentage of the Shrink step in a general Nelder-Mead iteration. Thus, by choosing a favorable value of η=0.5, considerable acceleration in the total time needed to converge to the optimised parameters can be achieved.

The overall adapted NM algorithm has been tested using StateFlow® and has been coded in VHDL to ascertain the order of delay to be expected for the time duration needed to converge. Methods for parallelism needed at the objective function level have also been outlined to reduce the delay at the cost of additional hardware resources.

However, even after these efforts, the Adapted Nelder Mead method is not fast enough to envisage a real-time displacement algorithm. This leads to a rethink of the manner in which the displacement is extracted from the OOP signals. The next section thus presents a new approach to this measurement.

II.4 Hybrid Optimization Algorithm

II.4.1 Introduction

As seen in the previous section, the optimisation for the joint estimation of the feedback-coupling coefficient characterizing the feedback regime and the line-width enhancement factor of the laser diode remains time-consuming. So, several other derivative-less optimization methods (such as Powell's method, uni-dimensional minimization methods and Nelder Mead Simplex method) have been considered to reduce this computation time. The results of the comparison have been used to propose a new faster hybrid method of optimization that has taken into account the behavior of these two parameters for a Self Mixing laser sensor [80]. This new method makes it possible to envisage the development of a real-time self-mixing micro-interferometer.

II.4.2 Physical Behaviour of C and α

According to the behavioral model of a self-mixing Laser Diode sensor [81], the influence of α on the shape of the self-mixing signal with feedback (2-5) is of second order as even a large variation can only cause a small drift. (Fig. II:22).

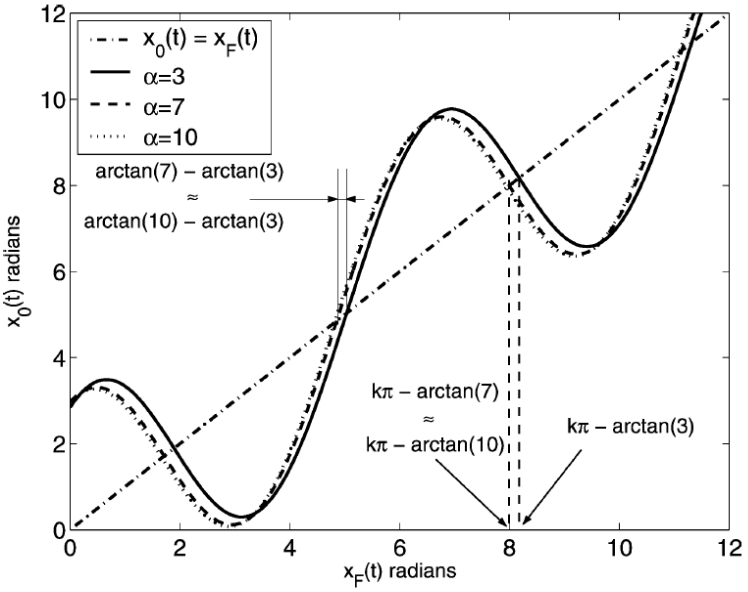

Fig. II:22 Three different calculated plots of $x_0(t) = G[x_F(t); C; \alpha]$ *obtained with* $\alpha = 3$, $\alpha = 7$, $\alpha = 10$, *and* $C = 3$. *The dash-dot curve represents a linear relation between* $x_F(t)$ *and* $x_0(t)$.

However, the influence of *C* on x_F (t) is far more important (Fig. II:23), as its influence is of first order for the SM regime changes [81].

Furthermore, the continuous monitoring of C is very important, as experimental data has shown that it is subject to variations even for a fixed distance D_0 between the laser diode and the target surface. For example, under experimental conditions, for a D_0 of *40cm*, the variations in C were observed just by translating the laser spot on the target (an adhesive micro-prisms surface). The result is depicted in Fig. II:24 where variations of *C* between the values of *1.9* and *5* can be noticed due to a varying quantity of light back scattered into the active cavity. These variations were observed just by translating the spot on a width of approximately *1cm* without changing $D_{0.}$

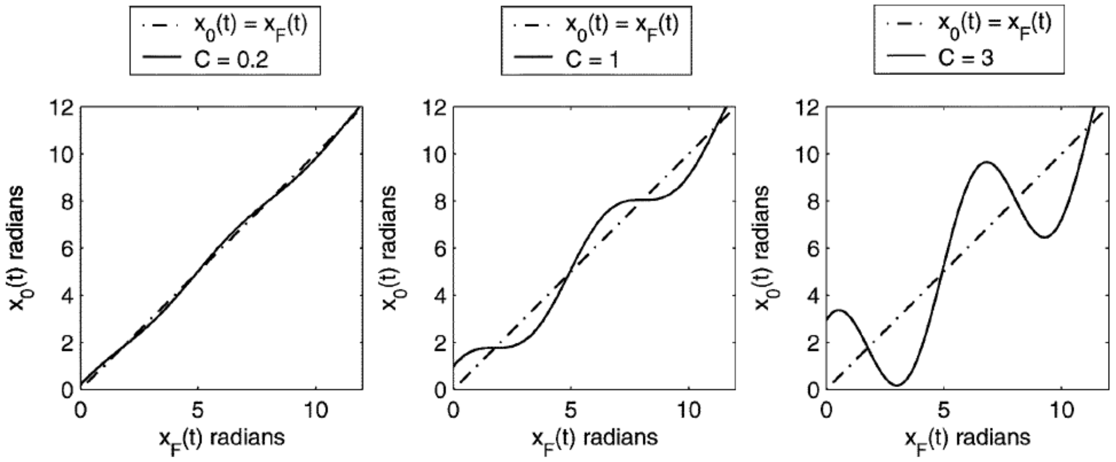

Fig. II:23 Three different calculated plots of $x_0(t) = G[x_F (t); C; \alpha]$ *obtained with C = 0:2, C = 1, C = 3, and* $\alpha = 5$*. The dash-dot curve represents a linear relation between* $x_F (t)$ *and* $x_0 (t)$*.*

As the self-mixing phase relationship and consequently the displacement measurements are highly dependent on this parameter so its correct determination is paramount for accurate displacement measurement.

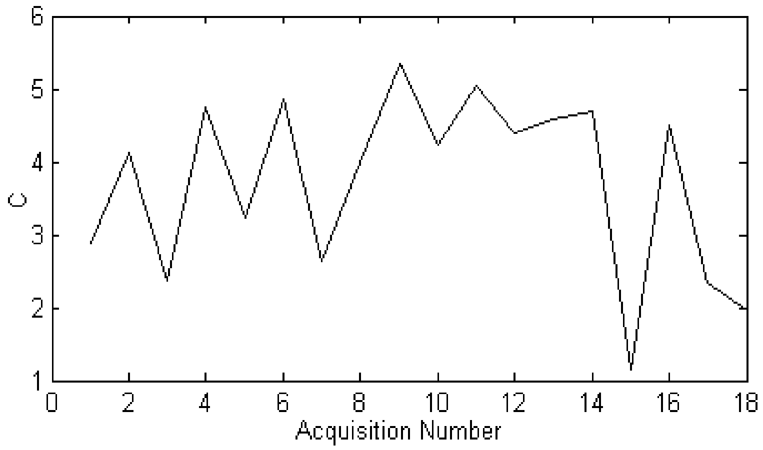

Fig. II:24. Variation in C, for a constant D_0*=40cm, by translating the laser spot on a micro-prism surface over a width of 1 cm.*

On the other hand, the effect of the variations in α on the phase equation remains of 2nd order, as can be seen in Fig. II:22. Likewise, the effect of a variation in α for a constant C on the OOP signal is also of 2nd order as can be observed in Fig. II:25. Moreover, once the initial phase value of the laser diode under feedback is estimated using the criterion *J(C,* θ), any further variations in $\theta = \arctan(\alpha) + x_F(0)$ are highly unlikely. Thus, it can be approximated as a constant and has no serious subsequent influence on the measurement of *C* or *D(t)*.

In fact, it is this important information that helps us to reduce the criterion *J(C,θ)* to a simple uni-dimensional estimation of *C* and allows for a more rapid convergence to the optimized value of *C*.

Let us now look in to various optimisation methods available to find out *C*.

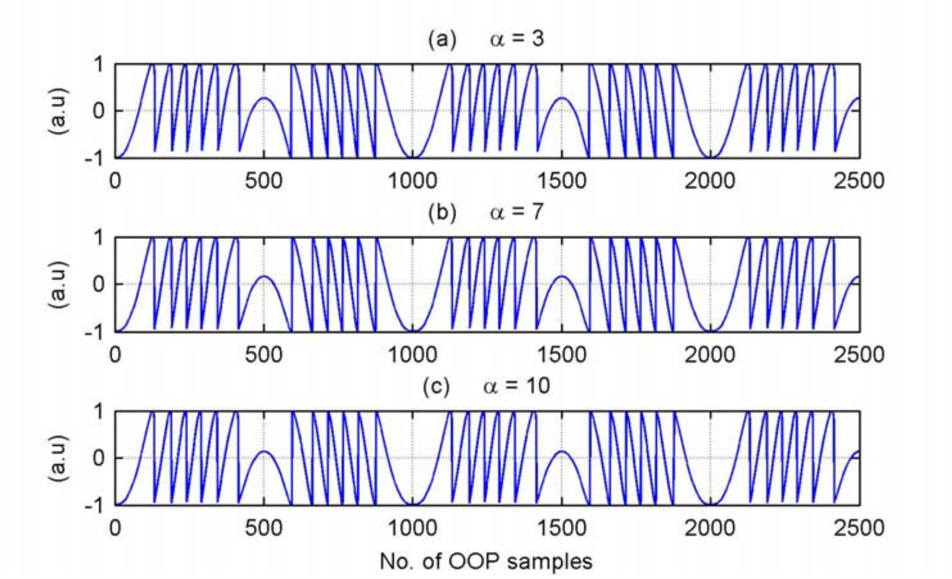

Fig. II:25 OOP signals for C=1.5 and (a) α=3, (b) α=7 and (c) α=10. The influence of α on OOP remains of second order.

II.4.3 Derivative-less optimisation methods

As the gradient information of the nonlinear and bijective functions (2-4) needed in Phase Unwrapping method (Fig. II:1) is difficult to obtain so derivative-less optimization methods have been considered for the evaluation of *J(C,θ)* and are detailed below.

II.4.3.a Powell’s Method

It is a simple variant of the well-known method of minimizing a multi-variable function by optimizing along one variable vector at a time [82]**.** It results in an approach that when the algorithm is applied to a quadratic form, the successive variable vectors take conjugate directions, so the convergence to the optimized point is fast when the method is used to minimize a general function.

As the Powell's method divides a given multi-variable function problem into uni-dimensional tasks, so line search techniques are needed for its execution. Thus, each uni-dimensional minimization along a certain variable vector results in successively approaching to the minimum point of complete multi-variable function space, as seen in Fig. II:26.

II.4.3.b Line Search Methods

Line search methods [83] are used as part of a larger optimization algorithm. At each step of the main algorithm, the line-search method searches along the line containing the current point, p_k, parallel to the *search direction*, which is a vector determined by the main algorithm, which in our case is the Powell's method.

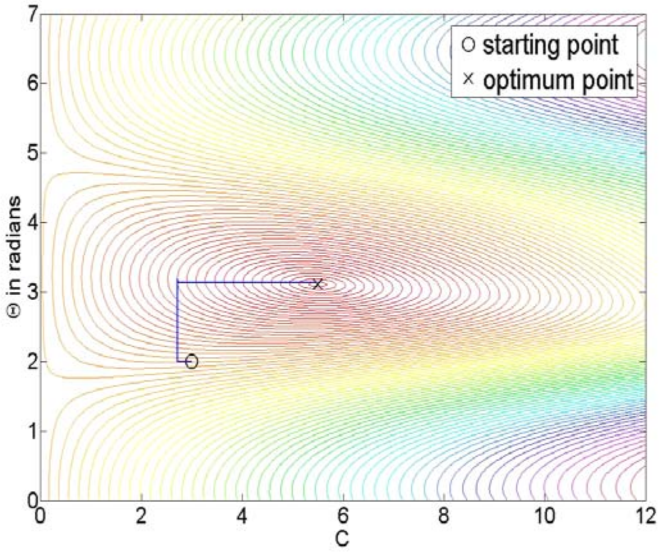

Fig. II:26. Convergence of the Powell's method (shown in blue line) from an arbitrary starting point to the minimum point over the J(C,θ) *surface (shown in colored contours).*

Thus, the line search method finds the next iterate p_{k+1} :

$$p_{k+1} = p_k + gd \tag{2-20}$$

where p_k denotes the current iterate, *d* is the search direction, and *g* is a scalar step length parameter.

The line search procedure has two main steps:

II.4.3.b.1 The Bracketing Step

The bracketing phase determines the range of points on the line to be searched. The bracket corresponds to an interval specifying the range of values of *g*.

For a successful convergence, the minimum must be bracketed so that for three unevenly spaced points $[p_1, p_2, p_3]$ and their associated function values $[f(p_1), f(p_2), f(p_3)]$, the points can be arranged to give $f(p_2) < f(p_1)]$ and $f(p_2) < f(p_3)]$.

Bracketing is started by incrementing the given point in the given direction by a certain initial step size that is subsequently doubled for every next iteration. Table II-7 shows the influence of initial step sizes of 1% and 8% (P-GS1 and P-GS2 respectively) on the Powell's method using line searches.

II.4.3.b.2 The Sectioning Step

The sectioning step divides the bracket into subintervals, on which the minimum of the objective function is approximated by either a search method (such as golden section or Fibonacci series methods) or polynomial interpolation (quadratic or cubic interpolation methods).

Polynomial interpolation methods are generally the most effective in terms of computational efficiency when the function to be minimized is continuous and quadratic in nature, which is the case of the criterion $J(C,\theta)$, as seen in Fig. II:27 for an experimental SM signal.

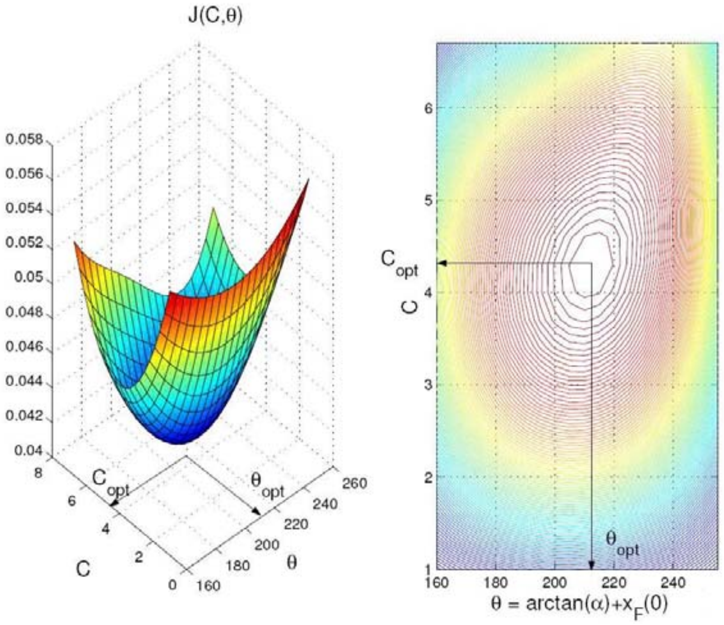

Fig. II:27. Criterion J(C,θ) *whose minimization results in the optimum couple of C and θ.*

II.4.3.c Golden Section Method

It is an efficient method for finding the minimum for a given unimodal function i.e. a continuous function f with a bracketed interval $I=[a,b]$ that has a unique number $p \in I$ such that f is decreasing on $[a,p]$ and that f is increasing on $[p,b]$. Fig. II:27 shows that this method may be applied to minimize $J(C,\theta)$ as it can be taken as a unimodal function.

II.4.3.d Quadratic Interpolation

For three unevenly spaced points and their associated function values, the *minimum* resulting from a second-order fit is given by

$$x_{k+1}=\frac{1}{2}\frac{\beta_{23}\,f(x_1)+\beta_{31}\,f(x_2)+\beta_{12}\,f(x_3)}{\gamma_{23}\,f(x_1)+\gamma_{31}\,f(x_2)+\gamma_{12}\,f(x_3)} \qquad (2\text{-}21)$$

where $\beta_{ij}=x_i^2-x_j^2$ and $\gamma_{ij}=x_i-x_j$.

Thus, the minimum point can be detected in an already bracketed interval by using just 3 objective function values. To further improve the computing time, the function values already computed in the bracketing step can be directly used, as shown in Table II-7 under P-QI1 and P-QI2.

II.4.4 Comparison Of Different Methods

The various algorithms, already presented in the previous sections, are summarized in Table II-7 that shows the number of objective function calls needed to converge to the joint estimation of C and θ for an experimental self mixing laser diode optical output signal.

TOL	**P-GS1**	**P-GS2**	**P-QI1**	**P-QI2**	**ANM**
0,001	158	175	99	75	61
0,0001	197	219	103	80	61
0,00001	275	315	130	83	68

Table II-7. Number of objective function calls for different derivative-less minimization algorithms for varying tolerance values.

TOL: tolerance parameter, used to define the terminating condition for convergence, for a given algorithm.

P-GS1: Powell’s method using Golden Search with a bracketing method starting with a 1% initial step size.

P-GS2: Powell’s method using Golden Search with a bracketing method starting with a 8% initial step size.

P-QI1: Powell’s method using Quadratic Interpolation without reuse of function values calculated in the bracketing method.

P-QI2: Powell’s method using Quadratic Interpolation reusing the function values calculated in the bracketing method.

ANM: Adapted Nelder Mead Simplex method [76].

II.4.5 The Hybrid Approach

The study of the physical behavior of *C* and θ as well as the various optimization methods leads us to propose a novel hybrid method. It allows fast calculation of *C* and the corresponding displacement as compared to other methods for a target inciting the self-mixing in a Fabry Perot laser diode sensor.

This hybrid approach divides the task into two steps:

- Firstly, a complete minimization of the criterion $J(C,\theta)$ *is* achieved either by the Nelder Mead Method [76] or the Powell's method as these methods allow an unconstrained derivative-less optimization of multi-dimensional functions by using only the objective function values.
- Secondly, as soon as the optimized value of θ is found, the hybrid method stops the joint estimation and only tries to minimize the parameter *C* for a given rough estimation of the laser phase. Thus, the dual optimization of *C* and θ now reduces to a uni-dimensional task. This can either be achieved using the line search and minimization techniques such as the golden section method or by using a polynomial interpolation such as the quadratic technique.

Thus, once the joint optimization is done (using one of the methods shown in Table II-7), the hybrid method, in its second step, need only minimize *C.*

Looking at Table II-8, only 3 calls for the QI method and from 20 to 30 calls for the GS method are needed for an accurate uni-dimensional estimation of *C* lying between a guess interval of C = [0 15]. ANM still needs about 30 iterations, even after θ has already been optimized proving it is not the ideal choice for uni-dimensional optimization.

TOL	**GS**	**ANM**	**QI**
0,001	20	29	3
0,0001	25	31	3
0,00001	30	31	3

Table II-8. Number of objective function calls for different derivative-less minimization algorithms for varying tolerance values 'tol', after θ has already been optimized.

So, for the hardware implementation of this hybrid method, the quadratic interpolation is to be used in conjunction with the Powell's method. The ANM method [76], though it gives faster convergence in the first step of the Hybrid Method, is not preferred as it is incompatible with the uni-dimensional optimization methods used for unimodal functions. On the other hand, for the Powell's method, these uni-dimensional techniques are its inherent part and are already there as its sub-routines. Therefore, by using Powell's method, no additional functional blocks may be needed to execute the two steps of the hybrid method.

Thus, if we recapitulate the already presented results, for a TOL value of 0.001, only 3 calls for the QI method are needed in the second step after the use of 75 calls of P-QI1 in the first step of the Hybrid Method.

II.4.6 Assessment of Hybrid Optimization Algorithm

In order to obtain an accurate real time displacement measurement based on a self-mixing laser sensor, it is necessary to efficiently compute the feedback-coupling coefficient C. After a first joint optimisation of C and the phase θ, only C needs to be calculated, as θ does not vary significantly until the sensor is switched off. So, the proposed hybrid method uses uni-dimensional optimisation methods in conjunction with more sophisticated optimisation methods. It enables us to minimize the overall computation time of the signal processing needed for the sensor, and allows a rapid calculation of the feedback-coupling coefficient.

However, it needs to be pointed out that at present, the tests were done on an experimental SM signal that did not have a large variation in C over time. Thus, the influence of a large variation in C over the course of time needs to be analysed to see if the method is able to correctly estimate a change in C over time. Such a method could prove an important tool in characterizing a variation in target surface or in the medium between the laser and the target in addition to measuring the target displacement.

II.5 Conclusion

In this chapter, the Phase Unwrapping Method for measuring displacement was analysed so that a faster variant of it could be designed. Initial studies indicated that the joint optimisation of C and θ was the most time consuming step. Hence efforts were done to either replace it (e.g. by using a Fourier Transform based technique) or improve it (e.g. by adapting the Nelder Mead algorithm used initially for minimisation a two-dimensional function). Then, further efforts were done to use the joint optimisation operation while replacing the Nelder Mead algorithm by a new approach called the Hybrid technique.

Although these efforts resulted in algorithms that take a lot less time to reach the optimised values but the fundamental nature of the algorithms did not change in the sense that it continues to need tens of thousands of samples that need to be saved and then processed. In other words, these remained of a non real-time nature contrary to a system that would only work on a few samples that arrive and get processed in real time.

Thus, in order to have a system that would use very few samples at a time, a new approach has been considered in the next chapter. The resultant algorithm has the added advantage of being compatible with the detection and correction of disappeared SM fringes, a phenomenon that occurs in case of increased feedback. This section shall be followed by the presentation of a new signal processing technique used to process multiple feedback regimes.

III Adaptive Solutions for Varying Optical Feedback

The previous chapter presented the efforts done to achieve a fast and efficient variant of the Phase Unwrapping Method. However, in spite of the improvements in the calculation time, the variants cannot be used for a real-time displacement sensor having a sub-half-wavelength precision.

This chapter, therefore, starts by presenting a method that is of a real-time nature. It needs no optimisation procedures and has the added advantage of compensating for the fringe-loss in case of harmonic vibrations.

Then, a strategy has been proposed that allows us to correctly detect and process the SM signals of weak as well as moderate feedback regimes. This has been achieved by replacing the static fringe detection approach used in the PUM that limited its use to only moderate feedback regime signals.

Finally, the experimental set-up based on adaptive optics in the form of a voltage controlled liquid lens is presented. This optical set-up allows us to obtain a reliable SM signal that would not be affected by the fringe-loss. The liquid lens then helps us to maintain the SM signal in a favorable regime and can be used to lighten the eventual signal processing needed to tackle a feedback change.

The present chapter thus presents the solutions needed to adapt to a change in the optical feedback level or the coupling factor. So, the effects of a change in the coupling factor have been countered either by using an algorithmic approach (such as the fringe-loss compensation and adaptive fringe detection) or by adding an additional component (the liquid lens) to the standard SM sensing system.

III.1 Fringe-loss Compensating Algorithm

The tedious optimisation procedure of the PUM (Fig. II:1) forces one to re-evaluate the working of this method. Let us plot the results of the two principal steps of this method i.e. the rough estimation of phase and the optimized estimation of phase (Fig. III:1).

Looking closely at the rough phase estimation, it can be seen that it's the direct addition of +/-2π that results in a staircase shaped signal. Such a signal is then processed through the optimisation step of the PUM.

So, instead of adding directly +/-2π at the instant of the fringe detection, we may place slopes of amplitude +/-2π between two detected fringes. Such a treatment would make the optimisation step redundant and thus a fast signal reconstruction can be achieved.

Thus, slope placement becomes the central idea of our new algorithm. However, a very important aspect of self-mixing need now be introduced that has a direct influence on metrological measurement, namely fringe-loss.

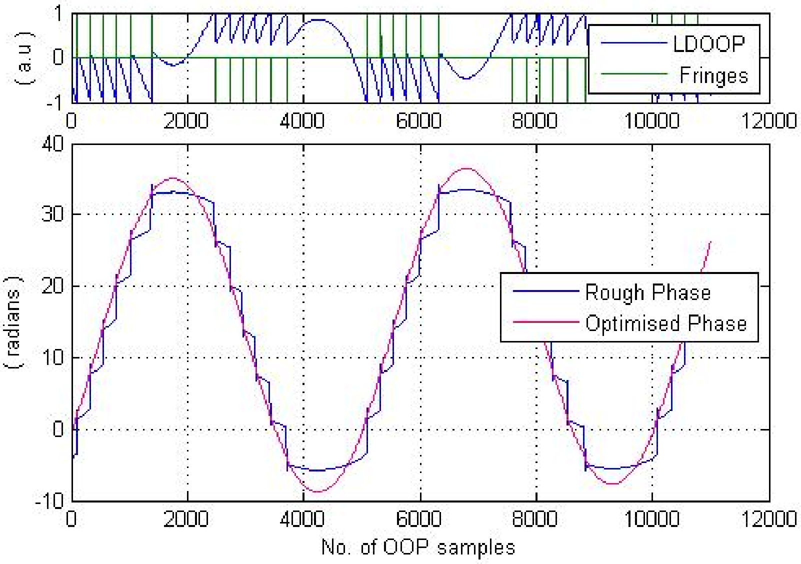

Fig. III:1The rough phase alongside the optimised phase calculated by PUM for an experimental LDOOP signal.

III.1.1 Fringe-loss in Self-Mixing Signals

When the LD is subject to the moderate feedback regime (C>1), a bifurcation takes place so that several solutions of $x_F(t)$ calculated from the phase equation (2-4) may exist for a given $x_0(t)$, inducing hysteresis (Fig. III:2) in the OOP fringes [10]. The fringe-loss then frequently occurs for SM signals in the presence of the multiple steady-state solutions. The feedback phase is given by $\phi = \omega_0 \tau_D + \arctan(\alpha)$, where ω_0 is the angular frequency of the solitary laser. The curve that separates the region of equal number of solutions of the phase equation can be expressed as:

$$\phi = (2k+1)\pi \pm \arccos\left(1/C\right) \mp C.\sin\left[\arccos\left(\left(1/C\right)\right)\right] \tag{3-1}$$

where *k* is an integer [85].

The *C* parameter plays an important role in fringe-loss. It is subject to vary with the time-of-flight τ_D – with respect to the distance D_0 to the target – and because of local fluctuations of the coupling efficiency and the surface reflectivity of the target (Fig. III:2). For example, as already seen in Fig. II:24, variations of *C* are achieved just by translating the laser spot on the target for a given constant distance [84]. These values of *C* have been estimated by using the behavioral model previously reported [81].

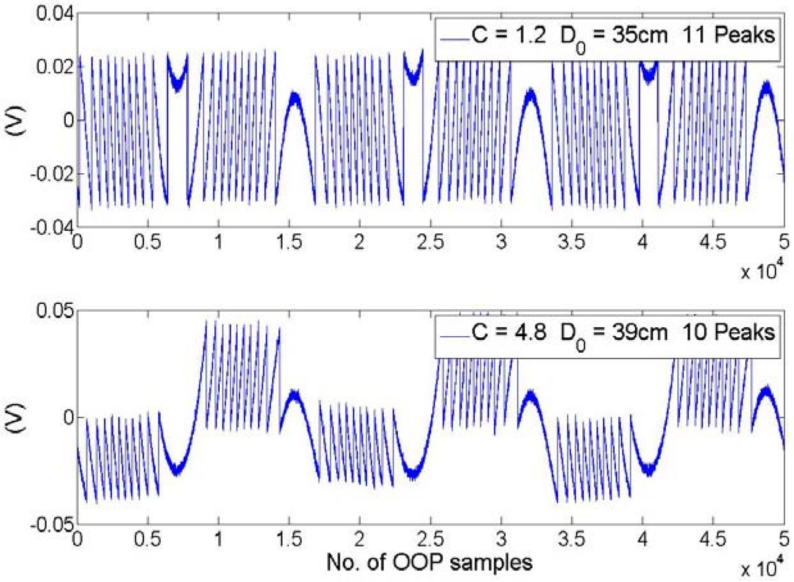

Fig. III:2. Experimental samples of acquired OOP signals showing hysteresis and fringe-loss.

For a LD subject to moderate feedback, a diminution of the total number of fringes and a variation of the excess fringe containing all the disappeared fringes may be observed when *C* is increasing (Fig. III:2). As keeping D_0 constant and hitting exactly the same point of the target surface is not realistic at all for most of industrial applications, so it proves the difficulty of keeping *C* constant, even roughly, or of maintaining the laser under weak feedback where no disappearance of fringes has been noticed.

In order to look further into the issue of fringe disappearance, OOP variations were simulated with the behavioral model for a displacement with constant amplitude of $16\lambda_0$ and a continuous variation of C. Table III-1 shows the variation in *C* needed for the disappearance of 10 fringes. The first fringe disappears for *C=2.7* whereas the second fringe disappears for *C=6.3*, i.e. for a variation in *C* of 3.6. Then, it can be noticed that for the disappearance of the even numbered fringes, an average increase in *C* of *3.83* was needed, by considering the 5 values shown in italic (noted $\Delta C'_1$). For odd numbered fringes (5 values shown in bold) an average value of only *2.6* was necessary (noted ΔC_1). Moreover average step of $\Delta C = 6.43$ is needed for the disappearance of two consecutive fringes [84].

Table III-1 Consecutive fringe disappearance for continuous variation of C.

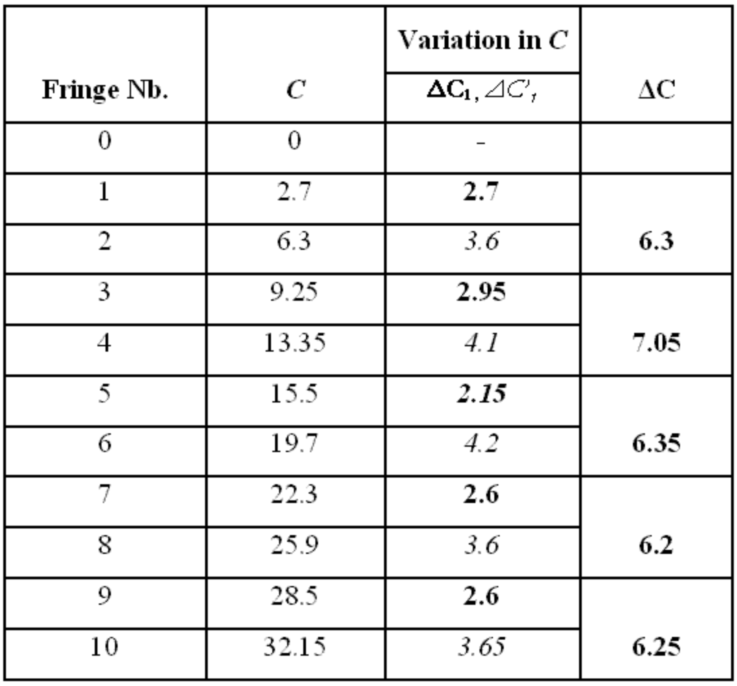

Fringe Nb.	C	**Variation in** C	ΔC
		ΔC_1, $\Delta C'_1$	
0	0	-	
1	2.7	**2.7**	**6.3**
2	6.3	*3.6*	
3	9.25	**2.95**	**7.05**
4	13.35	*4.1*	
5	15.5	***2.15***	**6.35**
6	19.7	*4.2*	
7	22.3	**2.6**	**6.2**
8	25.9	*3.6*	
9	28.5	**2.6**	**6.25**
10	32.15	*3.65*	

The step function (Fig. III:3) depicts the number of fringes N occurring under moderate feedback in (C, ϕ)-space for a constant target displacement amplitude. N can decrease (fringe-loss) depending on values of ϕ and C. For a fixed value of ϕ, a variation in C of 2π will cause a loss of 2 fringes [85]. On the other hand, for a fixed value of C, the variations in ϕ will generally cause a loss of a single fringe.

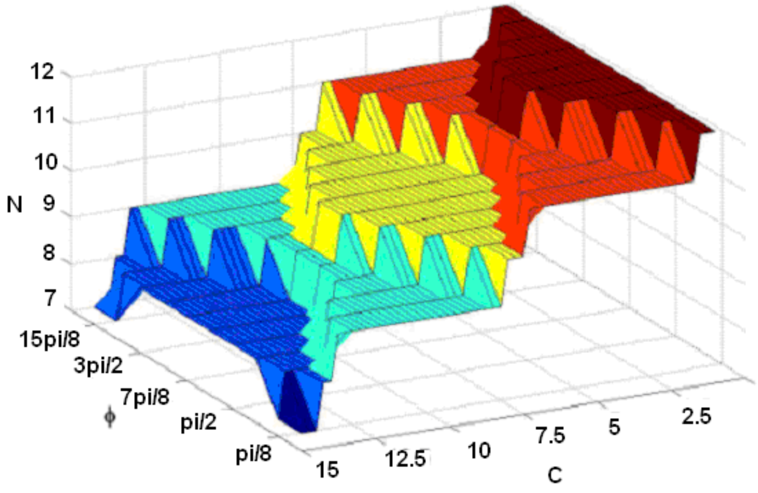

Fig. III:3. Number of fringes N as a function of C *and* ϕ *for constant displacement amplitude of* $6\lambda_0$..

For example, using the behavioral SM model to analyze the influence of C, Fig. III:4 presents 3 SM signals for the same harmonic target displacement of $4\lambda_0$. Starting with C equal to 1.2 in Fig. III:4 (a), each subsequent variation in C of 2π results in 2 lost fringes as seen in Fig. III:4 (b-c).

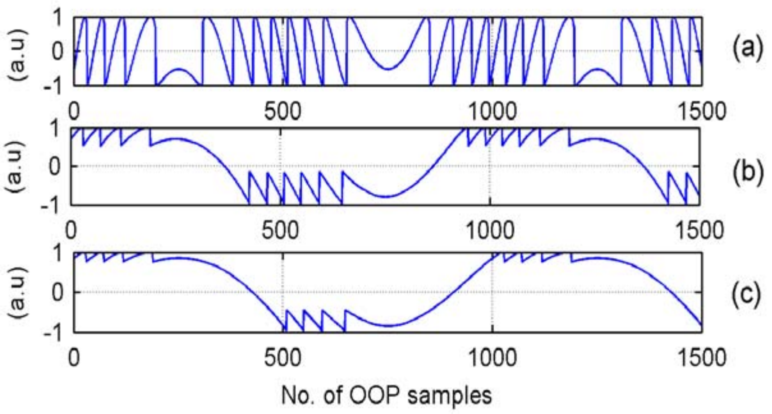

Fig. III:4. Simulated SM signals for the same harmonic target displacement of 4λ_0. Fig. (a-c) correspond to a C value of 1.2, 7.48, and 13.76 respectively.

III.1.2 Fringe-loss and Displacement Measurement

The above-mentioned fringe-loss has a direct influence on the measurement of displacement. For the case of the simple Fringe-Counting Method (FCM) [33], it is easy to see that each lost fringe shall result in an added error of half-wavelength. Likewise, even the sophisticated Phase Unwrapping method (PUM) [39] fails in the presence of fringe-loss and presents increased error. Considering Fig. III:5, for a target displacement of 3.42µm, the accuracy of this method is only about 10% when fringes have disappeared. The resultant error of 309nm in the case of fringe-loss is thus far greater than the documented error of around 40nm when there is no fringe-loss.

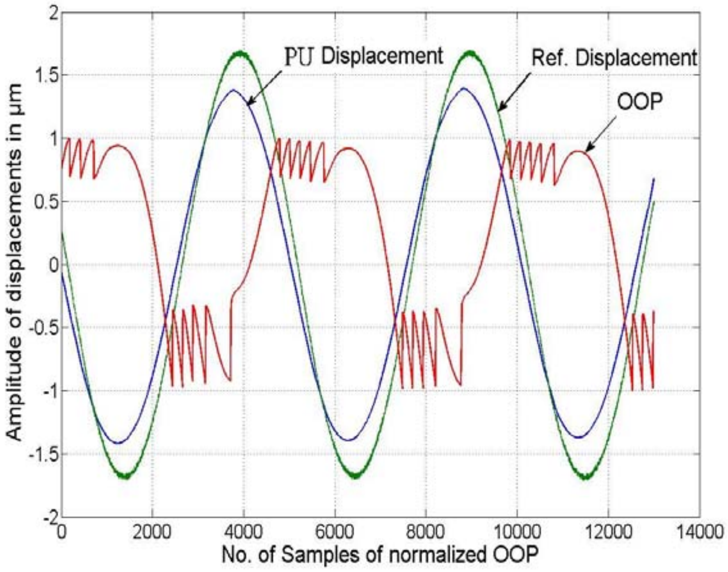

Fig. III:5. Non-convergence of the Phase Unwrapping Method (PU) for a practical SM signal under fringe-loss alongside a reference signal. Error is of 309nm for a displacement of 3.42µm.

III.1.3 Slopes based Method and Fringe-loss Compensation

Just as in external interferometry, each OOP fringe of SM signal represents a displacement of $\lambda_0/2$ (or a phase change of 2π), where λ_0 is the LD wavelength under free running conditions. Thus, a simple fringe counting method can only lead to a half-wavelength resolution. This resolution, however, can be improved by using more sophisticated methods, such as the Phase Unwrapping method (PU), by unwrapping the phase around each fringe-detection where each detection contributes $\pm 2\pi$. So, for a displacement without fringe-loss of $D(t)=N\lambda_0/2 + \varepsilon$, the excess fringe '$\varepsilon$' ($< \lambda_0/2$) is estimated by the simultaneous extraction of C and α parameters. However, in the presence of fringe-loss, even this advanced method fails in ensuring a good resolution.

So, a new technique to compensate for the fringe-loss is proposed [86], as shown in Fig. III:6.

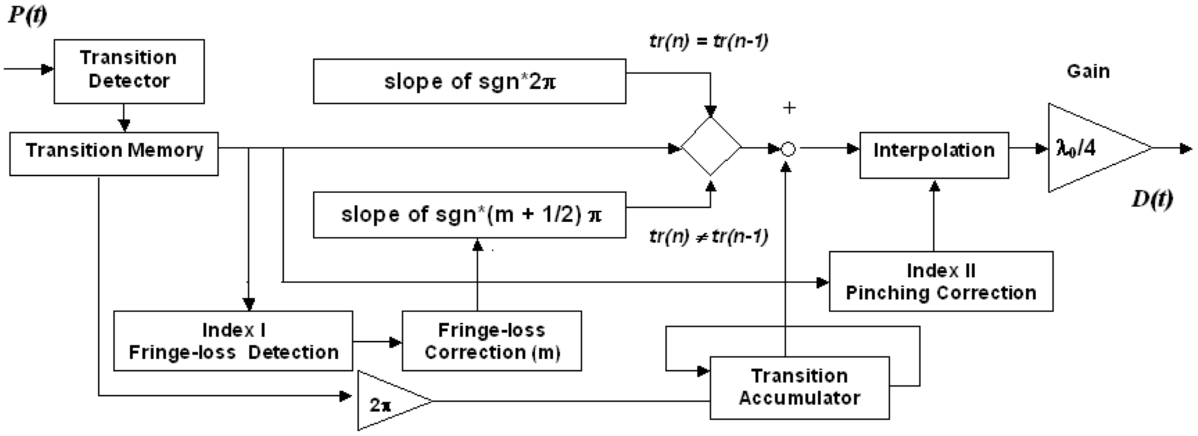

Fig. III:6. Schematic block diagram of the fringe-loss compensating algorithm.

The algorithm starts by reconstructing the phase from the SM signal. The SM fringes, characterised by the sharp edge of the saw-tooth shape, are detected as $tr(n)$ where $n = 0, 1, 2, \ldots$ is the number of fringes detected. These transitions are then saved in the Transition Memory block along with their respective signs 'sgn' and the number of samples (representing the time) counted since the previous transition. Based on the sign of the previous two detected transitions, the algorithm either selects a "slope of sgn×2π" block or a "slope of sgn×$(m + ½)\pi$" block (as represented by the diamond decision block), where $m = 0, 1, 2, \ldots$ is the number of lost fringes. The procedure used to determine m will be addressed later. Thus, a slope segment of 2π is selected if the last two transitions are of the same sign ($tr(n) = tr(n-1)$), indicating no direction-reversal. The slope segments of $(m + ½)\pi$ are used if a vibration maximum or minimum has been detected, represented by a change in sign of the last two transitions ($tr(n) \neq tr(n-1)$), i.e. when the direction of displacement of the target has changed. The

Transition Accumulator simply increments / decrements itself by 2π, at each new positive or negative transition. This results in the slopes based reconstruction shown in Fig. III:7 (a) and final displacement is found after Gain block of $\lambda_0/4\pi$. In the case of displacement signal pinching (to be detailed later), interpolation is used to correct this anomaly.

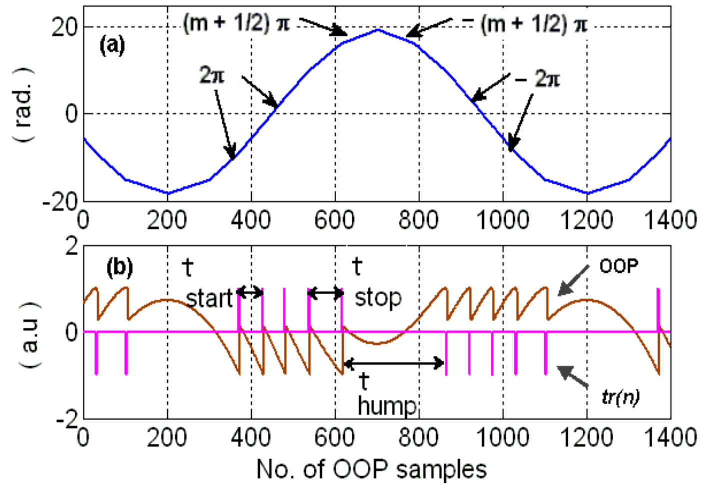

Fig. III:7. (a) Slopes based phase reconstruction. (b) Index calculations based on the time intervals between OOP fringes.

The slope segments of $(m + ½)\pi$ fulfil two roles: fringe-loss compensation and the estimation of ε.

As m lost fringes correspond to a loss in phase amplitude of $m2\pi$ so a direct addition of $m\pi$ at the maximum and the minimum of the reconstructed harmonic displacement respectively compensates m lost fringes. Then, we have to reduce the error due to 'ε'. So, the addition of $\pi/2$ at the maximum and at the minimum of phase reconstruction results in the max. possible error of $\lambda_0/8$ at the vibration maxima and minima.

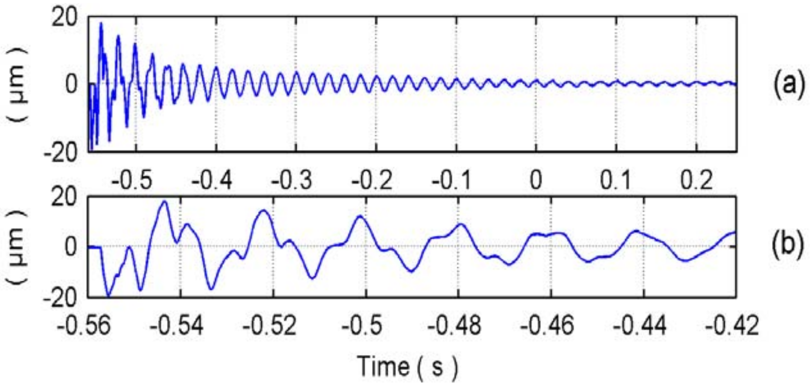

Fig. III:8 (a) Displacement retrieved from a SM OOP signal obtained from a vibrating concrete pillar excited with a single shock. (b) Zoom at beginning.

An example of the reconstruction using this algorithm is represented in Fig. III:8. The displacement is obtained for an arbitrarily vibrating concrete pillar excited with a single shock.

III.1.3.a Index I & II

We propose here two parameters that we call Index I & II that can be used to compensate the fringe loss.

For a given SM signal corresponding to a harmonic displacement, the fringe-loss for a given target vibration can be detected by using Index I = t_{start}/ t_{hump} where t_{start} is the time (or no. of samples) between the first two consecutive same-signed transitions and t_{hump} the time taken by the central transition-free hump zone (Fig. III:7 (b)), under the condition that C should remain constant for one period only. The evolution of this index is represented in Fig. III:9 as a function of C and for 5 different values of ϕ. It can be seen that as a result of increasing C, each fringe loss for a given ϕ results in a sharp fall in its value and this can be used to detect the fringe-loss. What makes the event Index I useful is that there are no intersections of its values for a certain fringe-loss with another value corresponding to a higher fringe-loss for at least the first three fringe losses. Thus, specific zones of the Index I can be designated to no fringe loss (m = 0), the first fringe loss (m = 1), the second fringe loss (m = 2) etc. For the 4th or beyond lost fringe, the method compensates at least 4 fringes as intersections between different curves start to appear after the third fringe-loss. So, our technique correctly detects the fringe-loss for the first 4 fringes which is equivalent to a variation of C = 4π. Once m is found, the algorithm duly compensates the fringe-loss by adding $2\pi m$ to the phase reconstruction.

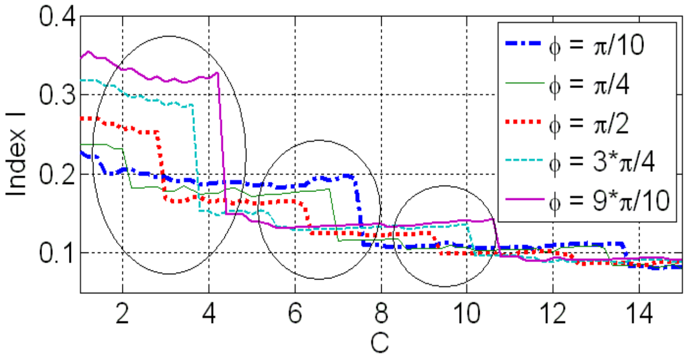

Fig. III:9. Index I for increasing C *and* $\phi = [\pi/10\ \ \pi/4\ \ \pi/2\ \ 3\pi/4\ \ 9\pi/10]$ *and displacement amplitude of* $6\lambda_0$*. The circles represent the first three fringe losses.*

The other useful ratio is Index II = t_{start}/ t_{stop} where t_{stop} is the time between the last two transitions before direction change (Fig. III:7. (b)).

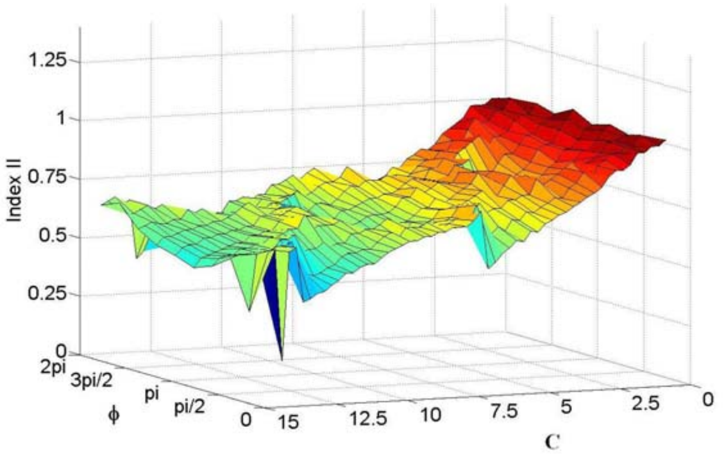

Fig. III:10 Index II for intervals C = [1⋯15] and ϕ = [π/10 ⋯19π/10] with a constant displacement amplitude of 6λ.

The Index II calculated by using simulated SM signals (Fig. III:10 and Fig. III:11) demonstrates that an increase in *C* causes the last fringe before direction reversal to continually move away from the rest of the fringes (corresponding to a decrease in Index II) until it merges into the central zone called "hump" (i.e. sudden increase in Index II corresponding to a fringe loss). The same is observed in experimental SM signals and such a detached last fringe can cause a pinching of the reconstructed signal (as shown later in Fig. III:18). So, Index II helps to detect a possible pinching of the reconstructed signal, and then it can be corrected using the Interpolation block of Fig. III:6.

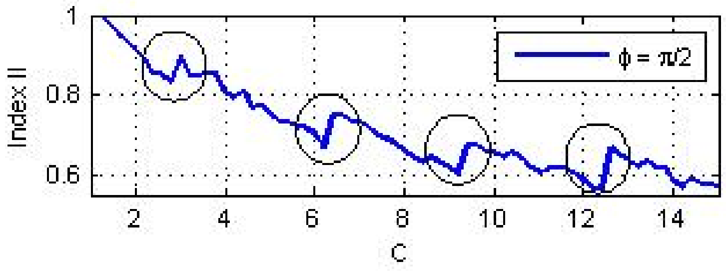

Fig. III:11. Index II for intervals C = *[1⋯15] and* ϕ = *π/2 for a constant displacement amplitude of 6λ_0. The circles represent the fringe losses.*

III.1.3.b Displacement Maxima and Minima Placement

The maxima or minima for a given displacement are calculated at the moment of the change in direction of the signal, which is obtained by observing the reversal of the sign of any two consecutive transitions. Thus, somewhere between these two transition instants, the target displacement reaches its extreme point (positive peak for a positive transition followed by a negative transition or negative peak for a negative transition followed by appositive transition).

For the case of signals with symmetric ascent and descent, the maxima are placed by firstly considering t_{tr} the time taken (i.e. the no. of samples) between the transitions *tr(n-1)* and *tr(n)* where *tr(n)* is the latest transition that has changed sign (Fig. III:12). The value $t' = tr(n-2) - tr(n-1)$ is then subtracted from t_{tr} in order to define a reduced interval t_{eff} which is divided into two equal parts, denoted t''. So, a slope of $-sgn*\pi$ is placed over the first interval t'' and a slope of $sgn*\pi$ is used for the second segment of t'', where *sgn* is the sign of *tr(n)*.

This is done to ensure that the placement of the slopes fits more accurately with the local maximum of the OOP. As a matter of fact, π slopes spread over the interval t_{tr} instead of t_{eff} would have shifted the reconstructed peak where as the slopes spread over t_{eff} are rightly aligned to the local max. of the OOP signal. It can also be observed that the replacement of t_{tr} by t_{eff} leaves an interval t' $(t_{tr} - t_{eff})$ before the beginning of the nth transition so that a slope of $sgn*2\pi$ is positioned.

The advantage of the above-mentioned method is that the right instant of signal maxima or minima can be easily found using simple subtraction of the transition instants already stored in the Transition Memory block. The other option would have been the search of local maxima or minima of the OOP signal within the t_{tr} interval but as the shape of this central zone may be complex so the time calculation could be longer.

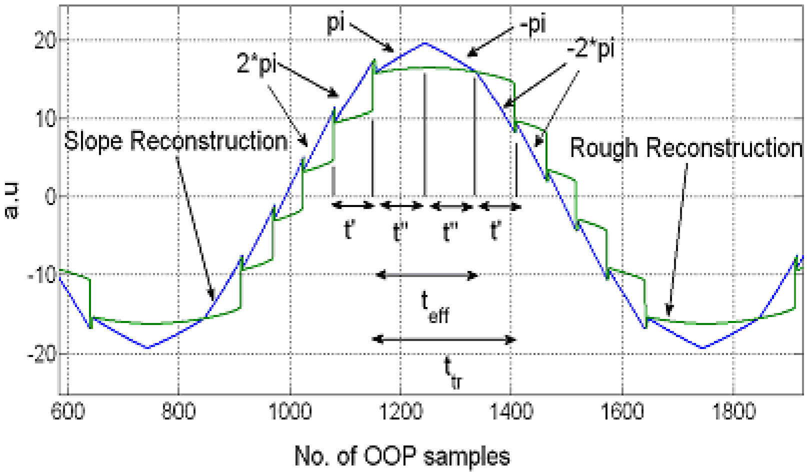

Fig. III:12. The calculation of the right instant of displacement maxima or minima, based on the time interval between the second-last transitions.

III.1.4 Simulated Measurement Results

For the case of harmonic vibrations of peak to peak amplitude of $6\lambda_0$, the error at the target signal maxima has been calculated for the Slopes Based Method (SBM) as well as PUM and FCM and the results are plotted in Fig. III:13 for a variation in *C* from 1 to 15. As can be seen in Fig. III:14, the SBM has been able to correctly detect and compensate the fringe-loss. Thus, the influence of fringe-loss is minimal in the case of SBM where as the other two methods' error is directly proportional to fringe-loss.

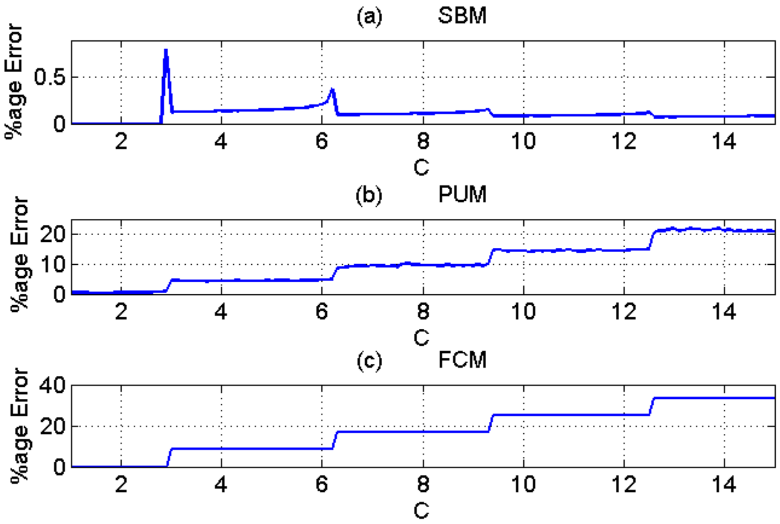

Fig. III:13 The measurement error at the target signal maxima for the SBM, PUM, and FCM for a constant peak to peak amplitude of 6λ_0 and a variation in C *from 1 to 15.*

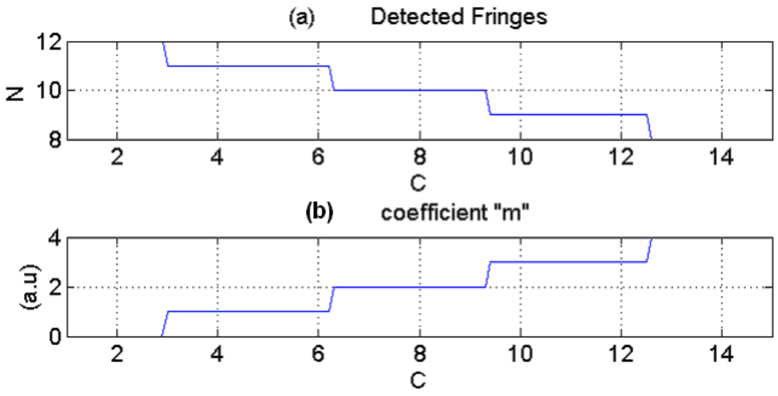

Fig. III:14 The No. of detected fringes "N" and the coefficient "m" found by the SBM for a constant peak to peak amplitude of 6λ_0 of the target vibration and a variation in C *from 1 to 15.*

III.1.5 Experimental Measurement Results

The experimental set-up, used to validate the method, consists of a commercial piezoelectric transducer (PZT) from Physik Instrumente (P753.2CD), used as a target. This PZT is equipped with a capacitive feedback sensor for direct-motion metrology with a resolution of 2 nm. The laser used for the self-mixing sensor is a Hitachi HL7851G laser diode emitting at 785 nm. Fig. III:15 presents the set-up where *g(t)*, *r(t)* and *sm(t)* are the excitation, reference counter-measurement and self-mixing signals respectively.

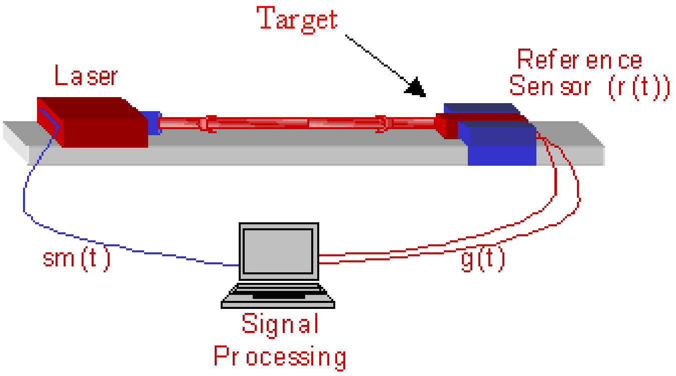

Fig. III:15 Experimental set-up for the characterization of the sensor.

A photograph of the actual experimental set-up on an optical table is shown in Fig. III:16 and the various instruments used are enumerated.

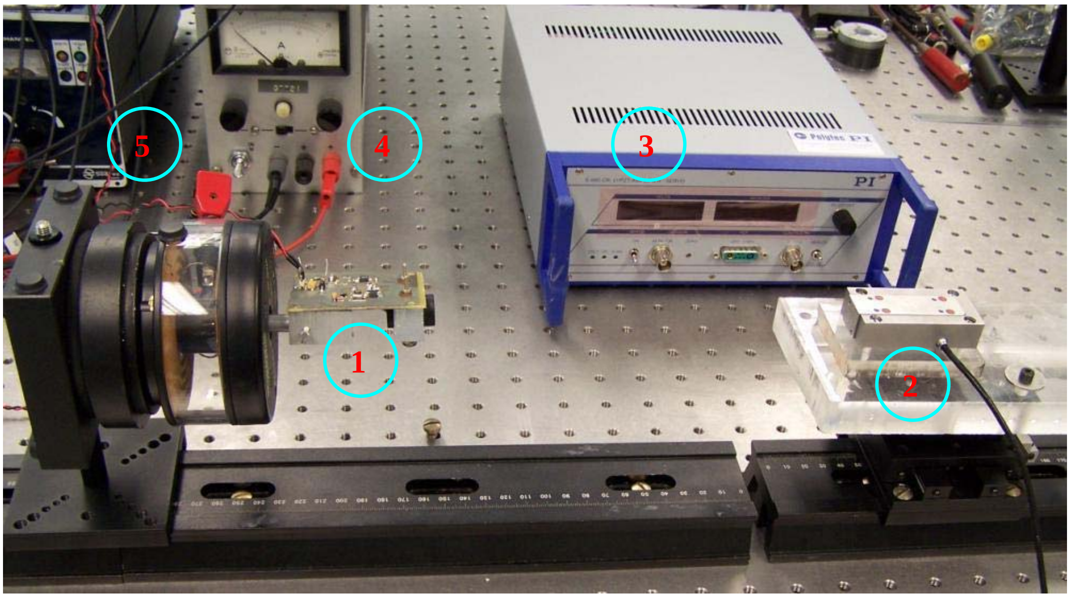

Fig. III:16 Actual experimental set-up. (1) is the LD circuit board, (2) is the PZT transducer with a capacitive sensor, (3) is the PZT controller, (4) is the LD power supply, and (5) is the signal generator for PZT excitation.

Considering Fig. III:17, for a peak to peak sinusoidal displacement of 3.42 µm, OOP signal should contain at least 8 fringes for λ_0 of 785 nm. The experimental SM signal has only 6 fringes for each half cycle. So, the loss of two fringes (m = 2) was detected and compensated by our technique to give an error of 41 nm at the signal maxima. The error at the maxima for PU is 290 nm. For the fringe-counting method, the error is ($m\lambda_0/2 + \varepsilon$), i.e.1063 nm.

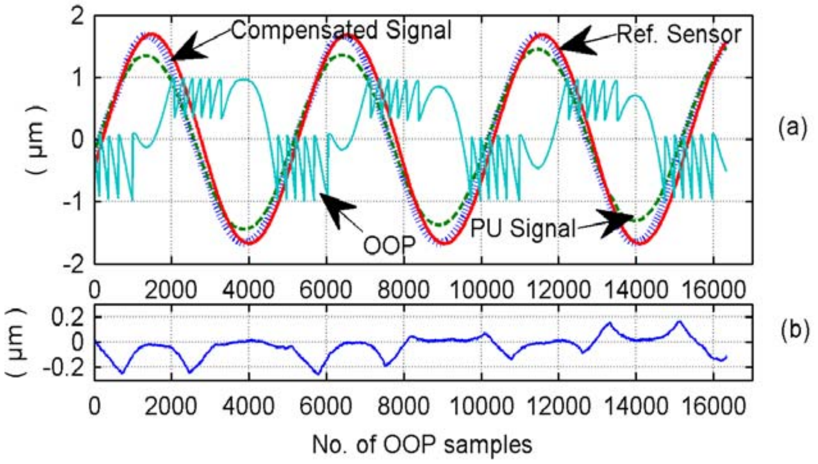

Fig. III:17 (a) Detection and correction of 2 lost fringes for an experimental SM signal alongside a reference sensor signal. (b) Difference between the compensated signal and the reference sensor signal.

For the same amplitude of displacement, for the OOP with only 5 fringes, compensation of 3 lost fringes has resulted in an error of 35 nm at the signal maxima, as seen in Fig. III:18. Use of PU and fringe-counting methods results in an error at the maxima of 309 nm and 1456 nm respectively. It can be noticed that the OOP signal also contains a soon to be lost fringe. The pinching caused by it has also been corrected.

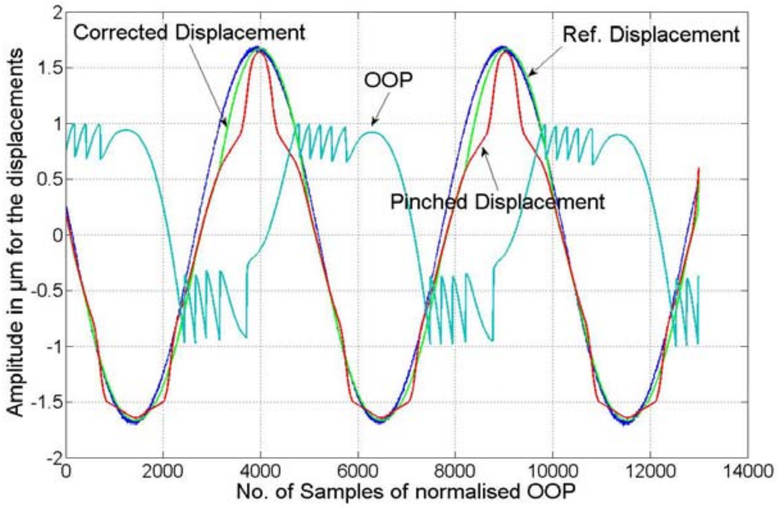

Fig. III:18. Detection and correction of 3 lost fringes as well as pinching correction for an experimental SM OOP signal alongside a reference sensor signal.

Our technique has successfully processed the SM signals with *m* from 0 to 4. The error for these cases is about the same, thus rendering it independent of fringe-loss in moderate SM signals. This approach has been successfully tested on various experimental SM signals proving its reliability with an error of around 45 nm as shown in Table III-2.

m	0	1	2	3	4
Error (nm)	56	59	41	35	45

Table III-2 The error in nm at the maxima of the reconstructed displacement for the experimental OOP signals having a fringe-loss from 0 to 4 for the same target vibration.

III.1.6 Conclusion

A new faster and more precise method has been presented for a self-mixing sensor under moderate feedback enabling us to measure displacements faster than the previously-reported phase-unwrapping method with the same accuracy when the signal presents no fringe loss. In the specific case of harmonic vibrations, fringe-loss detection and compensation has been achieved. Our technique has successfully processed the SM signals for the first 4 lost fringes i.e. a variation of $C = 4\pi$, with an error independent of fringe-loss in moderate SM signals. The proposed algorithm needs no time-consuming optimizations and so shall be implemented on a FPGA for a real-time vibration sensor.

III.2 The Transition Detection Algorithm

III.2.1 Introduction

In order to successfully extract the displacement information from the SM signals, an important step is the SM fringe or transition detection. Such a step has already been presented as a part of the rough estimation section of PUM, as shown in its schematic block diagram of Fig. II:1. Although this may appear to be a simple and straightforward operation but in reality it requires a detailed analysis of the SM signals as these tend to vary in shape and amplitude with a variation in the C parameter. It is reminded that the published PUM worked only for moderate feedback regime and could not process weak feedback regime [39]. Furthermore, even in the moderate regime, it cannot adapt itself to a change in feedback and needs a manual adjustment to correctly detect the SM fringes. Thus, the goal of the study presented in this section is to have an auto-adaptive fringe detection algorithm that adapts itself to the varying regimes of the SM signal without any external intervention. Such an algorithm can then be used in conjunction with the PUM so that it can work autonomously while increasing its working range to weak as well as moderate regime SM signals.

So, a new algorithm for self-mixing sensors has been developed to perform displacement measurements [87]. It is able to differentiate between the different self-mixing regimes (very weak, weak, moderate and strong) and thus converges automatically to the optimum threshold level required to detect all the self-mixing fringes, independently of the shape of the signal. Displacement reconstructions based on this algorithm have been validated with counter measuring commercial sensors for both weak and moderate regime acquisitions that are most frequently encountered under experimental conditions.

III.2.2 Existing SM Processing Techniques

In the literature, displacement measurements are generally performed with laser subject to moderate feedback as this regime is the most usually encountered in experimental set-up [39], [43]. However, displacement has also been measured under weak feedback regime in particular with diffusive targets [40] or with optical-fibered sensor [88]. A method permitting to recover displacement without directional ambiguity for both weak and moderate feedback has previously been proposed [89]. However, it required the time consuming estimation of *C* and a preliminary experimental calibration to evaluate the linewidth enhancement factor.

In this section, we focus on the automatic detection of the OOP fringes in order to develop unique signal processing for both weak and moderate feedbacks without any calibration or parameter extraction. This results in an accurate displacement measurement based on either weak or moderate feedback SM signals using the same algorithm.

III.2.3 Influence of the Feedback Coupling Factor

The feedback-coupling factor *C* is subject to vary with τ_D (i.e. the distance to the target) and because of local fluctuations of the coupling efficiency and the surface reflectivity of the target. A varying level of feedback then results in different shapes of variations of the OOP. The very weak regime ($0 < C < 0.2$) has sinusoidal fringes, the weak regime ($0.2 < C < 1$) is characterized by slightly asymmetric OOP fringes, the moderate regime ($C > 1$) presents sharper sawtooth-like OOP signal with hysteresis whereas the strong feedback regime results in a fringe-free OOP signal [90]-[91]. Thus, each regime may require an adapted signal processing for displacement measurements.

In Fig. III:19, the effects of increasing feedback level *C* on the OOP are simulated using the behavioural model . It can be seen that not only the shape but also the amplitude of the OOP fringes varies. This becomes even more evident for the SM signals with hysteresis where the amplitudes of the upper and lower halves’ fringes of the SM signals are comparatively different. Furthermore, the decrease in fringe number for increasing *C* finally results in total disappearance of fringes and SM signal can then be classified as in strong regime [92].

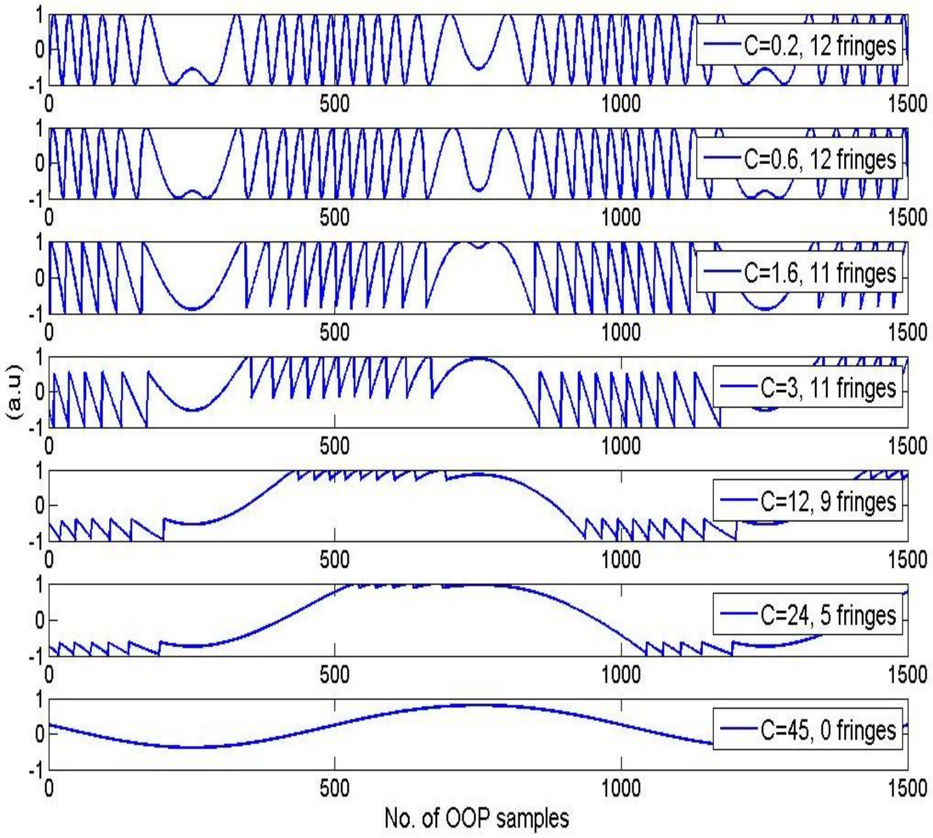

Fig. III:19. Effect of different feedback levels C on the SM signal fringe amplitude and shape for a target displacement of 12(λ_0 /2).*

The *C* parameter becomes all the more important as it varies a lot even for a constant laser to target distance (Fig. II:24). Thus, under practical conditions, it becomes quite difficult to maintain the SM signal in a given feedback. Such behaviour thus necessitates increased signal processing.

III.2.4 Displacement Reconstruction

In order to process all these signals, we have to improve the previously described PUM that has been summarized in the schematic block diagram (Fig. II:1). It can be split up into two principal steps. The first one leads to the rough estimation of the phase $x_F(t)$. After an Automatic Gain Control (AGC) of $P(t)$ to get $P'(t)$ ranging over a ±1 interval, an arc-cosine function is used to get $x_F(t) \bmod \pi$. The derivative of the $arccos(P'(t))$ is then compared with a threshold value to ascertain the presence of a transition (or a fringe) through the transition detector. An integrator then adds or subtracts 2π to $x_F(t)$, depending on the sign of the transition when a SM fringe occurs. The second signal processing step deals with the joint estimation of parameters, *C* and $\theta = x_F(t=0) + arctan(\alpha)$. The resultant phase $x_0(t)$ is then used to finally recover the displacement $D(t)$.

It is to be noted that the transition detection corresponding to $d[\arccos(P'(t))]/dt$ remains a key element of this algorithm if we wish to have a unique signal processing of weak and moderate feedback levels. Each missed and/or false transition detection directly affects the displacement measurement accuracy by a factor of $\lambda_0/2$.

Initially, a pre-calculated threshold value had been used for transition detection but it could only work well for a specified regime and caused erroneous detection as soon as the SM regime changed or when the signal was noisy. Then, a wavelet transform was employed to ameliorate the robustness of this detection but this method was found to be limited to moderate feedback [41]. Afterwards, transition detection had also been done by computed Holder exponent using differential evolution algorithms [42]. It enabled us to differentiate the shape of noisy signals in order to recover the displacement but this approach involved very long computations.

Hence, a faster unique transition detection algorithm has now been conceived for a LD self-mixing displacement sensor that aims to cover both weak and moderate feedback regimes. This method, presented below, results in a fully automated algorithm that converges to the optimum threshold level needed to correctly detect the signal fringes and can differentiate between the purely sinusoidal, the saw-tooth, the hysteresis affected saw-tooth, or the fringe-free SM signals.

III.2.5 Principle of Adaptive Detection

In the previously described standard approach for transition detection, the manually adjusted threshold value is introduced to ascertain if the variations in the differentiated signal correspond to a real shift in phase or if it is only a noise. This fixed threshold value, however, cannot be reliable in case of SM regime change as the peak to peak (p-p) fringe amplitude of the OOP decreases with increase in the feedback level C (Fig. III:19). If a small threshold value is selected for a moderate feedback regime to compensate for the its smaller p-p signal then it results in false detections for the case of a weak feedback regime signal that has larger p-p fringe amplitude. Likewise, a higher threshold value chosen for the weak feedback signal would miss the transitions in case of a moderate SM signal. So, an automated threshold is necessary that adapts to the changing input OOP signal no matter what the feedback regime may be.

For this purpose, the adaptive transition detection algorithm starts with a very small threshold value (5% of the peak amplitude of the differentiated phase Δx_F).

The advantage of this small starting value is that the algorithm shall be able to detect the transitions even for high values of C, i.e. small p-p fringe amplitudes of moderate regime OOP signals. At the same time, if ever no transitions are detected then the SM signal is classified as a strong regime signal and no further processing is done. The obvious drawback of such a small threshold value is the possibility of detecting false transitions for those signals that shall have higher p-p fringe amplitudes but these can be processed in the next steps.

In the following sub-sections, further processing catering to both moderate and weak feedback regimes will be considered separately. The algorithm then assumes a target displacement of at least $\lambda_0/2$ for a proper detection as any variation in displacement smaller than $\lambda_0/2$ would never appear as a fringe in the SM signal. Fig. III:20 presents as a block diagram the steps and decisions undertaken by this algorithm relevant to each SM regime.

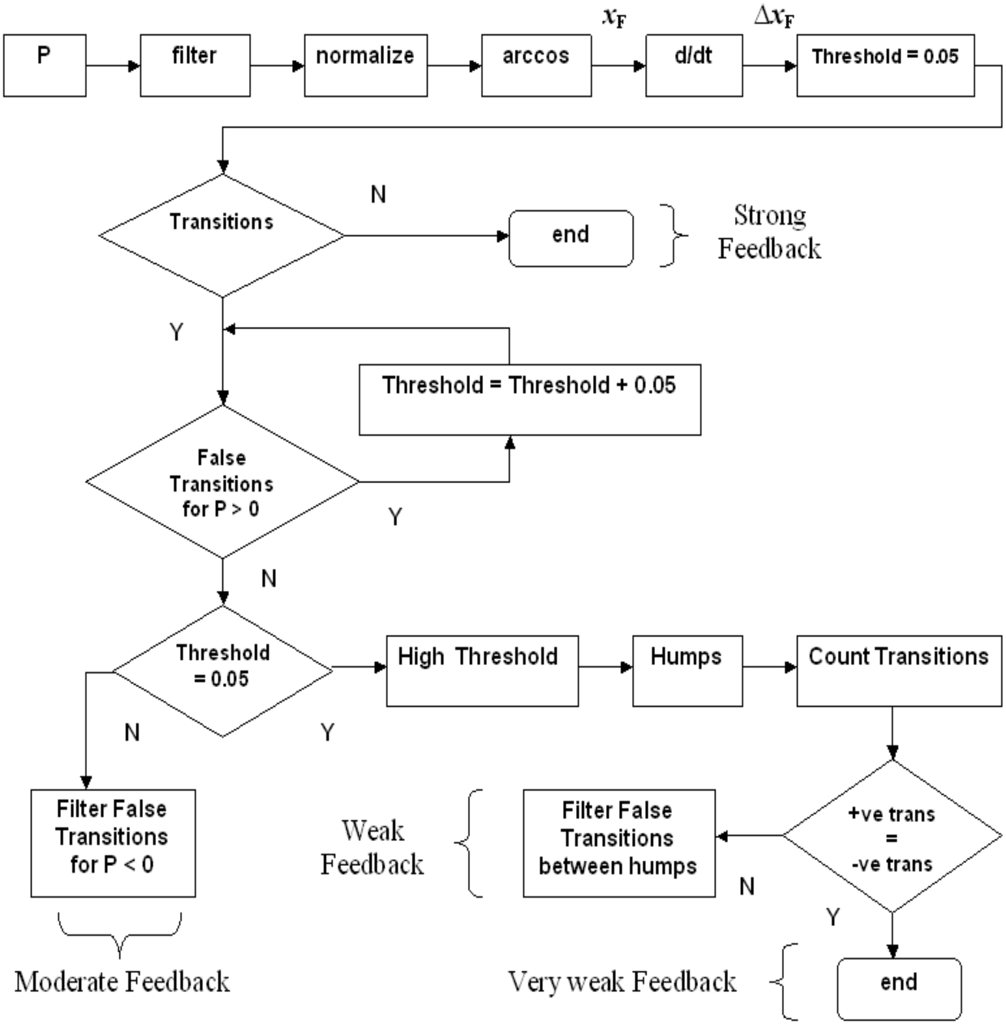

Fig. III:20. Block diagram of Adaptive Transition Detection Algorithm.

III.2.5.a Moderate Feedback Regime

For this regime, it must be noted that even a small value of threshold is not able to compensate for the difference in amplitude of the fringes corresponding to the two halves of hysteresis affected SM signals (Fig. III:19), where the upper and lower halves represent the target displacement away and towards the LD respectively.

For this purpose, the algorithm uses the relatively smaller fringes found in the upper half of a hysteresis affected SM signal (P(t)>0) as a starting point and then the lower half (P(t)<0) is treated separately to provide a correct result.

III.2.5.a.1 The case of P > 0

The transitions obtained for a given threshold value are saved along with the sign of the OOP signal corresponding to the instant of the fringe transition detection. So, once all transitions for a given OOP signal at a given threshold are saved, the algorithm in its first step tests only those transitions which were obtained for P >0. For a correct threshold value, only the negative transitions should be obtained for the SM signal corresponding to P > 0 (Fig. III:21 c).

If ever alternating positive and negative transitions are obtained for P>0 then it signifies that the threshold is too low (Fig. III:21 a). As a consequence, the threshold is incremented by 5% (as shown in Fig. III:20). This loop continues until the threshold value becomes large enough to rule out the possibility of a false transition detection for the positive half of the OOP signal in moderate feedback regime (Fig. III:21 a, b and c).

However, it has been noted that for SM signals with very little hysteresis only, certain false transitions may remain. These tend to be sporadically placed and are sandwiched between correct transitions [… x x y x x…] where 'x' represents a correct transition and 'y' a false transition. So these can be easily identified and removed for the moderate SM signal corresponding to P>0.

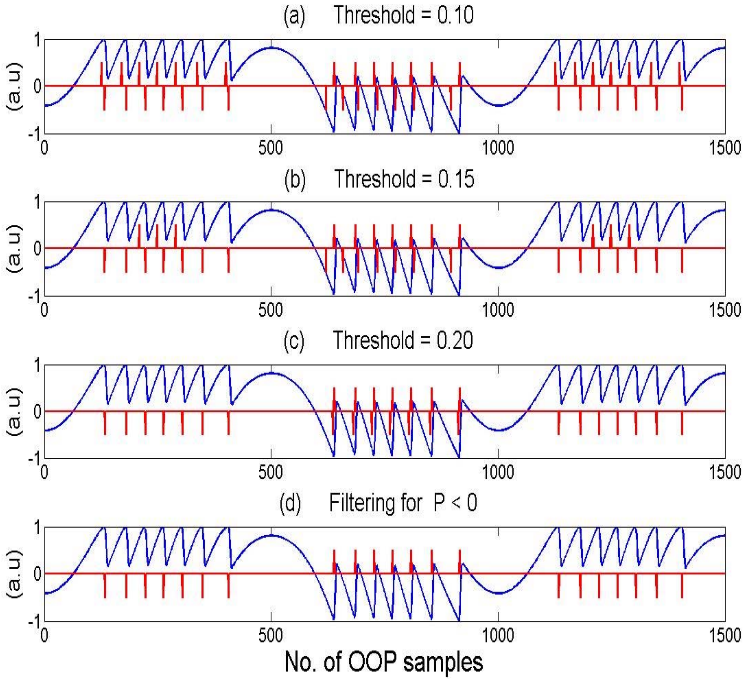

Fig. III:21. (a) shows alternating transitions for P > 0 segments at Threshold = 0.10 for C = 4, (b) and (c) present the effect of increasing Threshold on the P > 0 segments while (d) shows the removal of false transitions for P < 0 segment.

It is reminded that in case of a SM signal obtained under moderate feedback regime for a random displacement, any true half-wavelength displacement variation will result in a true fringe in the SM signal. These positive or negative half-wavelength variations can be observed as distinct fringes. The Fig. III:22 of an experimental random SM signal shows these in red circles. So, a true negative transition is found for the P>0 section at around 1000th OOP sample.

Now, if ever, a positive transition were to be found in between true negative transitions for the P > 0 section (shown in dashed black circle on Fig. III:22), the [… x x y x x…] condition can identify it as a false transition and remove it.

Thus, a true positive transition (as shown in the red circle around 15000th OOP sample) would never be treated in the P>0 case as it would always lie in the P<0 section for the moderate feedback regime. Hence, the [… x x y x x…] condition allows us to remove any false transition caused by an abrupt local variation in the P>0 section of the SM signal.

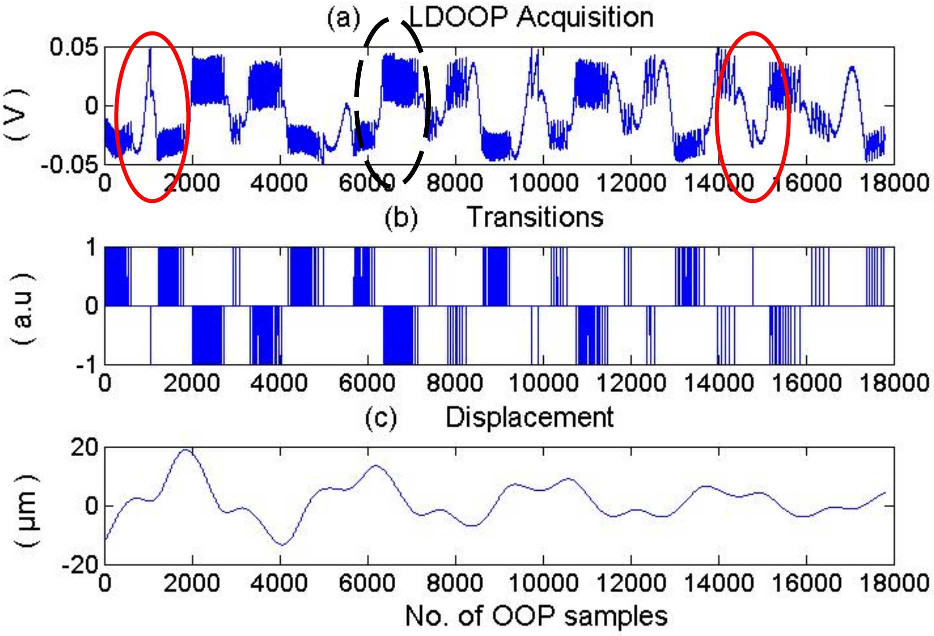

Fig. III:22. Experimental random SM signal (a), correct transition detection (b) and random displacement reconstitution (c) of a concrete structure.

III.2.5.a.2 The case of P < 0

The previous step provides a good detection for P>0 case by converging to an adequate threshold value (which is Threshold = 0.20 for the Fig. III:21 c). However, as expected, this value is not adapted to the relatively higher p-to-p amplitude of the fringes in the lower half of the signal, i.e. the moderate SM signal corresponding to the P<0 segments (Fig. III:19 and Fig. III:21). Thus, false transitions of opposite sign still exist and are then detected in this lower half and simply discarded (Fig. III:21 d).

These steps thus provide an overall correct detection for signals even with large hysteresis (where the upper and lower halves with saw-tooth fringes remain distinctly away from each another).

III.2.5.b Weak feedback Regime

The SM signals corresponding to the weak-feedback levels ($C < 1$) do not exhibit hysteresis (Fig. III:19). These tend to be purely sinusoidal in shape for $0 < C < 0.2$ and take on a relatively saw-tooth like shape for increasing C up to the value of 1. The p-to-p fringe amplitude of these normalised signals covers the whole of the [1 -1] range.

In order to differentiate the weak from the moderate regime, the sequence of transitions detected for the initial threshold value of 5% is analysed. Actually, as the weak SM fringes cover the whole of the [1 -1] range, so this makes it impossible to separate the OOP fringes into two halves of $P>0$ and $P<0$. So, even in the presence of alternating correct and false transitions, the test of the presence of false transitions for $P>0$ fails (see *Fig. III:23* where only negative transitions are observed for the test condition of $P>0$). This apparent failure to observe alternating correct and false transitions, even for a very small threshold value (indicated by the test condition ‘Threshold = 0.05’ in Fig. III:20), can be used to trigger the section of the algorithm that treats the weak feedback regime signals.

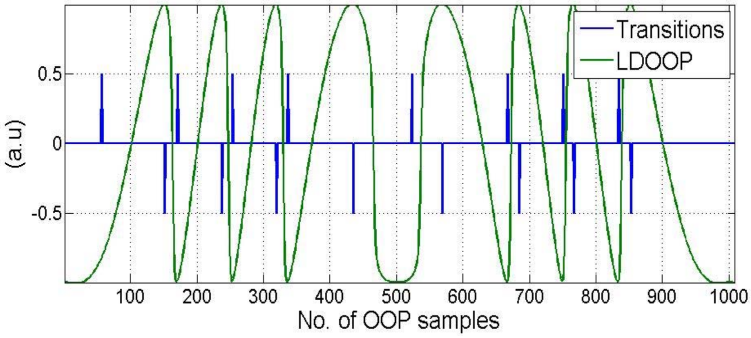

Fig. III:23. The alternating true and false transitions that can not be separated based on $P > 0$ for $C = 1$ and Threshold = 0.05, for a Laser Diode Optical Output Power (LDOOP) signal..

III.2.5.b.1 High Threshold

In order to correctly treat the higher p-to-p amplitudes of the weak SM fringes ($C < 1$), the first step in this section is then to assign a high threshold value. This alone clears all the false transitions for the weak SM signals with C close to 1 (Fig. III:24). However, when C is smaller this tends to be insufficient as many false transitions remain and further processing is then needed to remove these.

III.2.5.b.2 Hump Detection

As the lack of hysteresis makes it difficult to determine the direction of displacement by comparing the sign of P so another method needs to be devised. The moment of change in the displacement direction can allow one to correctly identify the adequate positive or negative transitions corresponding to a movement towards or away from a target.

At this moment of direction change, the central zone of the OOP (the so-called ‘hump’) which contains no fringes can be distinguished from the rest of the signal as it occupies the largest transition-free space for a given SM signal and is book-ended by opposite signed transitions.

The algorithm finds out these humps by selecting the zone with the maximum number of samples between two transitions. This, however, in itself is not sufficient as the upper and lower humps tend to be different in width so a next step designates all those transition-free regions into a hump array that are comparable to the maximum hump.

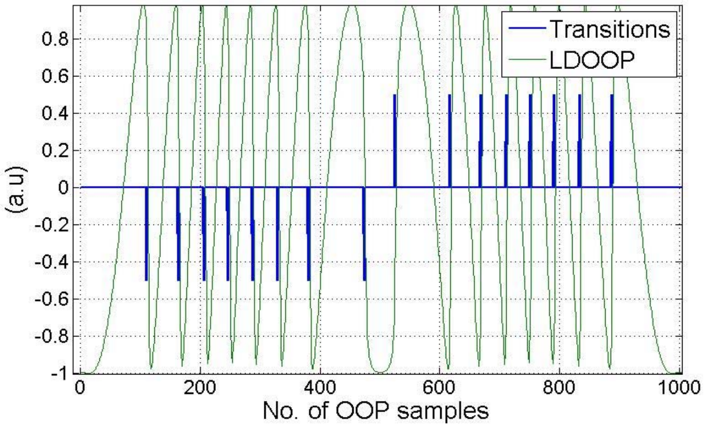

Fig. III:24. Effect of high threshold value (Threshold = 0.45) on the weak SM signals which leads here to perfect detection for C = 1.

III.2.5.b.3 Transition counting

Once the humps have been identified, the algorithm starts the task of eliminating the existing false transitions by counting the number of positive and negative transitions between humps.

2 cases are then considered.

III.2.5.b.3.1 Positive Transitions ≠ Negative Transitions

The more the value of *C* approaches 0.2 (i.e. the very weak feedback regime), the more the shape of SM fringes loses its sawtooth aspect and tends to be sinusoidal. As an example, Fig. III:25 shows almost sinusoidal fringes placed between sawtooth-like fringes.

Each of these middle fringes causes a correct and a false transition (due to the symmetry at the top and the bottom of the fringe). However, the presence of saw-toothed shaped fringes results in the fact that there are always fewer false transitions within a given inter-hump zone as compared to the correct transitions. So these fewer transitions can thus be removed.

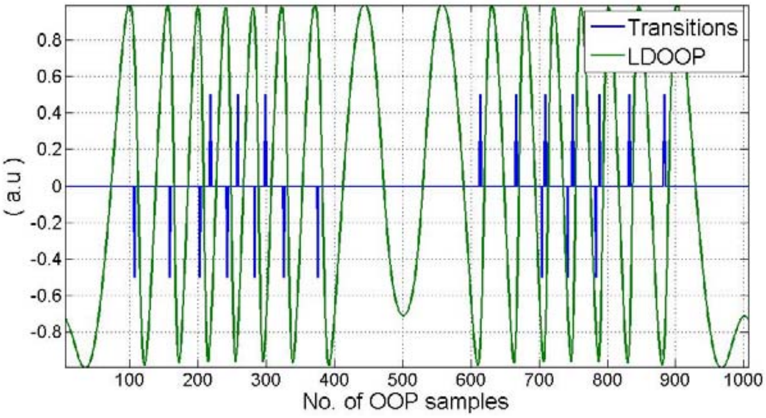

Fig. III:25. Effect of some sinusoidal fringes which lead to imperfect detection for C = 0.5 and threshold = 0.45.

III.2.5.b.3.2 Positive Transitions = Negative Transitions

This is case of 0<C<0.2 where the SM signal fringes are sinusoidal in shape thus resulting in equal number of positive and negative transitions within a region (Fig. III:26) which is supposed to contain only one type of transitions. So, only displacement amplitude can be recovered and directional information is lost. Thus, we encounter the same issue of directional ambiguity seen in classical interferometers. This very weak feedback regime can thus be identified as indicated in Fig. III:20.

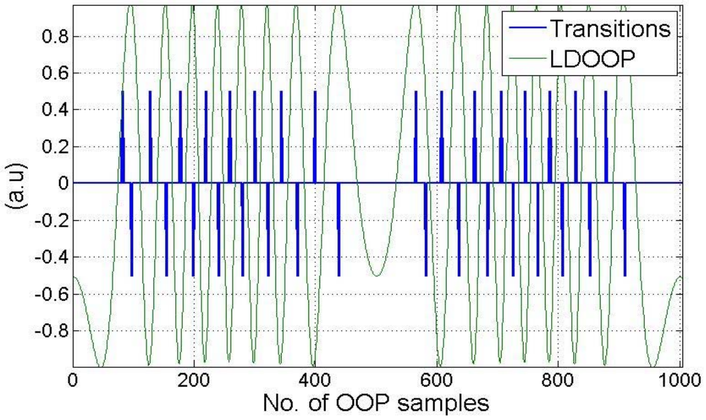

Fig. III:26. All sinusoidal fringes which lead to equal number of positive and negative transitions for C = 0.05.

III.2.6 Algorithm Validity

Using the behavioral model to generate SM signals for a given excitation signal, the adaptive transition detection algorithm has been theoretically validated for a variation of C from C=0.2 to C=100. Furthermore, the algorithm successfully distinguishes between the very weak, weak, moderate and strong feedback regime signals and then adapts to the relevant signal processing needed.

Using this algorithm, not only simulated sinusoidal but also random displacement signals have been correctly reconstituted. Fig. III:27 presents a random displacement signal where a maximum absolute error of less than 100nm is observed for a SM signal assuming a LD at λ=660nm. It is to be noticed on Fig. III:27 b that the error approaching such a value is due to a local variation in the random excitation signal of less than λ/2 i.e. where no SM fringes exist. However, as soon as the excitation signal covers a variation of at least 2λ, this error reduces to less than 20nm. The error is even smaller for the sinusoidal target displacement, at less than 50nm (Fig. III:28).

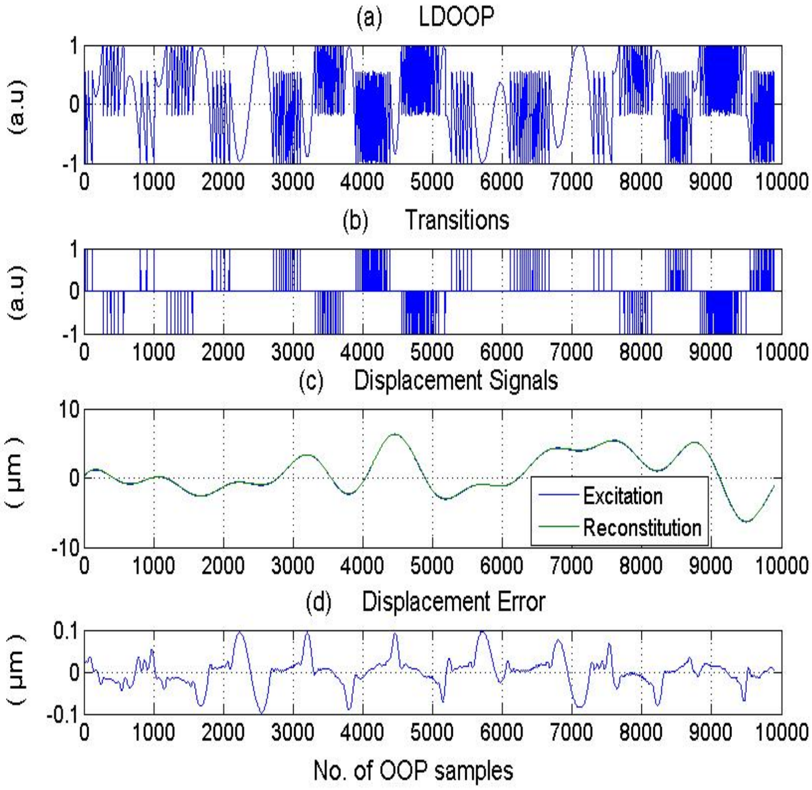

Fig. III:27. A simulated SM signal (a) and its correct transition detection (b) for a random displacement excitation and its reconstitution (c). The error between the excitation and reconstituted signals is shown in (d).

III.2.7 Experimental Results

This section details the transition detection of SM signals obtained with various Fabry Perot LDs of different wavelengths and with varying operating conditions. In order to modify the coupling factor *C*, the distance to the target D_0 has notably been changed by sliding the LD assembly towards or away from the target along the optical bench.

The next section shall present the comparison of displacement reconstitutions of various SM signals with respect to the reference displacement measuring instrument signals. Typical experimental set-up is the same as already presented in Fig. III:15.

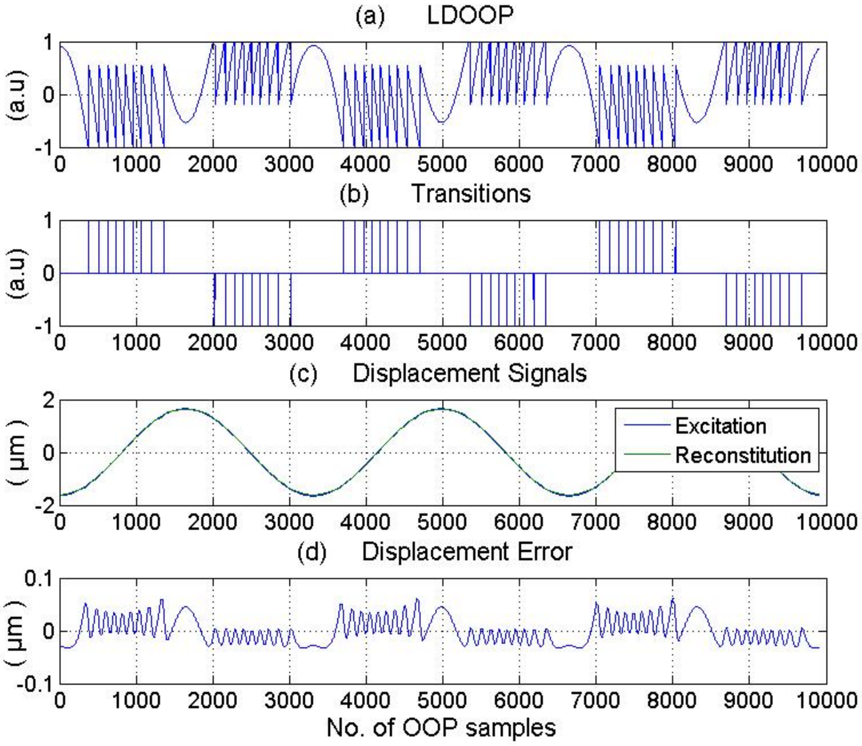

Fig. III:28. A simulated SM signal (a) and its correct transition detection (b) for a sinusoidal displacement excitation and its reconstitution (c). The error between the excitation and reconstituted signals is shown in (d).

III.2.7.a Transition Detection

Correct transition detection for various target signals is presented below.

III.2.7.a.1 Sinusoidal SM Signals

Fig. III:29 shows moderate SM signals presenting strong hysteresis obtained with a 1310nm DFB LD (Mitsubishi ML776H11F) for with D_0=71cm. The approximate values of C, estimated by comparing with the behavioural model [81], for signals shown in Fig. III:29 (a), (b) and (c) are 32, 13 and 8 respectively. The algorithm has been able to detect all of the fringes in these signals.

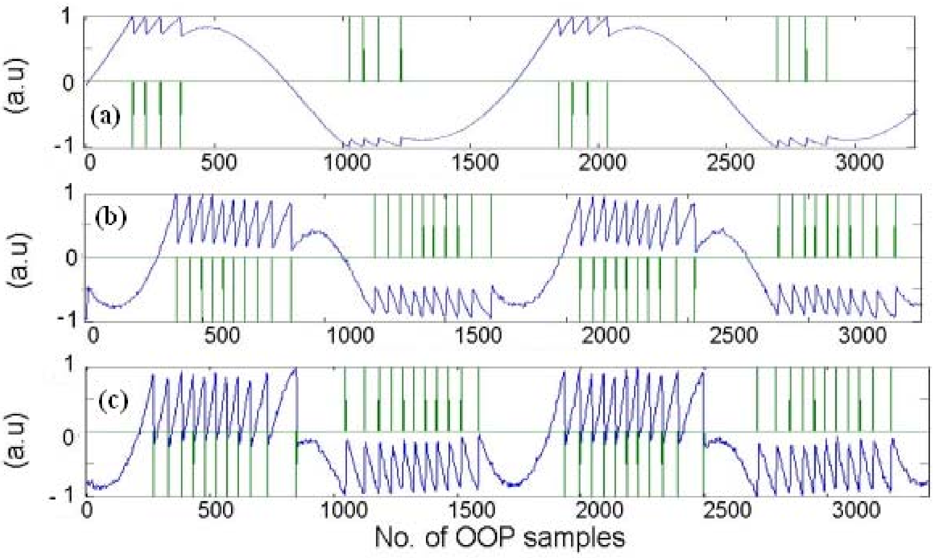

Fig. III:29. Experimental moderate feedback SM signals with decreasing hysteresis and correct detection of all SM fringes.

Using a visible LD working at 660nm with $D_0 \approx 10$cm, a weak SM signal has been tested (Fig. III:30). The algorithm rightly identified it as a weak regime signal. Once again, all of the fringes have been detected, even if the shape of the SM signal is totally different as compared to the signals of Fig. III:29 (no hysteresis, larger p-p amplitude of the OOP fringes). The optimisation procedure indicated in [39] found a value of $C \approx 0.64$ for this SM signal.

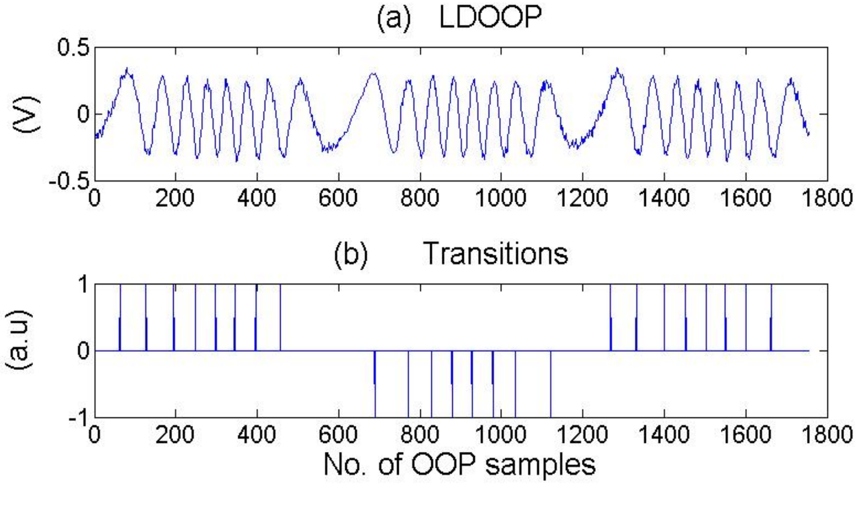

Fig. III:30. Experimental weak feedback SM signal (a) and correct detection (b) of all SM fringes.

III.2.7.a.2 Defocused SM Signal

In order to test the robustness of this algorithm, an experimental SM signal was acquired (Fig. III:31 a) by defocusing the optical lens of the laser (Hitachi HL7851G with λ_0=785nm) that results in a decrease of the feedback power. It was then necessary to use the low-pass averaging filter represented in the block diagram of Fig. III:20. Once again, all SM fringes have been properly detected after the filtering.

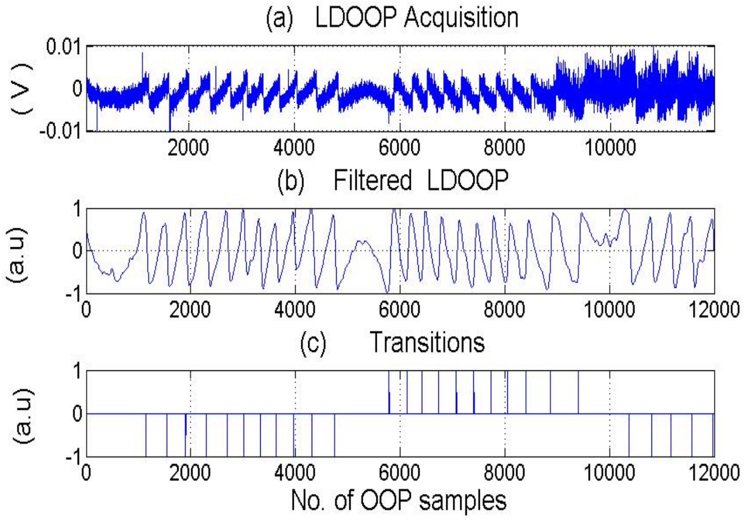

Fig. III:31. Experimental noisy weak feedback SM signal (a) and correct detection (b) of all SM fringes.

In fact, the defocusing of the optical lens shall result in the decrease in the feedback power of the optical beam. This is observed as a decrease in the peak-to-peak amplitude of the SM signal. The same is brought forward by Fig. III:32 that shows 3 experimental SM signals obtained in the lab for the same target excitation and distance between the target and the Laser diode, but where the focusing of the beam on the target surface has been changed.

Clearly, the more we defocus, the more the peak-to-peak amplitude of the SM signal decreases in amplitude. However, as the electronic noise of the system remains the same so this decrease in the amplitude of the signal results in a decrease in Signal to Noise ratio (SNR).

So, we observe here that the red-colored SM signal is the most defocused and has the poorest SNR, where as the blue-colored SM signal is the most focused and has the best SNR for these 3 experimental acquisitions.

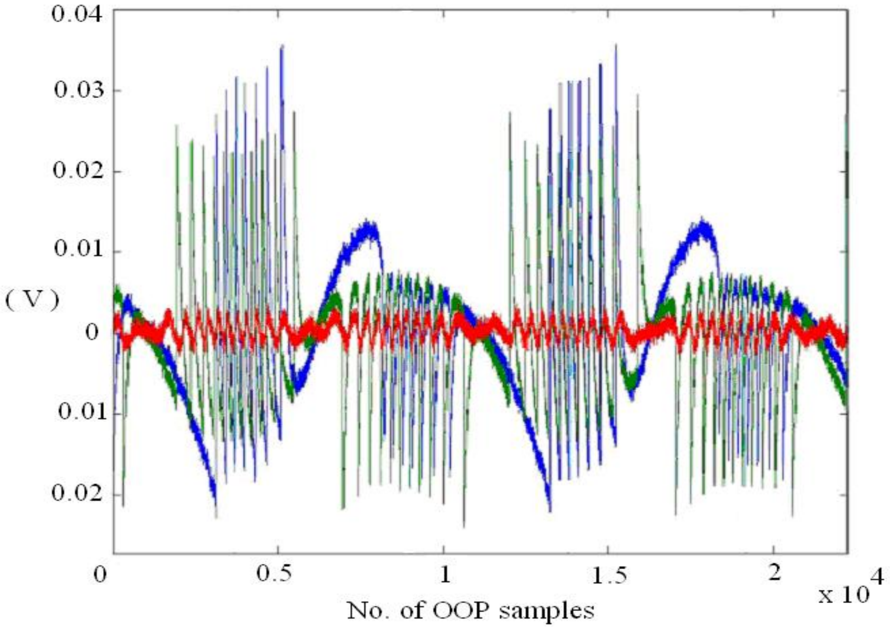

Fig. III:32. Three experimental SM acquisitions that have the same LD to Target distance and the same target excitation amplitude but with different focalisation of the Laser beam spot on the target surface, where the red-colored-signal is the least focused and the blue-colored signal is the most focused among the three.

III.2.7.a.3 Random SM Signal

The algorithm has also been used in conjunction with the PUM to measure the random displacement of a concrete structure hit with a hammer. The correct transition detection and the reconstituted displacement for the random SM signal obtained by a LD with λ=1310nm are shown in Fig. III:33.

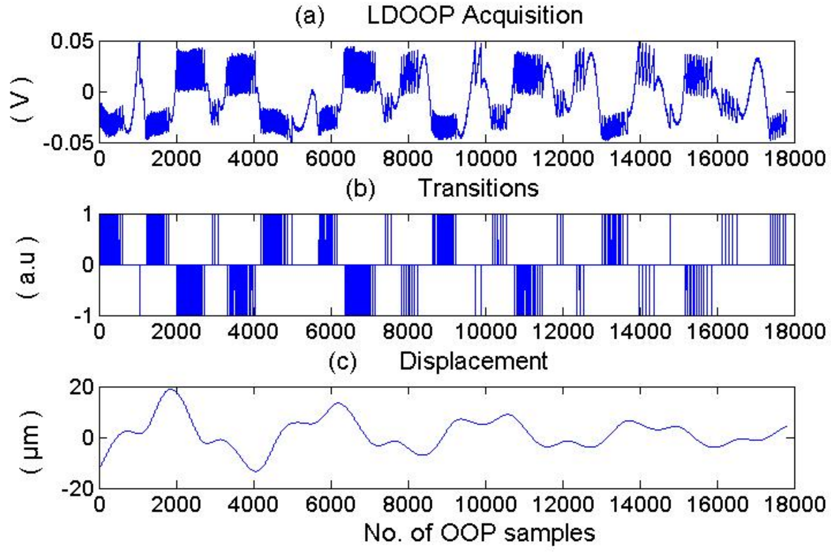

Fig. III:33. Experimental random SM signal (a), correct transition detection (b) and random displacement reconstitution (c) of a concrete structure.

III.2.7.a.4 Strong Regime Signal

As an example of an experimental transition-free signal, Fig. III:34 presents a SM signal in the strong feedback regime for a random excitation of the target. The signal has been acquired using the 1310nm DFB LD under the same set-up as shown in Fig. III:15.

Here, as expected, the algorithm correctly distinguishes this signal as a strong regime signal because no transitions are detected, as the signal in this regime is totally fringe-free. The SM signal follows the excitation signal *g(t)* driving the PZT. The reference measurement by the capacitive sensor *r(t)* verifies this behavior. The random target displacement is being closely followed by the strong regime SM signal.

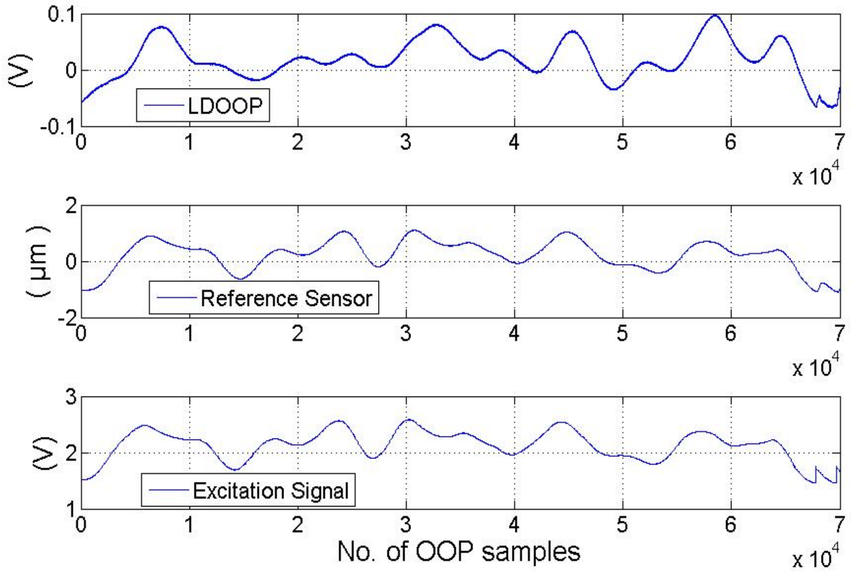

Fig. III:34. Experimental strong feedback SM OOP signal, the PZT excitation signal, and the reference sensor signal. No transitions were detected by the algorithm for this OOP.

III.2.7.a.5 Mixed-Regime Signal

A change in the target displacement amplitude may cause a change in SM regime from moderate to strong feedback or vice versa [41]. Thus, a given SM signal may contain both of these regimes as a result of displacement variations. Fig. III:35 presents such an experimental signal for a vibrating concrete structure targeted with a LD emitting at 1310nm. The algorithm has successfully been able to treat such a mixed-regime signal where it correctly identified and detected the moderate regime sections and no false transitions were introduced for the strong regime sections.

III.2.7.b Displacement Measurement.

This newly presented transition detection algorithm incorporated into the phase unwrapping method has then been validated for weak and moderate feedback regimes by using a reference counter measurement and under different experimental operating conditions.

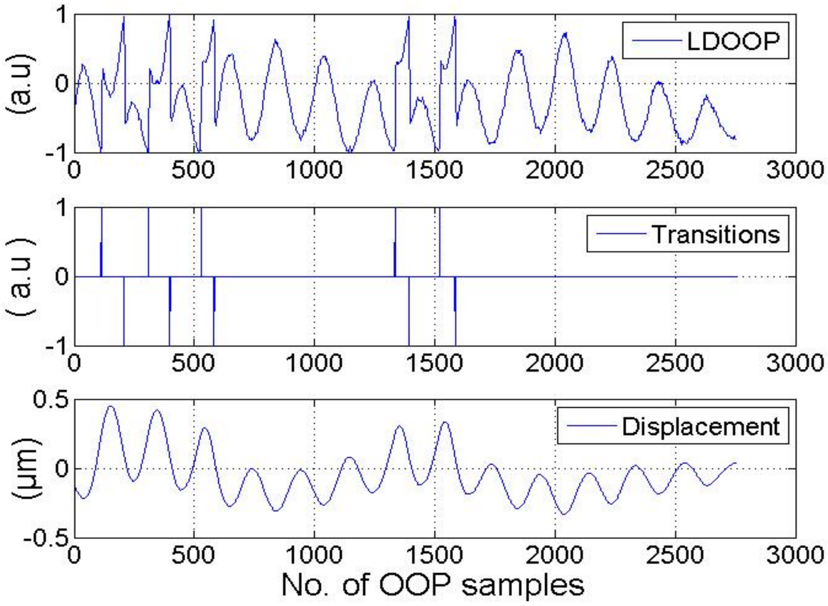

Fig. III:35. Experimental mixed-regime SM signal obtained for a vibrating concrete pillar and the reconstituted displacement using a DL at 1310nm.

III.2.7.b.1 Weak Regime in Free Space

Firstly, the target – a piezoelectric transducer (PZT) from Physik Instrumente (P-752 high precision nanopositioning stage) - was excited with a simple harmonic motion of p-p amplitude of 2.31µm and with a modulation frequency of 83 Hz. Counter measurements were achieved with an integrated capacitive feedback sensor for direct-motion metrology.

The generated SM signal in the weak feedback regime as seen on Fig. III:36 [16] was then acquired using the red LD of λ = 660nm. The algorithm correctly identified the signal as a weak regime signal and then detected all SM fringes. The reconstituted signal has an error of 29 nm at its maxima with respect to (w.r.t) the excitation signal.

III.2.7.b.2 Weak Regime in Optical Fibre

Secondly, another weak SM signal was obtained within an optical fibre under strain [88]. This SM signal was thus affected by dynamic strain variations, the target being a Fibre Bragg Grating (FBG) included in the optical fibre that acted as a selective mirror at a wavelength around 1309nm.

The algorithm successfully treated the signal and the reconstituted phase was used to calculate the strain with a target modulation frequency of 88 Hz (Fig. III:37). The final error was less than 1% w.r.t a commercial strain gauge. Using the optimization procedure of PUM, an approx. value of C=0.75 has been calculated for this signal.

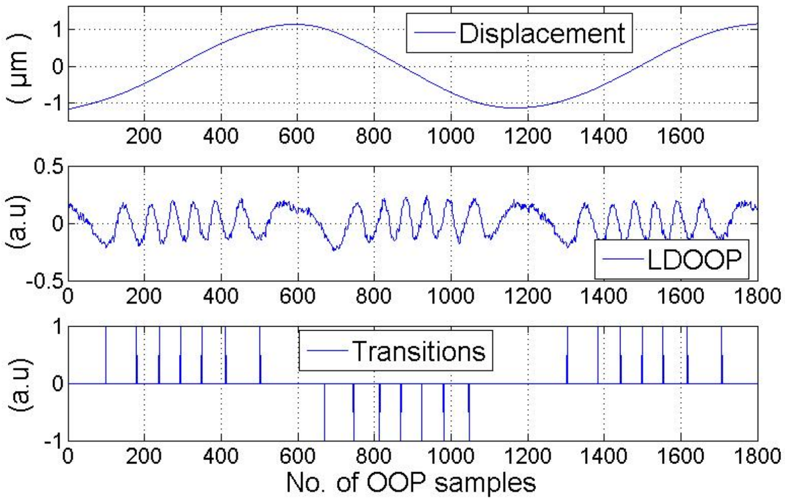

Fig. III:36. Reconstituted displacement of an experimental SM signal with a Red LD and its correct transition detection.

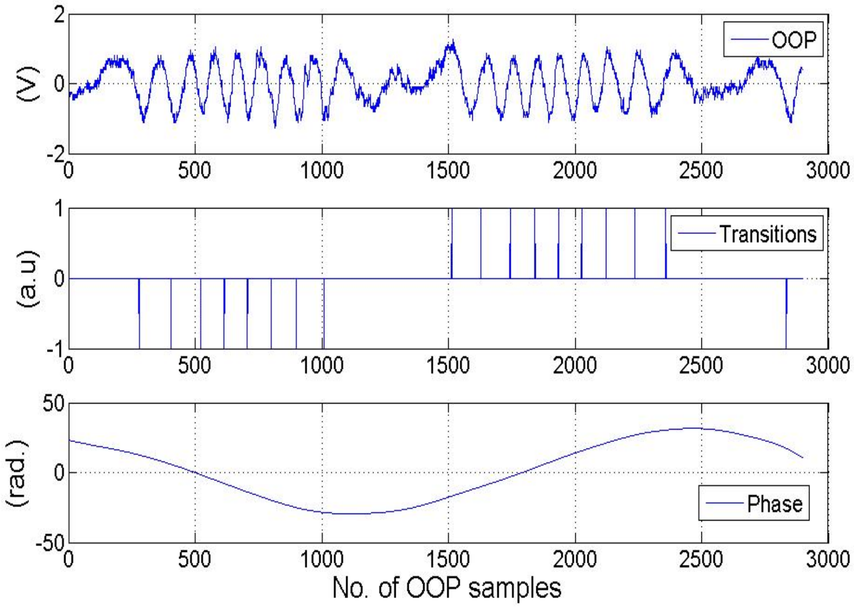

Fig. III:37. Experimental weak feedback SM signal obtained within an optical fiber stuck on a metallic plate, its transition detection and the resultant phase that has been used to measure the strain of the plate.

III.2.7.b.3 Moderate Regime Signals

Thirdly, the HL7851G laser diode emitting at 785nm was used to obtain a moderate SM signal for a p-p target displacement of 5µm and with a target modulation frequency of 330 Hz. Another commercial PZT from Physik Instrumente (P753.2CD), having an accuracy of 2nm and also equipped with an integrated capacitive feedback was used as the target. The experimental SM signal had a large hysteresis (with C≈17, found by using [81]). The algorithm correctly identified it as such and detected all the fringes (Fig. III:38 a). The reconstituted displacement has an error of 86 nm at its maxima w.r.t the reference PZT sensor (Fig. III:38 b).

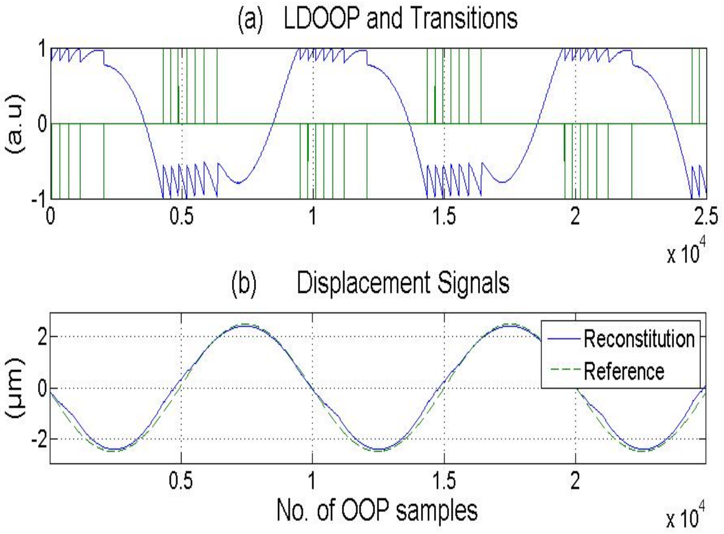

Fig. III:38. Experimental moderate feedback SM signal and its transition detection (a), the reconstituted and reference sensor displacements (b).

Using the same set-up as for the above-mentioned third case, another LDOOP signal has been acquired (Fig. III:39 a) for a target displacement of 1.715µm. This signal has lesser hysteresis (with C≈6) as compared to the previous signal. The algorithm still treated it as a moderate SM signal and found all the transitions to reconstitute a displacement with an error of 37 nm at its maxima w.r.t the reference PZT sensor (Fig. III:39 b).

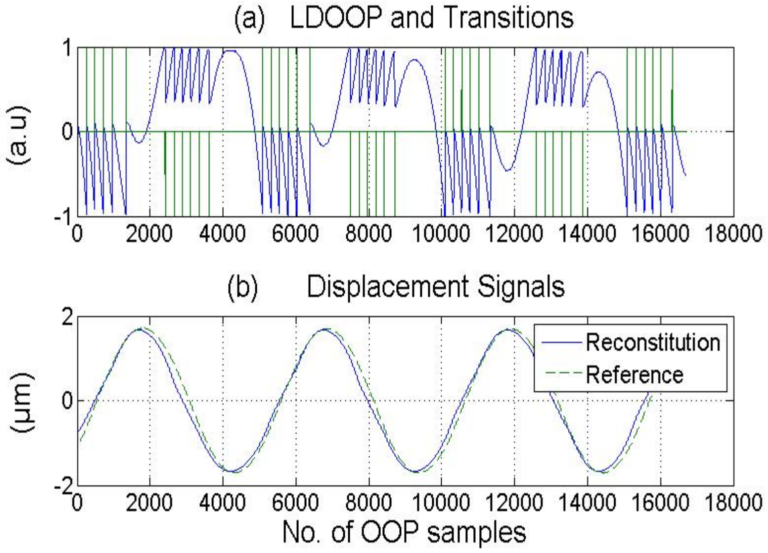

Fig. III:39. Experimental moderate feedback SM signal with lesser hysteresis and its transition detection (a), the reconstituted and reference sensor displacements (b).

III.2.7.b.4 Random displacement SM signal

Lastly, a random displacement reconstitution for an experimental SM signal (Fig. III:40 a) has been compared with the PZT signal. The max. error is of 83nm for a target excitation frequency of 2.5Hz (typical for geophysical applications) and LD wavelength of 785nm. Once again, all transitions have been successfully detected (Fig. III:40 b).

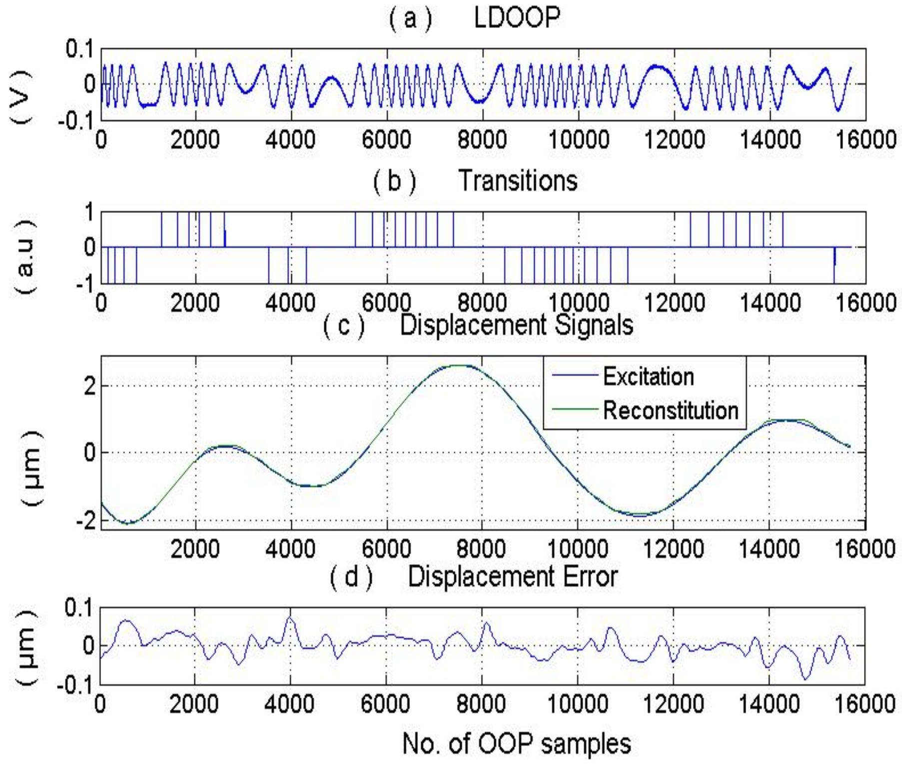

Fig. III:40. An experimental random displacement based SM signal (a), correct transition detection (b) and its reconstitution (c). The error between the excitation and reconstituted signals is shown in (d).

III.2.8 Conclusion

In this section, we have presented a new algorithm that replaces the static fringe transition detection technique of the phase unwrapping method with a dynamic one that adapts itself to changes in the shape of the self-mixing fringes caused by variations in optical feedback. It then enables us to perform displacement measurements based on optical feedback interferometry for lasers subject to weak as well as moderate feedback regimes.

This algorithm is able to differentiate between the very weak feedback (sinusoidal), the weak feedback (slightly asymetric), the moderate feedback (sawtooth-like with hysteresis) and strong (fringe-less) regimes. Even when the shape of the signal strongly varies from one regime to another, notably in terms of p-p amplitude of the fringes of the optical output power, this algorithm converges automatically to an optimum threshold level required to detect all the self-mixing fringes. It has been tested successfully for these self-mixing regimes. Experimental validation has been done by using various lasers operating at different wavelengths, in free space conditions and within an optical fiber, as well as for defocused lasers. Moreover, this method has been successfully tested for random and sinusoidal displacements at different target vibration frequencies. It covers a wide range of applications from geophysics (1-2 Hz) to mechatronics (up to 2.5kHz).

The algorithm paves the way for a universal signal processing for all self-mixing regimes and shall lead to the development of a real-time System-in-Package (SiP) for a self-mixing displacement sensor.

The next section is, however, dedicated to the possibility of adding an adaptive optics based component to our sensor. Such a device allows us to electronically control the optical feedback into the active laser cavity and so can be used to maintain the self-mixing signal in a favorable feedback regime.

III.3 Use of Adaptive Optics in Self-Mixing

III.3.1 Introduction

As seen in the previous section, the influence of the feedback parameter is predominant for metrological measurements using the Self-Mixing. The different regimes need specific signal processing to extract the displacement information and each regime comes with its own challenges. For example, the sinusoidal fringes of the weak feedback regime result in directional ambiguity whereas the fringe-loss in the moderate feedback regime needs compensation of the fringe-loss.

These issues, however, can be avoided by controlling the optical feedback. Thus, if we are able to adjust the feedback such that the parameter C remains greater but close to 1 then a fringe-loss and saw-tooth like SM signal can be obtained which is the easiest to process in terms of fringe detection as well as displacement reconstruction.

In this section, a study on the use of an Adaptive Optics (AO) element in the form of a liquid lens (LL) is presented for the case of Self-Mixing based metrological measurements [93]. The LL maintains the SM phenomenon in the moderate feedback regime with no hysteresis, thus leading to very good vibration results. The set-up has also increased the dynamic range of the distance between the target and the LD. Target vibration signal reconstitutions present a max. error of λ/16 over a distance range of 6.5 cm to 265 cm as compared to a commercial sensor.

III.3.1.a Adaptive Optics

AO was originally used in large telescopes for the compensation of the effects of atmospheric turbulence [94], but a number of applications for the enhancement of optical measurement sensors [95] and techniques [96] have been developed in the last years. In our set-up, a liquid lens has been used whose focal length can be controlled by applying an external voltage [97]. A LL is thus far superior to a traditional lens as focusing can be achieved with any mechanical contact and its electronic control can lead to an automation of the complete set-up.

III.3.1.b Use in Moderate feedback Regime

Displacement measurements are generally performed in the moderate feedback regime (corresponding to $C>1$). The signal is then characterized by hysteresis and even fringe loss – caused by variations of C with D_0 and/or the feedback level - that may result in a decrease in accuracy. However, the marked slope of the fringes indicates the direction of motion of the external reflector.

An efficient method has previously been proposed that keeps the operating point of the SM interferometer fixed at the half-fringe value [27]. As a consequence, there is no influence of fringe loss thus avoiding sophisticated signal processing. However, this approach requires an objective lens that collimates the LD beam onto a second focusing lens placed at a distance of 40cm in order to project the LD beam spot on the target. In addition, an optical attenuator has to be inserted in the optical path to prevent the optical feedback from becoming excessive. Furthermore, the absolute distance to the target D_0 has to be measured at the beginning of each measuring session. Our approach consists in replacing the focusing lens and the attenuator by the use of AO in the shape of a LL and a simplified electronics (Fig. 1). This results in strongly increasing the measuring range of $D_{0.}$

III.3.2 Experimental Set-up

The experimental set-up diagram, where the Liquid lens is used to direct the laser beam on to the piezo actuator surface, is presented in Fig. III:41.

In our set-up, an ARCTIC 416SL V3 liquid lens from Varioptic has been used. In this lens the curvature of the interface between two immiscible liquids of different refractive indices is controlled using an external voltage [97].

The liquid lens has an optical power ($1/f_{LL}$) variation of –12 dioptre to 18.75 dioptre corresponding to a voltage variation of 30 V to 60 V, where f_{LL} is the focal length of the liquid lens. The LL holding assembly, containing the collimation lens (CL) and the LL, is placed in front of the LD (a Hitachi HL7851G LD with a maximum output power of 50 mW, emitting at λ=785 nm, where λ is the LD emission wavelength).

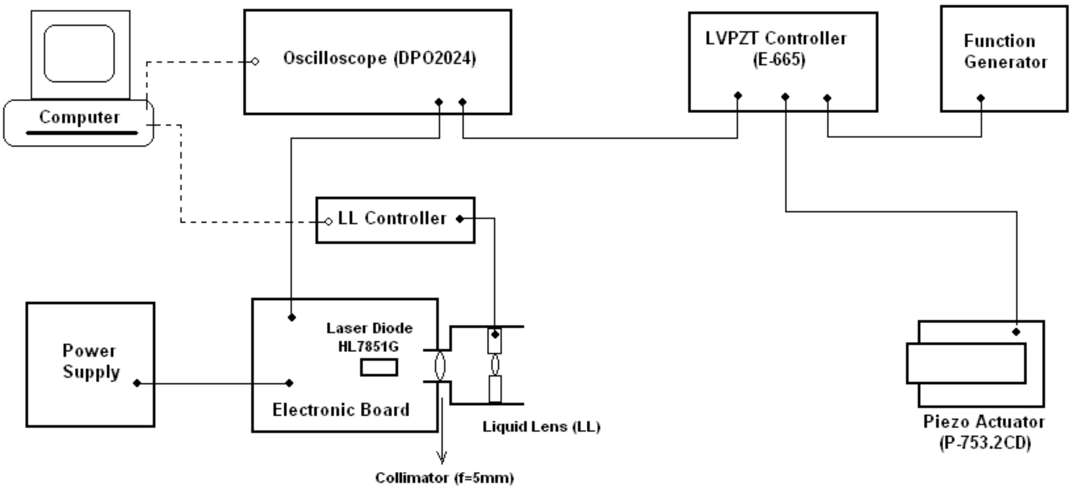

Fig. III:41 Experimental set-up diagram of the Liquid lens focusing the LD beam on to a Piezo actuator surface.

The LL focuses the laser beam onto an oscillating target, which is at a distance D_0 from the LD. The target is the P-753.2 CD piezoelectric transducer (PZT) from Physik Instrumente, equipped with an integrated capacitive sensor for direct-motion metrology having an accuracy of 2 nm. The CL having a focal length f_1=5mm, placed at the distance of d_1=6mm from the LD, concentrates the strongly divergent laser beam onto the LL, placed at a distance d_{CL}=18mm. Such an optical arrangement combines near-distance focusing capabilities with an extended range of focused distances. The f_{LL} can be changed through the LL controller. The built-in monitor photodiode (PD) is used to retrieve the variations in the optical output power (OOP) of the LD (i.e. the SM signal). The OOP signal is then amplified, digitalised and, at present, processed on a computer (PC).

The whole optical set-up stands on an optical table such that D_0 can have a maximum value of 265 cm (limited by the optical table) and a min. value of 5 cm (taking into account the LL assembly plus a minimum focusing distance of 2.5 cm).

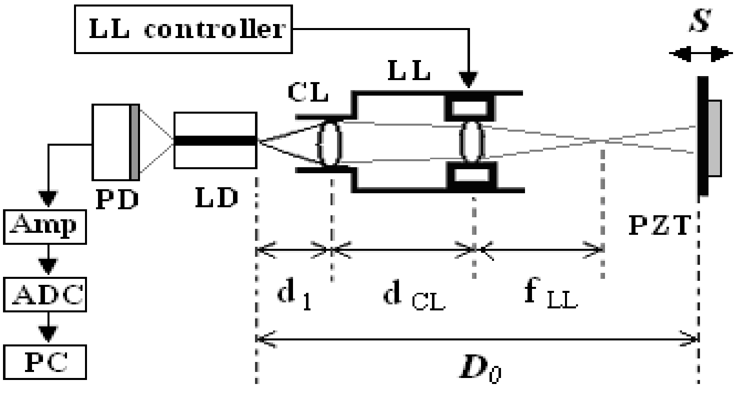

Fig. III:42 Schematic diagram of the experimental set-up for increasing the dynamic range of the distance D_0 for a SM LD vibrometer with a Liquid Lens.

Fig. III:42 indicates the partition of the distance between the LD and the target as well as the acquisition of the SM signal.

In Fig. III:43 is presented a photograph of the LD based SM sensor with the LL where the various components have been enumerated and detailed in the figure legend.

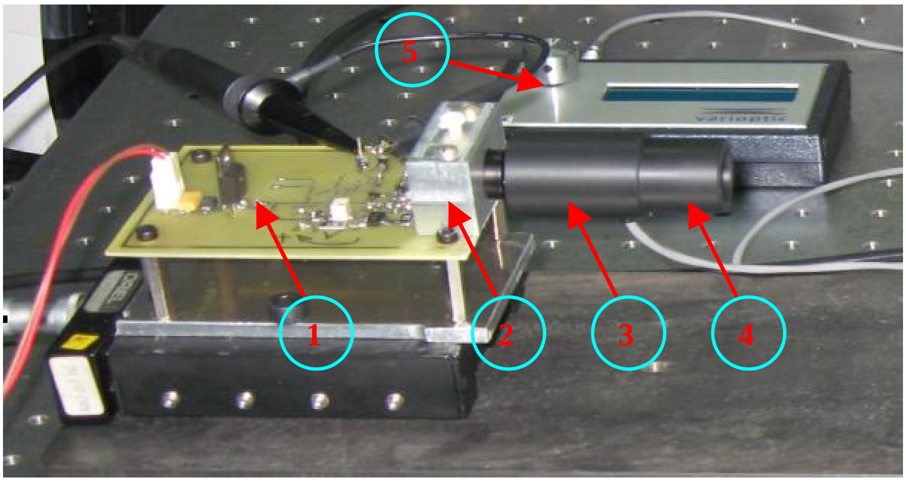

Fig. III:43 Photograph of the SM sensor with the Liquid Lens. (1) is the electronic SM signal acquisition circuit board, (2) is the metallic heat sink that contains the LD package, (3) is the collimating lens assembly, (4) is the liquid lens, and (5) is the liquid lens controller.

III.3.3 Experimental SM Signal Acquisitions

The LL has allowed us to obtain all the possible SM regimes, from the weak to moderate and up till the strong feedback regime. Fig. III:44 presents us the SM signals obtained with a VCSEL working at λ=850nm for D_0 = 91 cm.

It is clear to see that the LL set-up provides a comprehensive control on the feedback level, that in itself has a crucial influence on the SM behaviour for a given sensor to target distance.

Let us now analyse in detail the SM signals obtained for the FP LD at 785nm and D_0 = 78 cm.

The moderate feedback regime SM signals obtained with a variation in the focusing are presented in Fig. III:45. The PZT has been excited with a simple harmonic motion of peak-to-peak amplitude S of 4.25 µm at a frequency of 100 Hz. For this amplitude S, the number of fringes N of the SM signal in every half period of target oscillation should then be 11 ($N = round(2S/\lambda)$), as each fringe represents a displacement of $\lambda/2$. Now, when the laser beam is focused, the signal exhibits a large hysteresis as well as 3 lost fringes (Fig. III:45 (a)). Then, when the LL is used to defocus the beam, the SM signal regains one lost fringe and has comparatively less hysteresis (Fig. III:45(b)). The same happens for Fig. III:45.(c) showing 10 fringes. Further defocusing results in a moderate SM signal without fringe-loss (Fig. III:45.(d)). So, N has been varied here from 8 to the correct value of 11 by the use of LL arrangement.

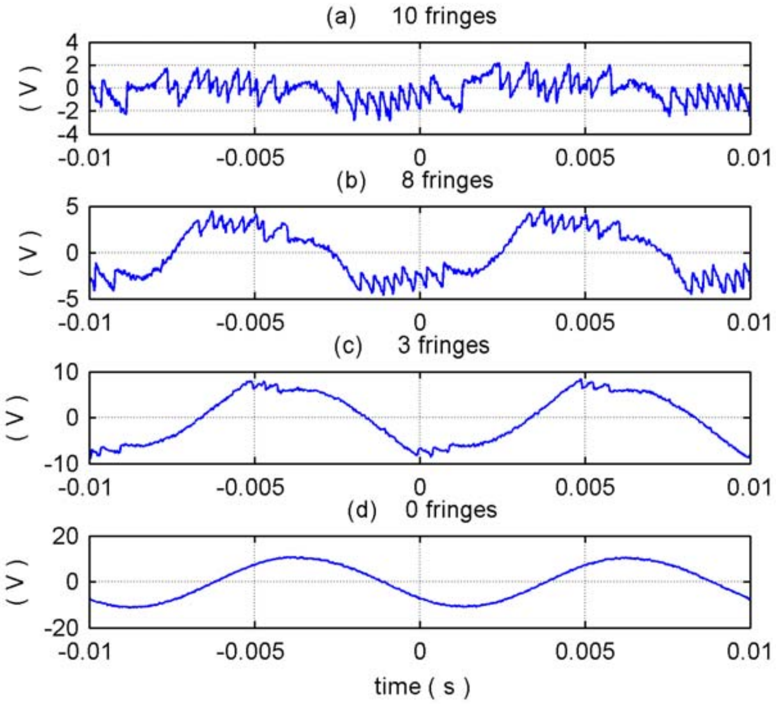

Fig. III:44 Filtered experimental LDOOP for a 850 nm VCSEL that goes from weak (a) to moderate (b-c) to strong feedback regimes (d). D_0 = 91 cm.

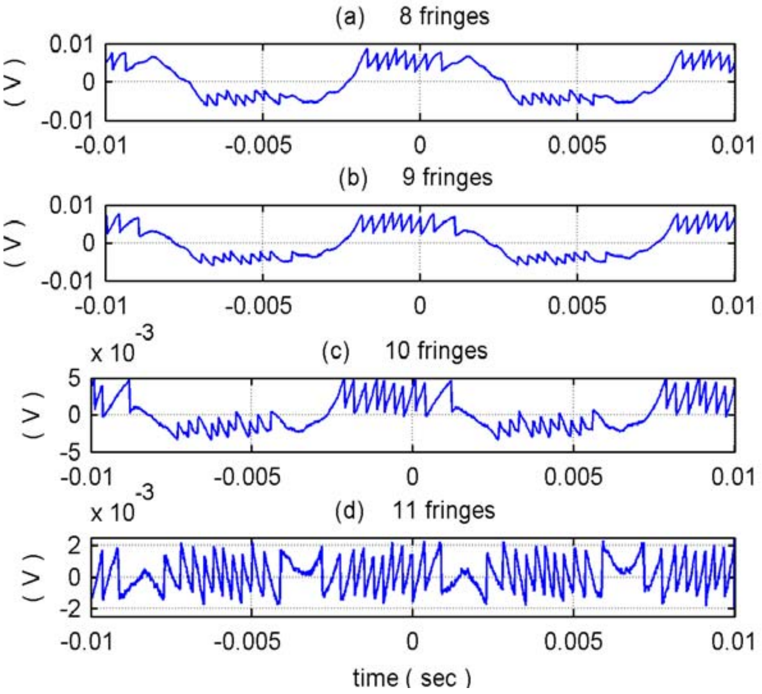

Fig. III:45 (a-d) Experimental OOP signals in the moderate feedback regime for a 785 nm FP LD with D_0=78 cm for varying focus.

Fig. III:46 presents three laser beam spots on the metallic surface of the PZT have been captured by a standard web-cam that is placed just outside the optical path. These three spots (a-c) correspond to the focusing that resulted in 9, 10, or 11 fringes respectively. Clearly, the more a laser beam is focused on the target, the more the chances of fringe-loss for a given sensor to target distance (which is 78cm in this case). By observing Fig. III:45(b) and Fig. III:46 (a), we see that a relatively better focused spot results in a moderate regime signal with large hysteresis as well as fringe-loss. On the other hand, as the liquid lens continues to defocus the beam, the feedback decreases and the SM signal regains the fringes and finally has no hysteresis (Fig. III:45.(d)).

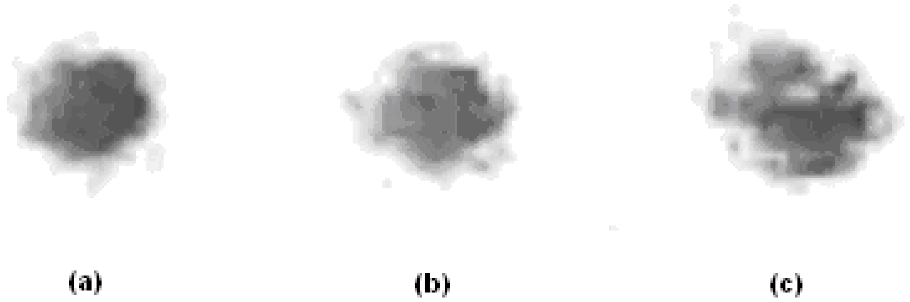

Fig. III:46 Laser beam spots on the metallic surface of the PZT that have been captured by a standard web-cam placed just outside the optical path.(a) 9 fringes, (b) 10 fringes, and (c) 11 fringes.

III.3.4 Influence on Metrological Measurements

This fringe-loss has a direct influence on the precision of the displacement or vibration measurement. For the fringe counting method (FCM), each lost fringe shall cause an error of λ/2. Likewise, even dedicated moderate regime displacement measurement methods such as the Phase Un-wrapping Method (PUM) cannot recover the lost information. Table III-3 presents the vibration measurement results for each of the SM signals shown in Fig. III:45. The error results of the vibration maxima have been found by comparison with the integrated capacitive sensor results.

No. of Fringes (N)	8	9	10	11
Error FCM (nm)	1110	718	325	68
Error PUM (nm)	180	116	48	32

Table III-3. Influence of fringe-loss on the error at the vibration maxima in reconstructed vibration signals as compared to a reference sensor for SM signals with D_0=78cm and S=4.25µm.

The impact of fringe-loss on the measurement error is easily seen. The use of the LL arrangement has thus successfully allowed us the control of the feedback level leaving a reliable moderate regime SM signal at a given fixed distance ((Fig. III:45.(d)).

Hence, SM metrological sensing should then be maintained in such practical conditions that result in C just greater than 1 ($1<C<\pi$). This would allow us to stay in the moderate feedback regime with its sawtooth-like fringes while avoiding a possible fringe-loss.

III.3.5 Variation in the Sensor-to-Target Distance

Another aspect in the moderate regime SM sensing is the influence of the variation of D_0 on C. We can see that for the same operating conditions, a decrease in D_0 reduces τ_D, thereby reducing the value of C. This means that a SM LD sensor set-up measuring a target vibration in the moderate regime may change to the weak feedback regime (with quasi-sinusoidal fringes implying directional ambiguity) if D_0 is reduced. Fig. III:47 (a) presents such a weak regime signal as compared to a moderate regime signal (Fig. III:47 (b)). Conversely, a large increase in D_0 while keeping all the other operating conditions the same will cause a large increase in C, thereby resulting in fringe-loss.

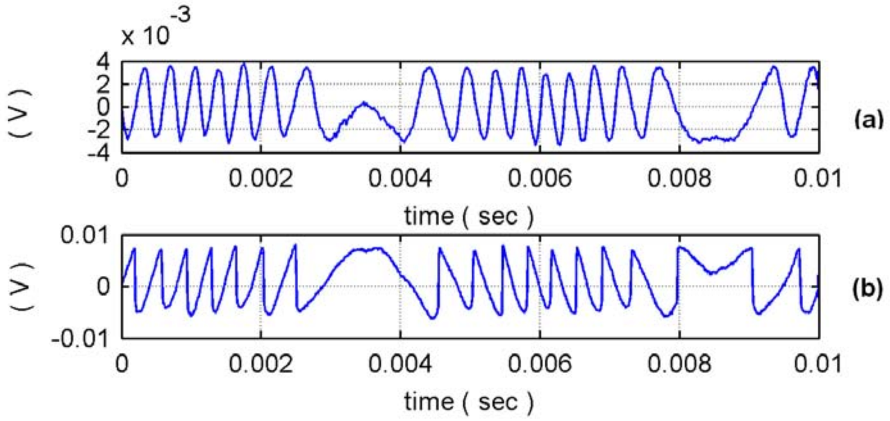

Fig. III:47 Experimental weak regime SM signal at D_0=5 cm (a) and a moderate regime SM signal at D_0=10 cm (b) for the same constant target vibration.

Further usefulness of the liquid lens based set-up is then shown by the fact that it allows us to maintain the SM phenomenon in a moderate regime with no fringe-loss even for a large variation in D_0. Fig. III:48 presents the OOP signals acquired for a D_0 varying from 6.5 cm to 265 cm. For a constant peak-to-peak target vibration of 3.6 µm, the number of SM fringes remains constant (N = 9).

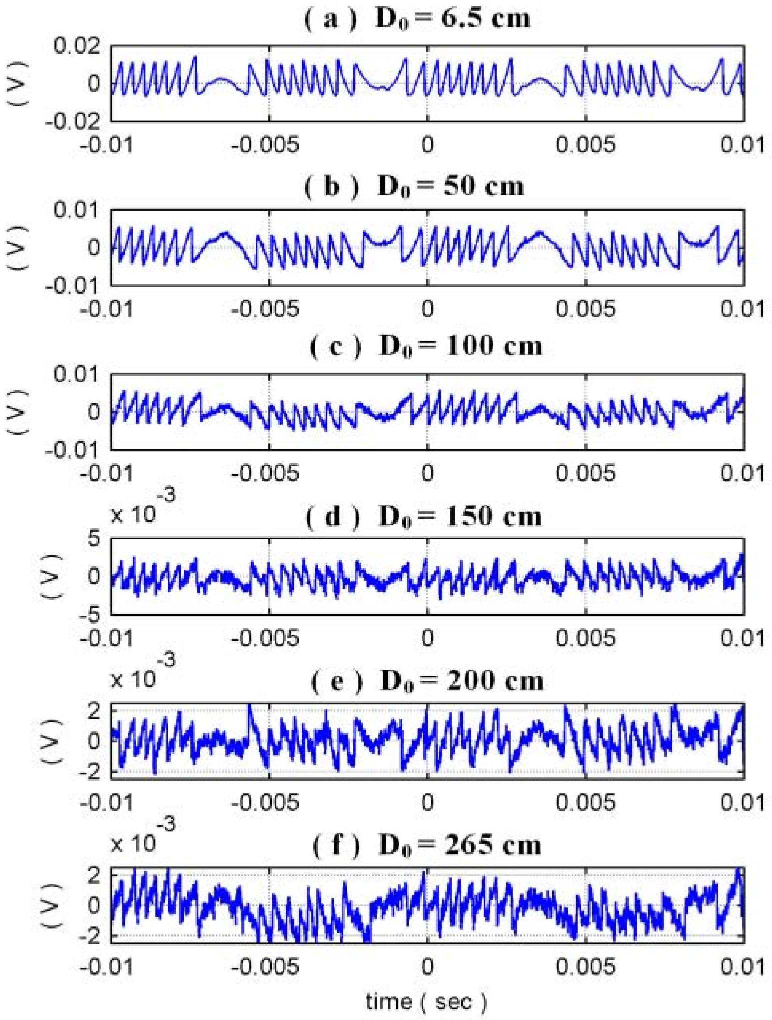

Fig. III:48 (a-f) Experimental OOP signals for a variation in D_0 from 6.5 cm to 265 cm for a constant target vibration of 3.6 µm.

III.3.6 Metrological Signal Reconstitutions

Based on these SM signals presented in Fig. III:48, vibration reconstitutions have again been done. The SM signal, the number of detected fringes and the reconstituted vibration signal as compared to the reference capacitive sensor signal are all shown for the case of D_0 = 6.5 cm as well as for D_0 = 265 cm in Fig. III:49.

The maximum error at the vibration signal maxima for each of these SM signals has been calculated and is presented in the Table III-4. The worst error over the whole of distance range (D_0 = 6.5 cm to D_0 = 265 cm) corresponds to about λ/16 for a 785nm LD.

Distance (cm)	6.5	50	100	150	200	265
Error PUM (nm)	44	23	20	45	32	36

Table III-4 Error at the maxima of the reconstituted vibration signals as compared to a reference sensor for a given distance D_0.

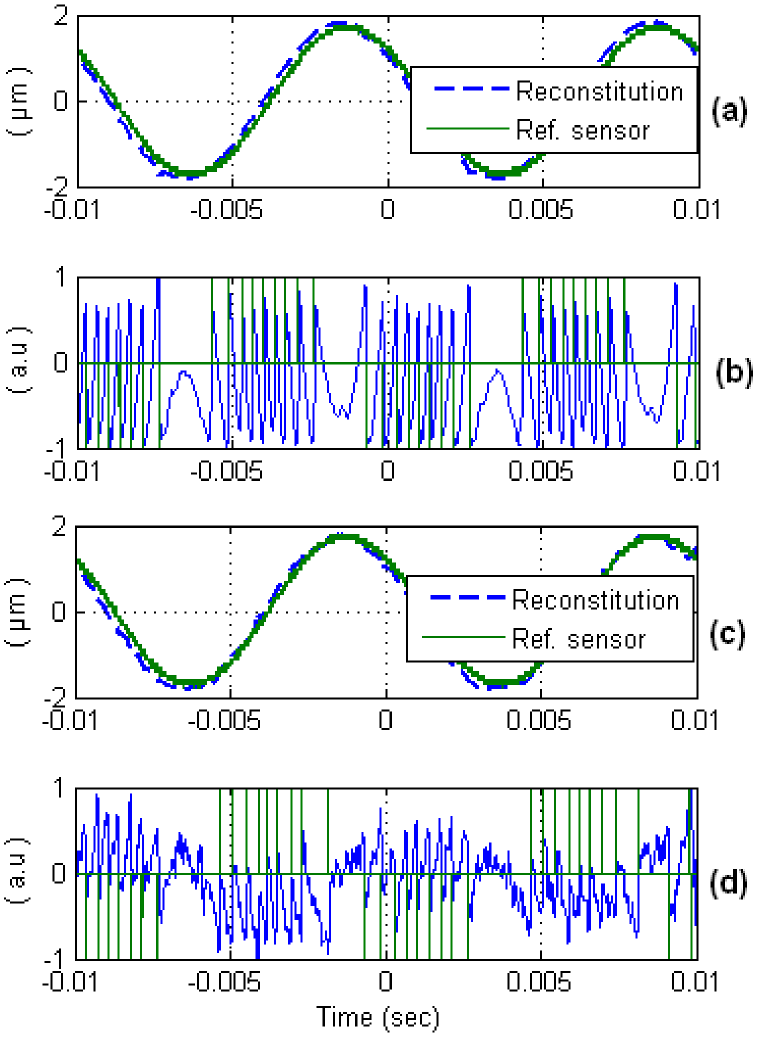

Fig. III:49 Vibration reconstitutions as compared to a reference sensor (a,c) for experimental OOP signals having 9 fringes at D_0=6.5 cm (b) and D_0=265 cm (d).

Furthermore, the presented set-up has also been used to measure triangular, square, and arbitrary target displacement signals with error at the maxima of 47 nm, 36 nm , and 161 nm respectively as compared with the reference sensor signal (as seen in Fig. III:50). These results successfully demonstrate the ability of the LL set-up to provide a fringe-loss free moderate regime SM signal irrespective of the target amplitude, shape or distance.

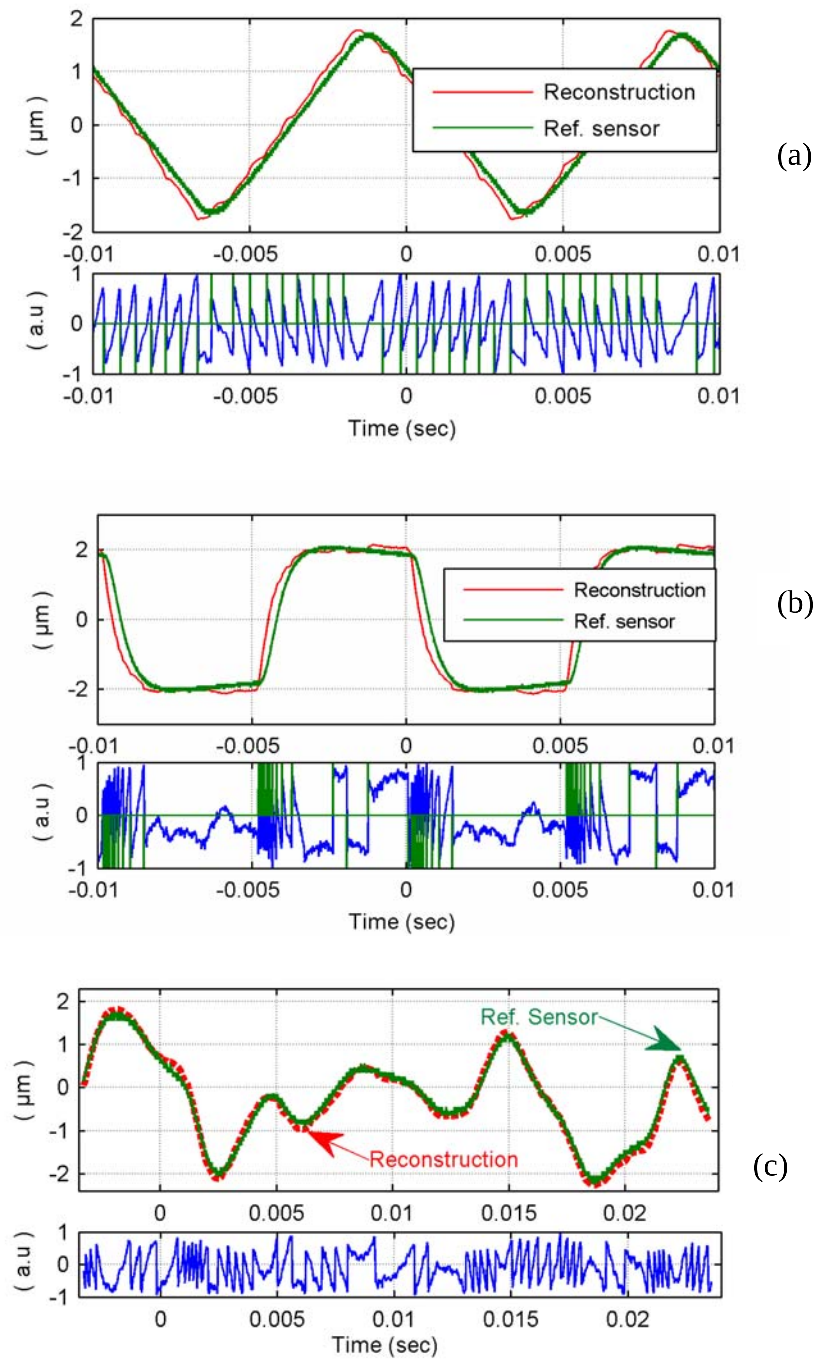

Fig. III:50 Displacement reconstitutions for (a) triangular,(b) square, and (c) arbitrary target movement as compared to a reference sensor.

III.3.7 Liquid Lens Control

In order to make the LL control autonomous, we need to distinguish the moderate regime from the weak regime. So, the automatic fringe detection algorithm [87] can be used as it is capable of such a distinction between different feedback regimes. Although this algorithm can successfully treat the weak regime signals, it requires additional signal processing due to quasi-sinusoidal shape of the fringes, which was avoided by using the LL. Thus, the LL maintains the SM in the moderate feedback regime where a simple fringe detection can be used to lighten the displacement reconstitution process.

III.3.8 Assessment of the Use of Adaptive Optics

In this section, we have demonstrated the use of adaptive optics in the form of a voltage controlled liquid lens for maintaining the Self-mixing phenomenon in the moderate feedback regime over a large range of the distance between the laser and the vibrating target. The vibration measurements based on these signals as compared to a commercial sensor validate the usefulness of adaptive optics for self-mixing applications. The future implementation of an automated liquid lens based set-up shall result in a precise and autonomous self-mixing metrological sensor, able to measure with precision over a large sensor-to-target distance range.

III.4 Conclusion

The studies undertaken in the last chapter for the optimisation of the phase unwrapping method showed that a new approach to displacement reconstruction is needed if we wish to have a real-time natured displacement sensor. Furthermore, its static fringe transition detection approach needs to be changed so that the sensor can simultaneously work for the weak and moderate optical feedback regimes.

Thus, in this chapter, a new signal processing technique for displacement measurement has been presented that is of a real-time nature as it does not need time-consuming joint optimisation step needed in the phase unwrapping method. Furthermore, it has an added advantage that it is able to detect and correct the phenomenon of fringe-loss that happens in case of an increase in optical feedback into the active cavity of the laser diode.

Then, another signal processing technique has been presented that is able to correctly detect the fringe transitions of the SM signals of the weak as well as moderate feedback regime. The target displacement results for the various weak and moderate feedback regime signals coming from different lasers and media have been presented. Such a technique then makes it possible to correctly recover the displacement information using a same algorithm even if the feedback regime changes from one to another.

Finally, the use of adaptive optics in the shape of a liquid lens has been demonstrated for SM displacement applications. It has been shown that not only it increases the range of the measurement but also helps in maintaining the SM signal in a certain feedback regime. So, the use of liquid lens can then simplify the signal processing needed for the sensor. However, it needs to be stated that the variations in the change in focalisation for the present liquid lens are slow which may reduce the use of such a device for rapidly varying displacements. Likewise, its utilisation would add another optical component to the set-up that can increase the overall cost and complexity of the sensor. Nonetheless, the cost of such a device cannot be very high due to its high volume production for the cameras. Furthermore, there remains a possibility of its integration directly onto the laser chip, a task which is the subject of a thesis in a sister laboratory.

In short, this present chapter has highlighted the various solutions needed to counter the effects of varying optical feedback so that a reliable and adaptive displacement measurement can be obtained. The first two sections of this chapter presented the algorithmic solutions to such a variation in the feedback whereas the third section has detailed the use of an adaptive optical element that allows us to electronically control the optical feedback into the laser cavity such that a reliable SM signal is always obtained.

The next chapter is based on the work done to have a SM displacement sensor that is more robust to practical conditions of utilisation. Thus, the use of such a sensor in the presence of speckle, misalignment as well as parasitic vibrations has been presented. Likewise, the efforts begun to implement the sensor processing techniques into an FPGA shall be presented.

IV Towards an Industrial Sensor

The field of Self Mixing Interferometry continues to be a rich source of scientific activity and publication. The potential of this phenomenon for its use in a metrological device has already been presented in the preceding chapters. What, however, needs to be emphasized is that for a considerable number of cases where the SM effect is used for sensing applications, the published results are obtained under laboratory conditions (e.g. by using cooperative target surfaces, optical tables, precision mounting and alignment stages). However, if one is to realize the promise of the practical application of such sensors under industrial conditions then the robustness of the sensor with respect to industrial usage conditions has to be reworked.

Thus, this chapter presents the work undertaken to make our displacement measuring SM sensor more robust in case of non-cooperative target surface and a misalignment between the laser and target (that would accentuate the speckle effect) as well as in case of presence of parasitic mechanical vibrations to the sensor assembly that may be caused by an unwanted mechanical coupling between the sensor assembly and the target or by stray, ambient vibrations (that would falsify the measurement of the perturbed sensor).

So, in order to observe the behavior of the SM displacement sensor under the above-mentioned conditions, experiments have been conducted where misalignment, non-cooperative target surface and parasite mechanical vibration to the sensor have been deliberately applied.

The later sections of this chapter present the efforts done to pave the way for a future real-time sensor on chip. As a first step, the trigonometric function blocks needed in the calculations have been optimised so that these could be later implemented in a FPGA based prototype.

Let us, however, start by looking into the data processing used for countering the speckle effect that becomes all the more important in case of centimetric displacement measurement.

IV.1 Centimetric Displacement Sensing

Although the SM effect has typically been used to measure the micrometric displacement of the target but the same principle can be extended to measure displacements of the order of several centimeters or even decimeters. In order to measure such large displacements, the basic displacement resolution of lambda/2 per SM fringe can then be used.

A study of the reported results of such large displacements, however, indicates that special optical/electronic equipment, target surface treatment as well as signal processing has been added to the standard simple LD based SM displacement sensor (as detailed in the next sub-section). The main issue that makes such additional components or processing inevitable is the Speckle effect that deforms or even eliminates the SM fringes. Let us first look in to this phenomenon.

IV.1.1 The Speckle Effect

Although sensors using the principle of self-mixing offer many advantages, as we have said previously, the results can be affected by a parasitic noise: the phenomenon of speckle or granularity due to the surface of the target. This speckle appears in the form of alternately dark and bright spots that are spread randomly in space. Thus, as seen in Fig. IV:1 for a diffusing surface, the back-scattered beam shows a characteristic random texture.

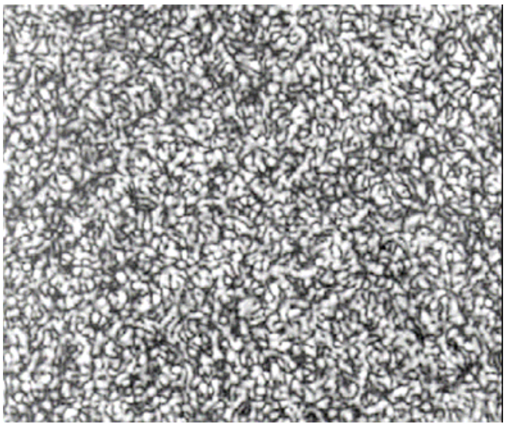

Fig. IV:1 The randomly spotted texture due to the Speckle effect.

When a target is illuminated by a laser beam, a fraction of the power that is neither transmitted nor absorbed by the target is reflected in space. This reflection for the case of the more common materials, is due to a combination of two phenomena that have been studied extensively namely:

- Specular reflection, which corresponds to the reflection of a mirror, which generates a beam of high directivity.

- Lambertian or diffusing reflection, where the light energy is uniformly distributed in space (e.g. for a plaster surface). See Fig. IV:2.

So, the spatial-coherence destruction of the beam is caused by the interaction of the beam with the diffusive surface [98]- [99] at two levels.

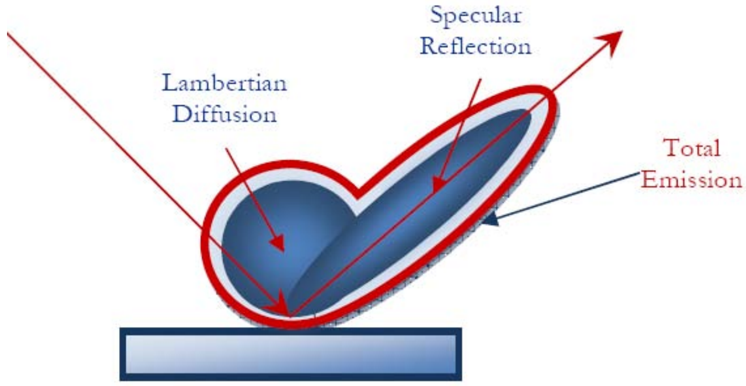

Fig. IV:2 Emission diagram of a regular surface.

As a first approximation, a rough surface illuminated by a laser beam (coherent light) can be regarded as an infinite set of points emitting coherent light [100]. Due to the phenomenon of interference, the light intensity at any point in space depends on the optical path difference between the beams emanating from the emitting points of the illuminated surface. That is the reason behind the fact that the speckle appears all the more important as the roughness of the surface approaches the wavelength of the light beam. Thus, there appears in space, a juxtaposition of small dark spots whose transmission coefficient is zero, and of small bright spots whose transmission coefficient is close to unity, as shown in Fig. IV:1.

The presence of the speckle spots distributed over the area where the laser beam falls thus represents a noise and it perturbs the operation of the laser. This spot scrolling results in a strong amplitude modulation or fading of the self-mixing signal (Fig. IV:3) and can even result in a total loss of the signal. So, in the case of a displacement measurement, if the signal disappears even for a moment, the fringe counting becomes false. The measurement can thus no longer be valid as it is only relative, as compared to the original position. However, the period during which the signal is zero is very small. Therefore, even though the optical power signal can be significantly distorted by the presence of speckle spots, it is still possible to exploit this signal to estimate the speed of the target [100].

In the case of sensors that use the self-mixing phenomenon in order to estimate the position of a moving target or a target displacement along the laser beam axis, the speckle phenomenon has proved to be a major challenge. The sensor is indeed positioned so that the laser beam axis is perpendicular to the target surface and the displacement measurement is taken along the laser beam axis if there is a displacement of the target relative to the sensor. The speckle noise is then very annoying because the oblong form of the speckle spots means that if a dark spot is located in front of the laser diode, then it will remain there and prevent the measurement to be taken. In order to obtain a valid measurement, it will then be necessary to move the sensor laterally. In the case of a longitudinal displacement sensor, if a dark spot is present in front of the laser diode opening during displacement, then there are two possibilities: either the displacement is less than the length of the speckle spot or it is greater than the length of the speckle spot. However, in both situations, the result is the same: the displacement measurement can be unreliable as a result of possible fringe count loss. To overcome this problem in the case of a non-prepared target (i.e. a target with a rough surface), one solution is to mechanically lock the sensor on to a bright spot of light by using a piezoelectric transducer [101]. In case of unavailability of a mechanical tracking, another solution lies in the envelope tracing of the modulated optical power signal that shall be detailed in the following section.

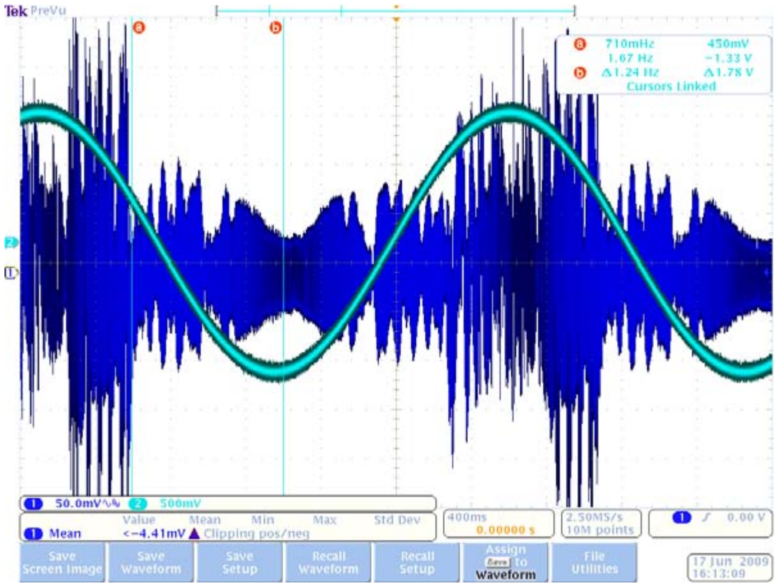

Fig. IV:3 OOP signal fading caused by the speckle effect for a harmonically moving metallic target.

IV.1.2 SM Centimetric Displacement Sensing Results

Let’s look into some of the solutions proposed by various authors for a correct measurement of centimetric displacements.

The linear and transverse displacement measuring sensor system proposed by Ottonelli et al is capable of measuring linear displacements of up to 40 cm [102] . Although the SM sensor is only based on a LD and a collimating lens, the target chosen, however, is a plane mirror that allows a stable moderate regime signal without any speckle. Such a choice, does limit the utilization of the sensor for practical cases where the target surface cannot be reworked. The choice of the target surface is then very important as in an other publication by the same group [33], the use of retro-reflective prisms instead of the plane mirror allows them to improve the range of yaw and pitch measurements by one order of magnitude.

Another approach for measuring centimetric displacement has been presented by Giuliani et al [27]. It consists in keeping the operating point of the SM interferometer fixed at the half-fringe value. Therefore, the resultant SM sensor avoids the speckle effect as well as the fringe loss thus by-passing sophisticated signal processing. However, this approach does need an objective lens that collimates the LD beam onto a second focusing lens placed at a distance of 40cm in order to project the LD beam spot on the target. Furthermore, for non-cooperative surfaces, an optical attenuator has to be inserted in the optical path to prevent the optical feedback from becoming excessive. Another condition is that the absolute distance to the target has to be measured at the beginning of each measuring session. Finally, the depth of field of the instrument, i.e. the longitudinal displacement of the target around the optimal working distance that causes a factor of two reduction in the dynamic range, is ±8 cm.

Another speckle countering technique has been proposed by Norgia et al that avoids the use of mirrors or reflective paints to achieve a cooperative target [47]. In order to correctly detect the speckle affected SM fringes with a poor SNR, a technique has been developed that is insensitive to changes in the back-injection amplitude or regimes as it works by calculating the frequency of the local most power tone, called the ‘beat frequency’. The main feature of this method is an intrinsic average process in computing the fringe duration so that single spikes or signal losses do not significantly affect the measurement. The paper, however, presents correct displacement recovery signal of only tens of micrometers.

In an other technique published by Norgia et al, a speckle tracking technique has been developed that has allowed experimental displacement reconstruction of up to 50cm [101]. In order to counter the speckle effect, the speckle relative maximum amplitude is used to jump from one bright speckle spot to another. The technique uses two piezo-actuators to move a lens in the transversal plane to the laser beam. The laser spot is thus moved on the diffusive target surface and the OOP from the Photodiode is used to form a closed loop with the piezo-actuators such that the recovered SM signal attains a certain amplitude level. The error results have not been quantified for those SM fringes that may get lost as the lens is moved from one bright spot to another.

Likewise, an improved version of the above-mentioned sensor has also been published by the same research group where a Liquid Crystal Attenuator has been added to the system and it forms another feedback loop with the Photodiode signal [103]. This results in a better countering of an excessive optical feedback such that the SM signal stays in the moderate feedback regime and avoids strong feedback regime causing complete fading of fringes. In addition, for the digital processing of the SM signal, an adaptive fringe threshold detection has been developed which uses a triangular laser current modulation. Frequency and amplitude of the triangular wave are, however, a function of the maximum target speed (set to 6 cm/s for the prototype). In this way, the presence of at least one positive and one negative pulse per period is ensured.

IV.1.3 Centimetric SM Signal Acquisition

In order to acquire SM signals for centimetric displacement, a camera-mounted device (as seen in Fig. IV:4) was used that is capable of displacing the camera in XY axes. It can then generate displacements of up to 1 m in the X-axis and up to 50 cm in the Y-axis, each with a 50µm precision. The SM sensor was installed on the same mechanical assembly that contains the rails on which the camera is installed. The laser then pointed along the X-axis on the vertical metallic bar that holds the camera. Thus, the target surface was an unpolished metal surface. As a matter of fact, this installation of the sensor on the same mechanical assembly was a voluntary choice with an aim to see the possible influence of a parasitic mechanical coupling between the moving target and the sensor assembly. Likewise, no extra efforts were made to have an exactly parallel laser beam along the X-axis. This caused a sort of scanning of the target surface by the laser spot as the misalignment caused the laser spot to slide on the target surface as the target moved.

The aim of these “inattentions”, as already indicated in the chapter introduction, has been to fairly resemble the realistic industrial conditions where the SM optical sensor cannot be guaranteed a perfect alignment or complete absence of undesirable mechanical coupling.

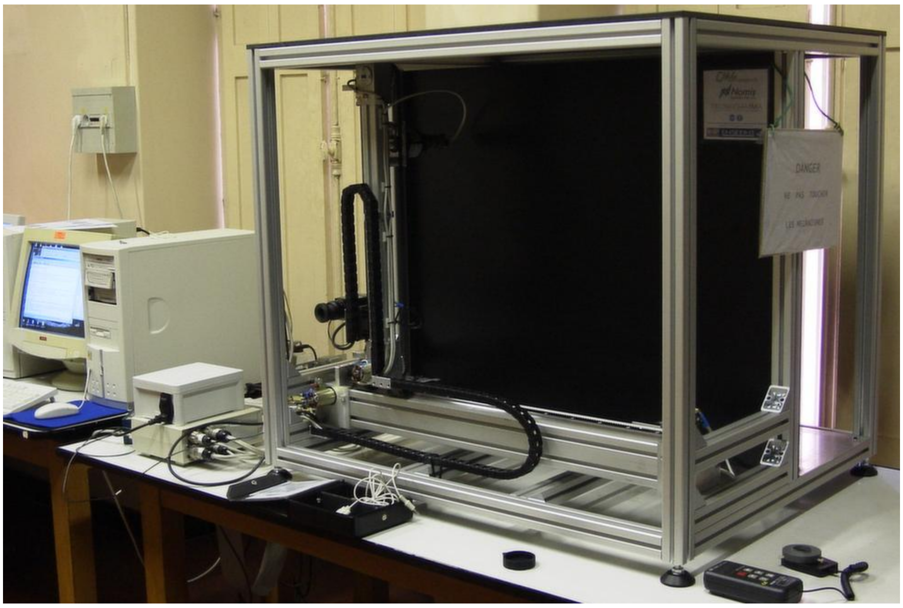

Fig. IV:4 A photograph of the device used for the measurement of centrimetric displacements using the SM displacement senor.

IV.1.3.a Influence of Mechanical Coupling

Fig. IV:5 presents a segment of the SM signal obtained for a 1cm long displacement along the X-axis such that the sensor to target distance was 55cm. It is clear to see that the sensor SM signal has been affected by the parasitic coupling that explains the fluctuations in the SM signal.

Such fluctuations in the SM signal thus make it difficult to use zero-crossing technique for fringe detection. Likewise, the adaptive fringe detection algorithm also faces problems as the moderate SM signal cannot be divided into two distinct regions i.e. P<0 and P>0, where P is the normalized SM optical output power.

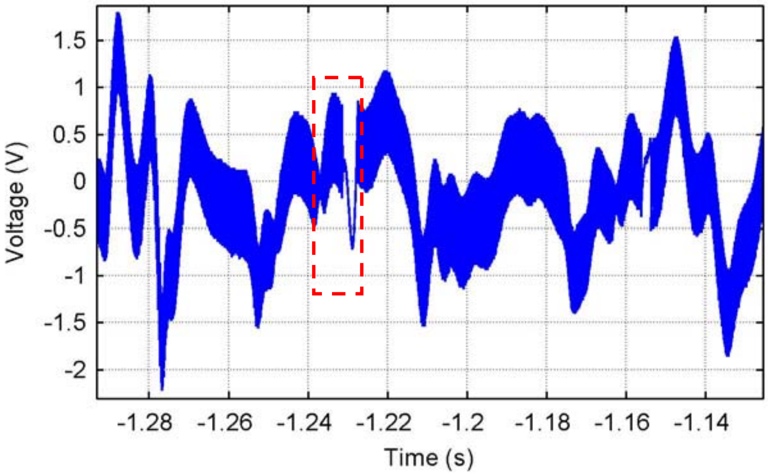

Fig. IV:5 A segment of a SM signal obtained for a centimetric target displacement. The fluctuations in amplitude are due to non-stationary SM sensor. The area within the segmented-lined block is Speckle-affected and is reproduced in the next section.

IV.1.3.b Influence of Target Surface Scanning

A further zoom in to the segmented-lined block of Fig. IV:5 is presented in Fig. IV:6. This image indicates the presence of speckle that has affected the amplitude of the SM fringes. The obvious impact of such a reduction in fringe amplitude is the impossibility of using a constant fringe-detection threshold. Thus, the threshold value needs to be adapted to the presence of speckle.

The presence of an arbitrarily occurring speckle is all the more trouble-some as the amplitude of a normally stable SM segment can rapidly vary if a dark speckle spot comes in to field of the laser beam spot. As the lack of misalignment results in a “scanning” of the moving target surface, so in case of diffusive surfaces, such speckle related signal black-outs become a frequent occurrence and regularly deform the SM signal.

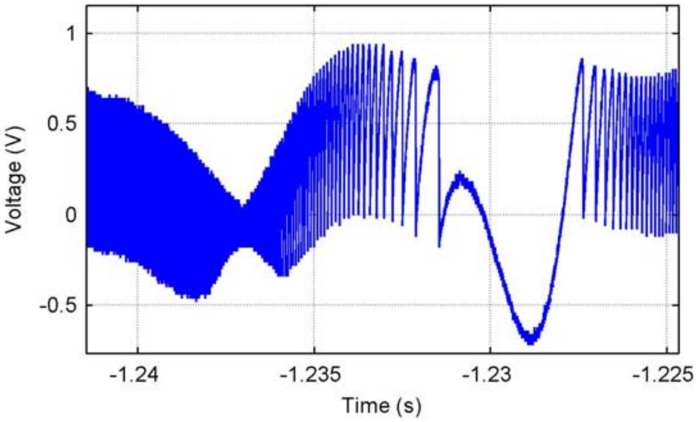

Fig. IV:6 A segment of a SM signal obtained for a centimetric target displacement. The decrease in the amplitude is due to the speckle effect.

In Fig. IV:7, the influence of the scanning of the target surface is presented. As the target is moving in a sinusoidal manner, so the scanning of the metallic surface causes an amplitude modulation of the SM signal, explained by the speckle effect.

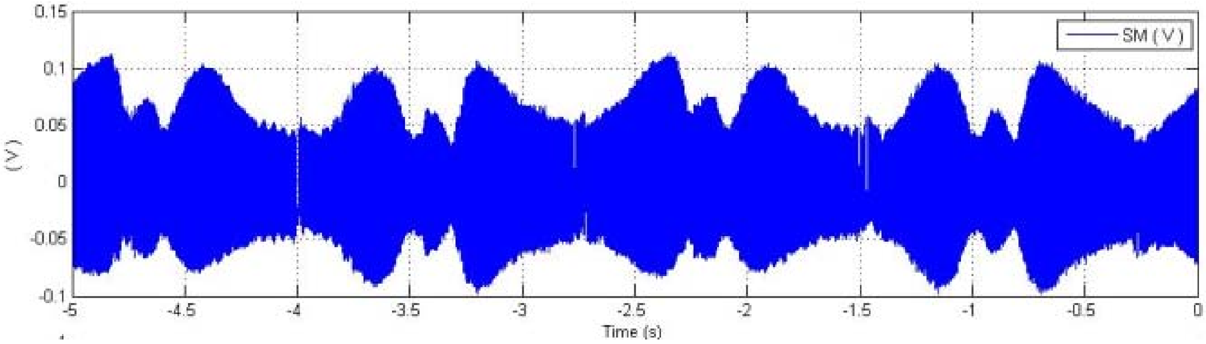

Fig. IV:7 The SM signal obtained for a sinusoidally moving metallic surface target. The misalignment results in a scanning of the surface and subsequent SM signal amplitude modulation.

Thus, in order to correctly reconstruct the displacement from the SM signal, we have to adapt our signal processing technique so that the issues of the fluctuations as well as the speckle can be resolved.

IV.1.4 SM Signal Treatment

IV.1.4.a SM Signal Envelope Extraction

The SM signal treatment starts by following the steps already detailed in Fig. III:20 to achieve the derivative signal. Then, instead of converging to the correct threshold value as in the adaptive fringe detection technique, the new processing searches the local maxima and minima of the derivative signal. In such a way, the upper and lower envelopes (i.e. the max. and min. envelopes) of the derivative signal are obtained. Fig. IV:8 presents the derivative signal as well as the min. and max. envelopes for the speckle affected SM signal of Fig. IV:6. Thus, we are able to closely follow even the speckle-affected signal. Note that Fig. IV:8 is based on a SM signal that represents only a forward target movement. So, no variations are to be seen for the min. envelope. Note also the presence of a fringe-less zone where the target movement remains less than the half-wavelength. The min. and max. envelopes of this zone then represent the SM signal noise floor.

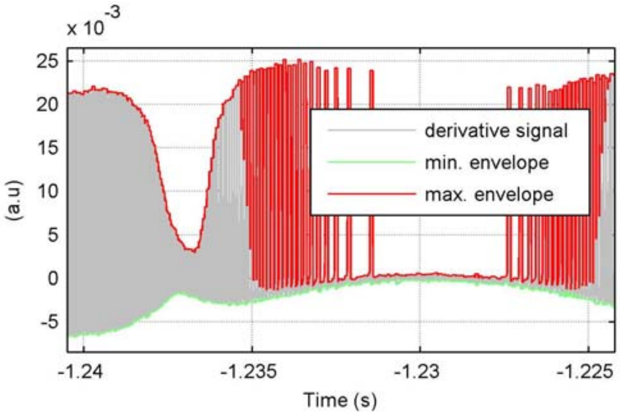

Fig. IV:8 The extraction of the max. and min. envelope of the derivative of the SM signal by searching for local maxima and minima.

IV.1.4.b Fringe-less Segment Distinction

A cut-off limit has then to be imposed so that all those samples of the derivative signal which are lower than this limit cannot be considered for fringe-detection. Fig. IV:9 presents the cut-off value used to separate the fringe containing segments from the fringe-free segments. The value is chosen to represent the SM signal noise floor. The previously detected local maxima are then saved into a decider array. Subsequently, all values of this array greater than the cut-off limit can be considered for fringe-detection.

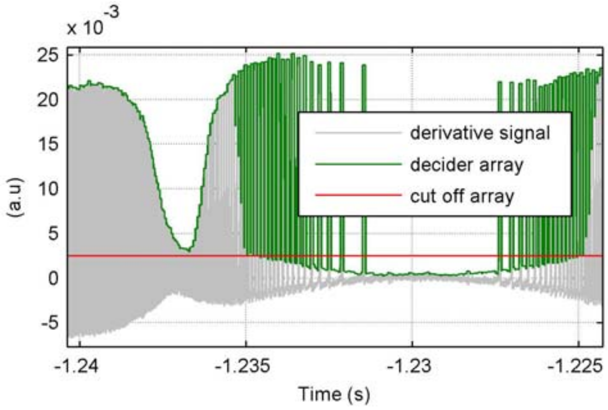

Fig. IV:9 The cut-off array contains the noise floor value used to separate the fringe containing segments from the fringe-free segments. The decider array contains the local maxima values.

IV.1.4.c SM Fringe Detection

A fixed threshold value of 90% is then used to detect the fringes. Thus, all those values of the derivative signal at 90% of decider array are considered as representing SM fringes. Such a high threshold is necessary as the local maxima values closely follow the SM fringe peaks, so a smaller threshold can introduce faulty fringe detection.

The resultant correct SM fringe detection for the speckle-affected OOP segment is then presented in Fig. IV:10. The introduction of the cut-off value allowed to distinguish the fringe-less segments where as the local mixima tracking resulted in completely recovering the SM fringe locations for the speckle-modulated segments.

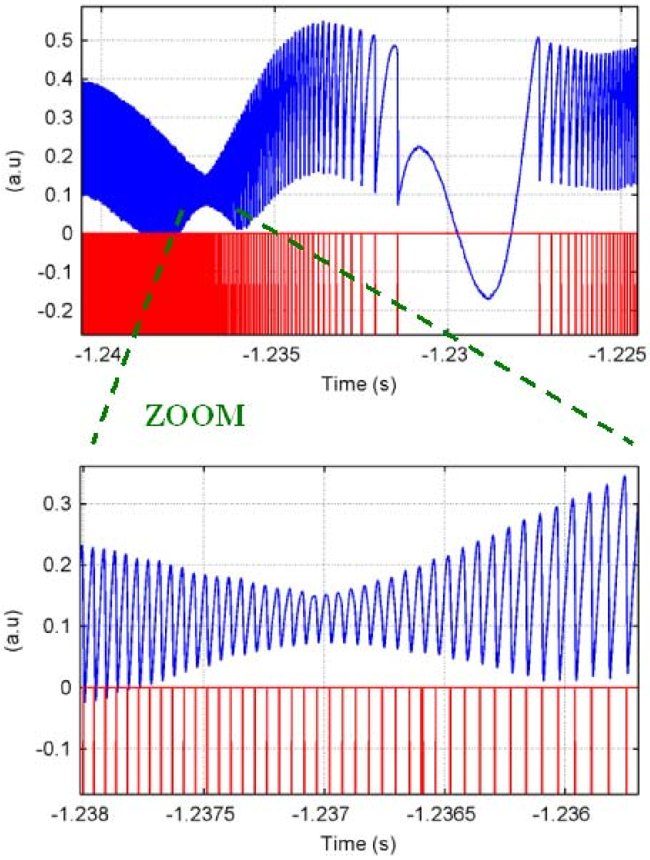

Fig. IV:10 Correct SM fringe detection for the speckle affected OOP signal. Note that no faulty detection occurs for the fringe-free segment.

IV.1.5 Experimental Result

Fig. IV:11 (a) presents an experimental SM signal acquisition for a target displacement of 2.5cm. The SM sensor was installed on the mechanical structure that contained the moving rail. The target surface was metallic and the initial sensor to target distance was 63 cm.

Using the signal treatment outlined above, the reconstructed displacement is shown in Fig. IV:11 (b) while a zoom at the end of the signal shows the total displacement of the target in Fig. IV:11 (c). The final displacement at standstill of 2.5036 cm is within the expected range of [25050µm 24950µm] if we take into account the 50µm accuracy of the displacement device. The result thus represents a percentage error of 0.14%.

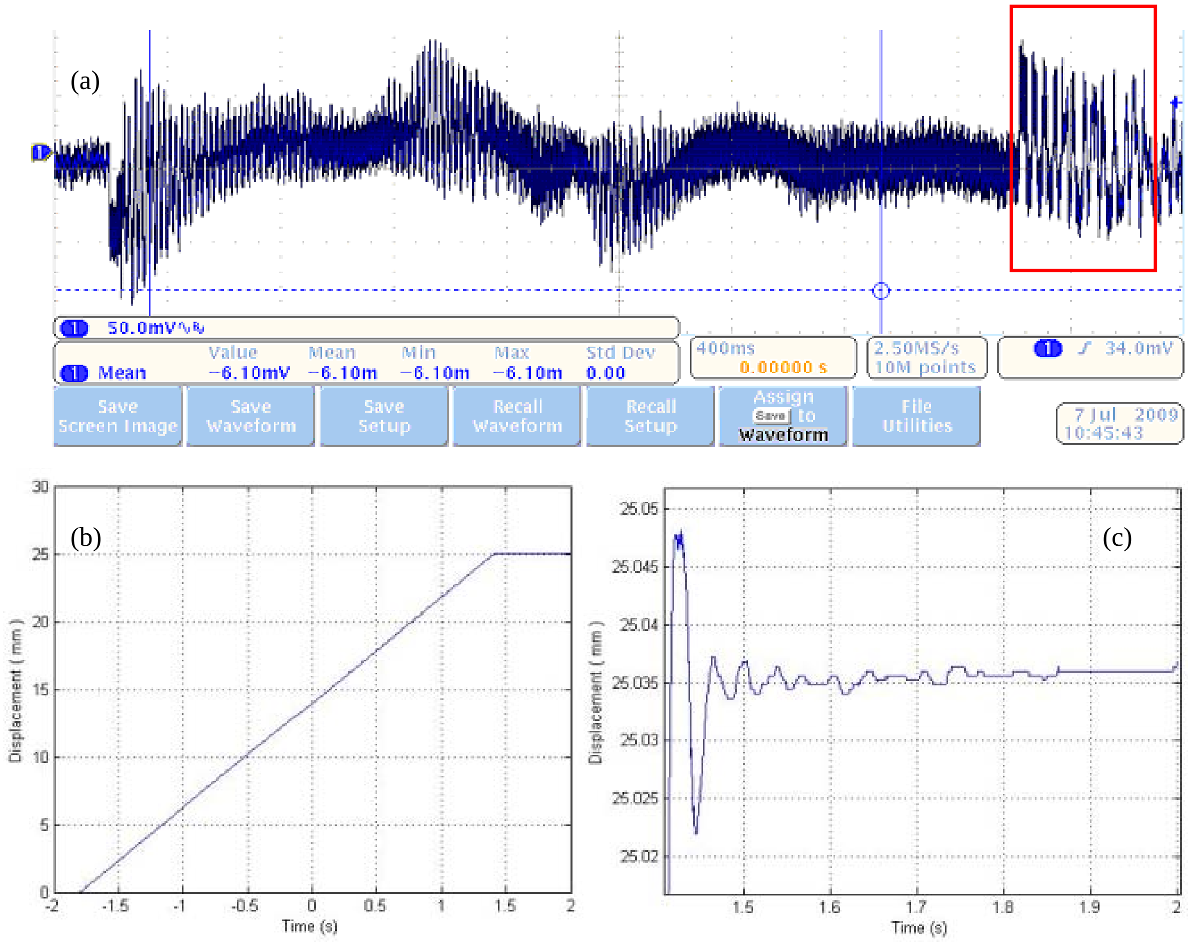

Fig. IV:11 (a) The SM signal obtained for a linear target displacement of 2.5cm for a metallic surface at the initial sensor to target distance of 63cm. (b) The reconstructed displacement after using the signal treatment. (c) Zoom at the end as the target settles to stand-still.

IV.2 Parasitic Vibration Correcting Sensor

It is important to underline that SM displacement sensing systems suppose a stationary sensor to guarantee an accurate measurement of target movement. Thus, these set-ups use an optical table to completely isolate the sensor from parasitic vibrations that would falsify the displacement measurements. So, in order to ensure good measurement precision, a great cost and effort is traditionally undertaken, which is not only difficult to ensure under realistic industrial conditions but also goes against the philosophy of low-cost sensors. Nevertheless, solid-state accelerometers (SSA_{cc}) can be used to sense these parasitic vibrations applied to the SM sensor. Such sensors benefit from a small size as well as a low-cost due to the high volume requirement for automotive, robotics and gaming applications.

This section thus presents a solution based on a SSA_{cc} coupled to the SM sensor to counter the parasitic movements to the sensor, thus liberating the optical sensor from optical tables or any other equivalent mechanical support. It then becomes imaginable to install the sensor even on non-stationary surfaces and embedded systems, thus opening its utilization in industrial conditions.

IV.2.1 Experimental Set-up

The schematic diagram of SM test bench is shown in Fig. IV:12.

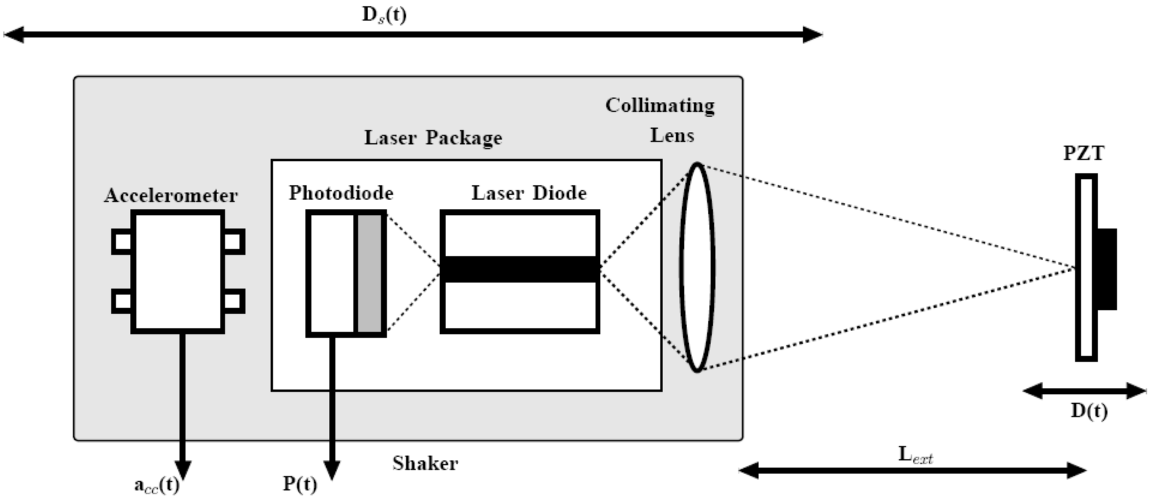

Fig. IV:12 Schematic diagram of the SM displacement measuring sensor coupled with a sold state accelerometer.

Here, a piezoelectric transducer (PZT) from Physik Instrumente (P753.2CD), equipped with a capacitive feedback sensor for direct-motion metrology with a resolution of 2 nm is used as a target. The parasitic vibrations are generated by a shaker to which the LD, combined with a SSA_{cc}, is attached. The built-in photodiode of the LD package is used to retrieve the SM signal caused by both the target displacement $D_{PZT}(t)$ and the shaker displacement $D_s(t)$, such that the global displacement D_Σ is defined as:

$$D_\Sigma(t)=D_{PZT}(t)+D_s(t)=N\lambda/2+\varepsilon \tag{4-1}$$

where N is the number of fringes of the SM signal and ε is the excess fringe 'ε' ($< \lambda_0/2$). Here, $D_s(t)$ is monitored indirectly through the measurement of the LD acceleration by a solid state accelerometer.

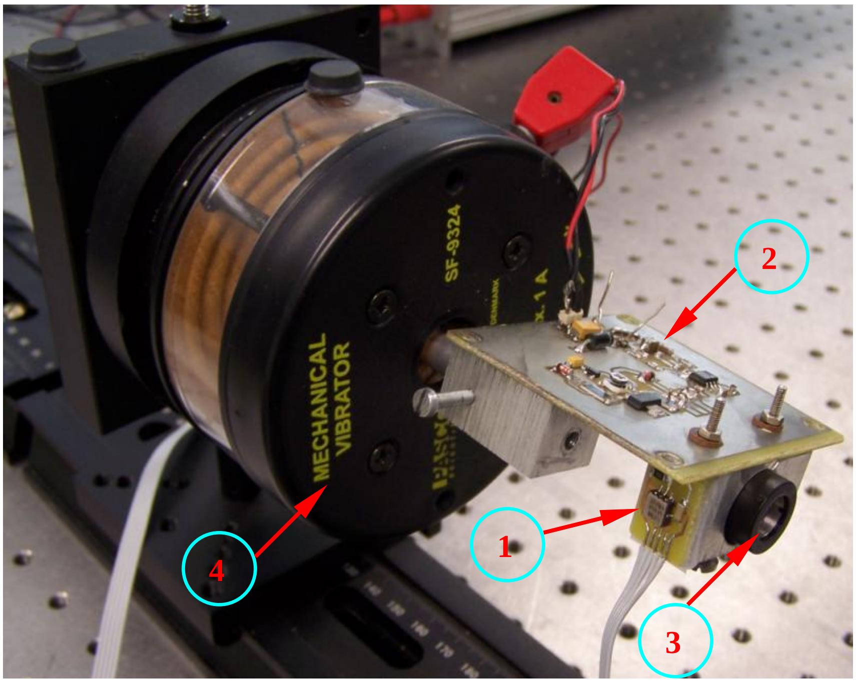

Fig. IV:13 A photograph of the accelerometer coupled SM sensor. The accelerometer(1) has been glued to the heat sink used for the Laser Diode. The sensor card (2) has been mounted on a mechanical shaker (4) such that the collimating lens(3) directs the beam towards the target.

IV.2.2 Displacement retrieval from the accelerometer

The proposed method consists in first reconstructing the displacement D_s due to the parasitic vibration by filtering and integrating twice the acceleration signal a_{cc} from the accelerometer sensor as follows:

$$D_s(t) = \int_0^t \int_0^u a_{cc}(v)\,dv\,du + D_s(0) \qquad (4\text{-}2)$$

where *dv* and *du* are the variables of integration.

From eq. (4-2), the white noise power density of the accelerometer signal S_{acc} has a $1/f^4$ frequency dependence and the noise power density of the computed displacement S_{Ds} can be expressed in the frequency domain as:

$$S_{Ds}(s) = S_{acc}(s)/s^4 \qquad (4\text{-}3)$$

Consequently, the displacement resolution is completely defined by the low cut-off frequency of the system. To avoid low frequency drifts that can make analog circuits to saturate, the accelerometer signal is thus bandpass filtered 20Hz-500Hz (as seen in Fig. IV:14). The high frequency limit is due to our shaker performances as well as our accelerometer dynamic range.

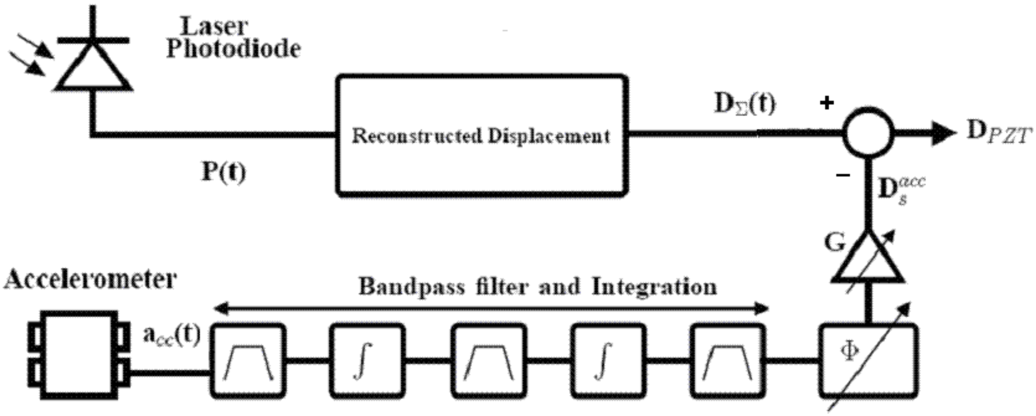

Fig. IV:14 Schematic block diagram of the vibration compensation method.

IV.2.3 Accelerometer Signal Phase and Gain Correction

To faithfully reconstruct D_s, the phase and gain of D_s should be corrected to take into account the phase and gain shifts induced by the analog circuit filters as well as the accelerometer gain (see Fig. IV:14). In fact, for a displacement amplitude A at a given frequency, assuming that the phase error ΔΦ and gain error ΔA are not correlated, the maximal residual error ξ_{max} can be given as:

$$\xi_{max} \approx \frac{A\sqrt{2}}{2}\sqrt{\Delta\Phi^2 + \Delta A^2 / A^2} \qquad (4\text{-}4)$$

Finally, once the phase and gain correction is done, D_{PZT} can be computed by subtracting D_s from the D_Σ global displacement (eq. (4-2)) sensed by the PUM [39]. A conceptual block diagram of the proposed method is shown in Fig. IV:14. It is to be highlighted that for the purpose of validation of the accelerometer based technique, the optical feedback into the laser cavity was always controlled (by the use of the lens) such that the feedback parameter stayed in the ($1<C<\pi$) range. As it was detailed in the preceding chapter, the resultant SM signal for such a C value is the easiest to process and is not affected by fringe-loss. For such a SM signal, PUM as well as SBM have equivalent precision but the PUM was preferred as in addition to the displacement measurement, it also gives a good estimation of the C parameter.

IV.2.4 Experimental Validation

During the experiments, the PZT target is positioned at L_{ext} = 45cm from the Laser along with the accelerometer (Fig. IV:12). The LD, driven by a constant injection current of 30mA and a maximum output power of 50 mW, is a Hitachi HL7851G emitting at λ=785nm. The accelerometer is the

ADXL311 from Analog Devices with a typical resolution of $300\,\mu g/\sqrt{Hz}$ and a 5kHz bandwidth.

First, the calibration of the accelerometer sensor was performed to retrieve the phase and gain correction coefficients using the test bench shown in Fig. IV:12. During the calibration, only the shaker is vibrating while the PZT is at rest. Four sets of measurements have been done from 20Hz up to 400Hz by step of 40Hz. Then, the data extracted from the accelerometer sensor and the SM signal is compared to obtain the phase and gain calibration coefficients that are stored in a look-up table. After calibration, the measured $\sigma\Delta\Phi$ is equal to 0.03 rad and $\sigma\Delta A/A=2\%$.

To validate the robustness of our system, the following tests are used:

- The Shaker and PZT are vibrating at two different frequencies.
- The Shaker and PZT are vibrating at the same frequency.
- The Shaker is vibrating at a single-tone frequency while the PZT is vibrating with an arbitrary signal.
- Two different arbitrary signals are applied.

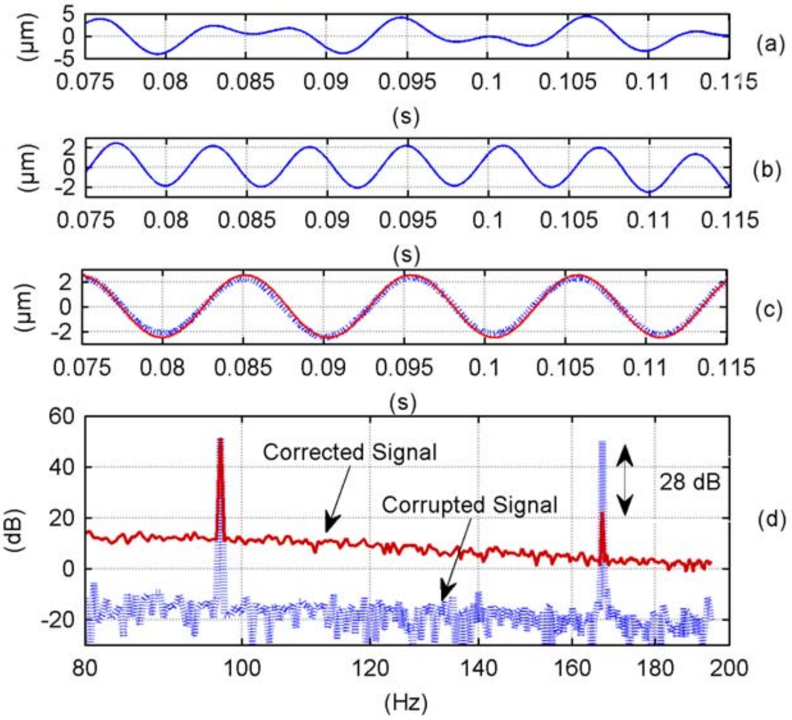

Fig. IV:15 (a) Corrupted displacement signal for f_{shaker}=81Hz and f_{PZT}=81Hz (b) Accelerometer signal (c) Reference signal at f_{PZT}=81Hz (red) and Corrected signal (dotted blue). (d) FFT of the Corrupted signal (red) and FFT of the Corrected signal (dotted blue).

Firstly, the shaker and PZT are vibrating at f=167Hz and 97Hz with an amplitude of 2µm and 2.5µm respectively (Fig. IV:15). Here, the corrupted SM measurement gives a completely distorted displacement estimation (Fig. IV:15 (a)) while the corrected measurement closely matches the PZT displacement (Fig. IV:15 (c)). In Fig. IV:15 (d), the comparison between the corrupted and corrected signal FFTs shows that the parasitic vibration is reduced by 28dB.

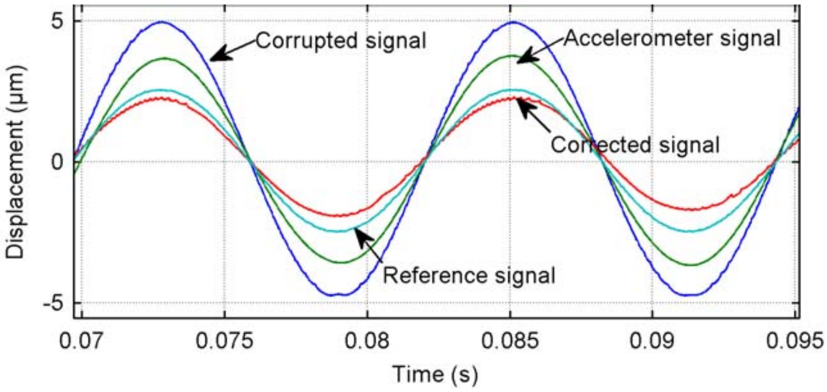

Fig. IV:16 Measured and Reconstructed displacement signals for f_{shaker}=81Hz and f_{PZT}=81Hz.

Secondly, in Fig. IV:16, the shaker and PZT are vibrating both at f=81Hz with an amplitude of 3.5µm and 2.5µm respectively while the corrupted SM measurement gives a wrong displacement amplitude of 5µm. This shows that the proposed method can properly recover the real target displacement even if the parasitic vibration is at the same frequency. This can frequently happen in the case of an undesirable mechanical coupling between the sensor assembly and the vibrating target. To further analyze the efficiency of the proposed method, including other examples not detailed here for brevity reasons, the displacement error ξ_{PZT} has been computed and summarized in Table IV-1.

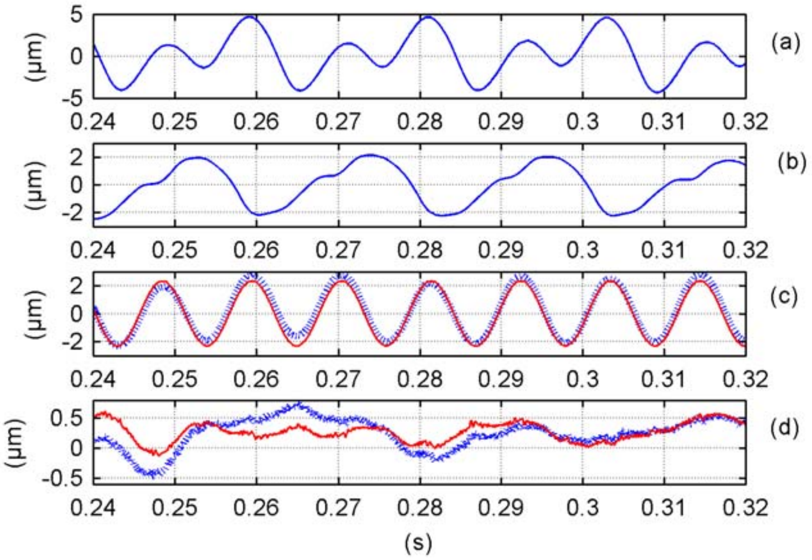

Fig. IV:17(a) Corrupted displacement signal for a single-tone versus an arbitrary signal with f_{shaker} =46Hz-92Hz-194Hz-276Hz and f_{PZT}=91Hz. (b) Accelerometer signal. (c) Reference signal (red) and Corrected signal (dotted blue). (d) Residual error for 10Hz-1kHz (red) and 40Hz-1kHz bandwidths (dotted blue) with respect to the SM reference signal.

Finally, two other cases are presented where firstly, the Shaker is vibrating at a single-tone frequency while the PZT is vibrating with an arbitrary signal (Fig. IV:17) and secondly, two different arbitrary signals are applied to the Shaker and PZT (Fig. IV:18). The residual error for each of these cases is presented in Fig. IV:17 (d) and Fig. IV:18 (c) respectively and summarized in Table II.

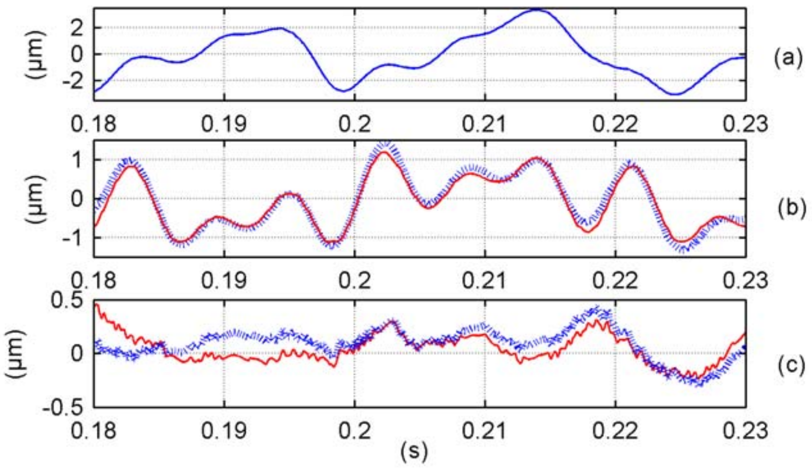

Fig. IV:18 (a) Corrupted displacement signal for two arbitrary signals with f_{shaker}=46Hz-92Hz-194Hz-276Hz and f_{PZT}=26Hz-104Hz-216Hz. (b) Reference signal (red) and Corrected signal (dotted blue). (c) Residual error for 10Hz-1kHz (red) and 40Hz-1kHz bandwidths (dotted blue) with respect to the SM reference signal.

IV.2.5 Results and Discussion

Depending on the low cut-off frequency, the proposed method using the ADXL311 achieves approximately an averaged resolution of 306nm (σ = 38nm) for a 20Hz-500Hz bandwidth and of 195nm (σ = 54nm) for a 40Hz-500Hz bandwidth (Table IV-1) when compared with the PZT reference signal.

Note that these errors include those added by possible misalignment between LD and target as well as the inaccuracy of the displacement extraction algorithm. Then, in order to reduce the influence of these errors, the SM based displacement signal obtained in the absence of parasitic signals (the shaker is off) can be used as a reference. Such a signal, obtained for the same PZT displacement is referred here as the SM reference signal. Based on this reference, the improved averaged resolutions of 275nm (σ = 31nm) for a 20Hz-500Hz bandwidth and of 137nm (σ = 39nm) for a 40Hz-500Hz bandwidth are presented in Table IV-2.

PZT (Hz)	Shaker (Hz)	ξ_{PZT} (µm)	
		20Hz-500Hz	40Hz-500Hz
63	63	0.312	0.259
81	81	0.366	0.287
105	105	0.247	0.149
61	45	0.329	0.222
72	54	0.271	0.147
72	93	0.286	0.172
47	225	0.3	0.183
97	167	0.338	0.143

Table IV-1 Corrected displacement RMS error ξ_{PZT} *as compared to the PZT reference signal.*

It is interesting to note that the obtained resolution is mainly limited by the accelerometer noise. Actually, based on eq. (4-3) and assuming a typical $300\mu g/\sqrt{Hz}$ noise floor, the displacement resolution obtained after processing the accelerometer signal is 480nm and 169nm for a 20Hz-500Hz and 40Hz-500Hz bandwidths respectively. Therefore, it is expected that lower cut-off frequency and higher displacement resolution can be achieved using lower noise accelerometers. Consequently, if a $1\mu g/\sqrt{Hz}$ accelerometer were used, nano-metric vibration displacement resolution can be achieved at even lower frequencies. Note also that according to eq. (4-3), for high frequency vibrations (>500Hz), high-g accelerometer sensor with poorer accelerometer resolution can be used. Therefore, depending on the targeted applications, a specific accelerometer should be used.

PZT (Hz)	Shaker (Hz)	ξ_{SM} (µm)	
		20Hz-500Hz	20Hz-500Hz
63	63	0.252	0.186
81	81	0.279	0.17
105	105	0.212	0.086
61	45	0.306	0.188
72	54	0.263	0.133
72	93	0.267	0.108
47	225	0.296	0.179
97	167	0.321	0.104
91	Arb.	0.264	0.108
Arb.	Arb.	0.293	0.113

Table IV-2 Corrected displacement RMS error ξ_{SM} *as compared to the SM reference signal.*

IV.3 Optimised Trigonometric Functions

The real-time hardware implementation of a SM displacement sensor algorithm necessitates the optimization of trigonometric functions such as *sin* and *arccos*, needed for its signal processing. For example, the *arccos* is needed to extract the excess fringe of the SM signal that represents the target movement under weak feedback regime. In this regard, two approaches, the limited Taylor series as well as the CORDIC (for COordinate Rotation DIgital Computer) method traditionally used in computer systems, have been evaluated for the implementation of these trigonometric functions. The increasingly higher ordered Taylor series cases have been compared along with their 12 bit and 16 bit fixed point implementations. Efforts have been done to optimize these trigonometric functions in order to reduce the error as well as the time needed for a future real-time sensor requiring such signal processing.

IV.3.1 Introduction

The present section concentrates on adapting these trigonometric identities in order to optimize result precision, area and timing constraints. For a real time hardware based sensor, the objective remains the design of a totally combinational structure that shall minimize the propagation time even at a possible cost of increased surface area of the chip. For the implementation of trigonometric functions such as *sin* or *arcsin* etc, two approaches, the limited Taylor series along with their 12 bit and 16 bit fixed point implementations as well as the CORDIC method traditionally used in computer systems, have been considered. The increasingly higher ordered reduced Taylor series based modules have been found to be attractive due to their combinational structure and the availability of embedded hardware multipliers in FPGAs. CORDIC modules are sequential structures, which require increasingly longer loops to reduce imprecision, and can only become an option in the case of non-availability of hardware multipliers. Furthermore, the use of ROM tables in conjunction with Taylor series based modules has been proposed to further reduce the error. These steps thus remain a key part in the consideration of timing constraints of the development of a real-time laser system in package dedicated to displacement measurement.

IV.3.2 Reduced Taylor series based functions

The *sin* function can be realized using the Taylor series as in (4-5) where x is the input phase in radians and n is the order of the series. For a limited range of x from $-pi/2$ to $pi/2$, the order of the Taylor series can be reduced without adding considerably large error, thus limiting the hardware multipliers eventually needed.

$$\sin x = x - \frac{x^3}{3!} + \frac{x^5}{5!} - \frac{x^7}{7!} + \cdots = \sum_{n=0}^{\infty} \frac{(-1)^n x^{2n+1}}{(2n+1)!} \tag{4-5}$$

Likewise, '*arcsin*' function can be calculated using the power series in (4-6) for input phase *z* in radians:

$$\begin{aligned} \arccos z &= \frac{\pi}{2} - \arcsin z \\ &= \frac{\pi}{2} - (z + \left(\frac{1}{2}\right)\frac{z^3}{3} + \left(\frac{1\cdot 3}{2\cdot 4}\right)\frac{z^5}{5} + \left(\frac{1\cdot 3\cdot 5}{2\cdot 4\cdot 6}\right)\frac{z^7}{7} + \cdots) \\ &= \frac{\pi}{2} - \sum_{n=0}^{\infty} \left(\frac{(2n)!}{2^{2n}(n!)^2}\right)\frac{z^{2n+1}}{(2n+1)}; \qquad |z| \le 1 \end{aligned} \tag{4-6}$$

where, once again, only lower order series shall be considered for the same reason as outlined before.

IV.3.3 CORDIC based functions

The CORDIC method [105] has been used regularly in integrated systems for calculating various trigonometric functions. It has remained popular for its ability to calculate the results using the simple operations of add, subtract and shift while using small Look-Up Tables (LUTs). It has been used for handheld calculators where the computation time has not been a priority as it required increasing iterations to finally obtain the needed accuracy. In fact, the CORDIC algorithm achieves the accuracy of one binary place with each execution of its loop, thus the final accuracy after the binary place is directly proportional to the iterations executed.

IV.3.4 Results

IV.3.4.a Error Analysis

In order to satisfy the area and timing constraints imposed by the working conditions of a real time displacement sensor, truncated or limited series implementations have been studied. The error introduced by such modules has been calculated and compared in order to find the optimum module with an acceptable error while respecting the timing and area constraints.

The averaged absolute percentage error for increasingly higher ordered limited Taylor series has been calculated for three cases:

- standard floating point 64 bit ‘Double’ type structure.
- 16 bit fixed point structure with 14 bit fractional part.
- 12 bit fixed point structure with 10 bit fractional part.

The error is found based on 2000 evenly spaced input samples from *–pi/2* to *+pi/2* in the case of *sin* or *cos* functions and from –1 to1 in the case of *arcsin* or *arccos* functions (see Fig. IV:19) as well as for linearly increasing number of iterations of CORDIC method (see Table IV-3).

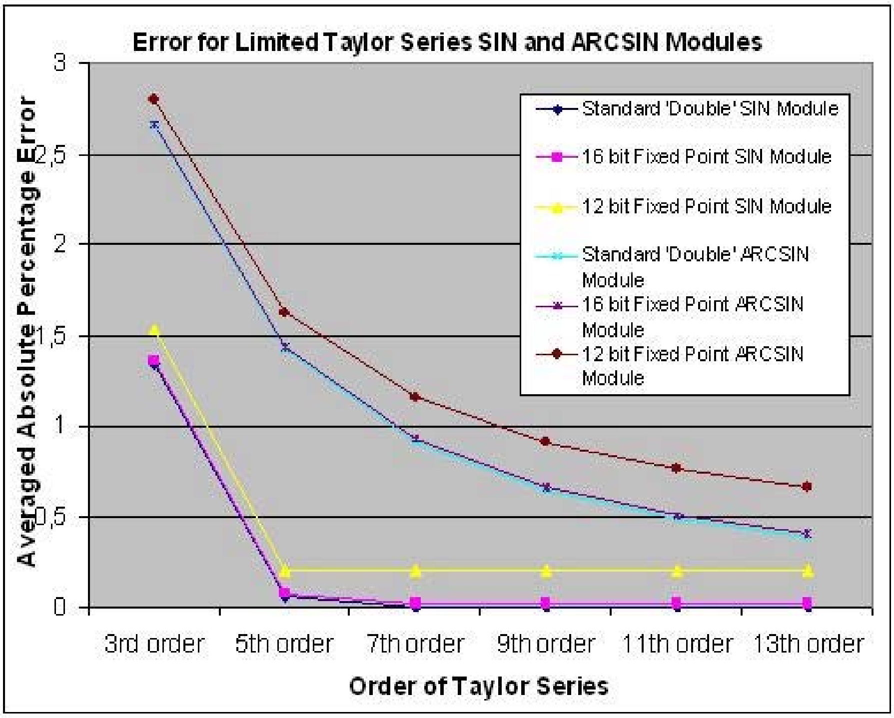

Fig. IV:19 Averaged absolute percent error for limited Taylor series sin *and* arcsin *modules.*

No. of CORDIC Iterations	7	8	9	10	11	12
CORDIC Error for SIN	2.6223	1.8176	0.647	0.2902	0.0858	0.0891

Table IV-3. Evolution of averaged absolute percentage error in a CORDIC based sin *module.*

IV.3.4.b Error Distribution

Fig. IV:20 shows the percentage error distributions for limited Taylor Series and CORDIC based *sin* modules for input interval from *–pi/2* to *+pi/2*. It is seen for limited Taylor series that most of the error resides in the last 20% of possible input interval where as the CORDIC presents larger error spread around zero. Thus, Taylor series based approach is preferred whose relatively smaller error, most of which is concentrated at the far ends, which can further be reduced as proposed later in the section.

IV.3.4.c Hardware Usage

The hardware cost, i.e. the number of LUTs as well as the slices consumed (Fig. IV:21) and the embedded multipliers for the limited Taylor series implementations (Fig. IV:22) have also been estimated for the fixed-point cases for a Xilinx Spartan III FPGA. This evaluation has been achieved by ISE Xilinx software with XST as synthesis tool.

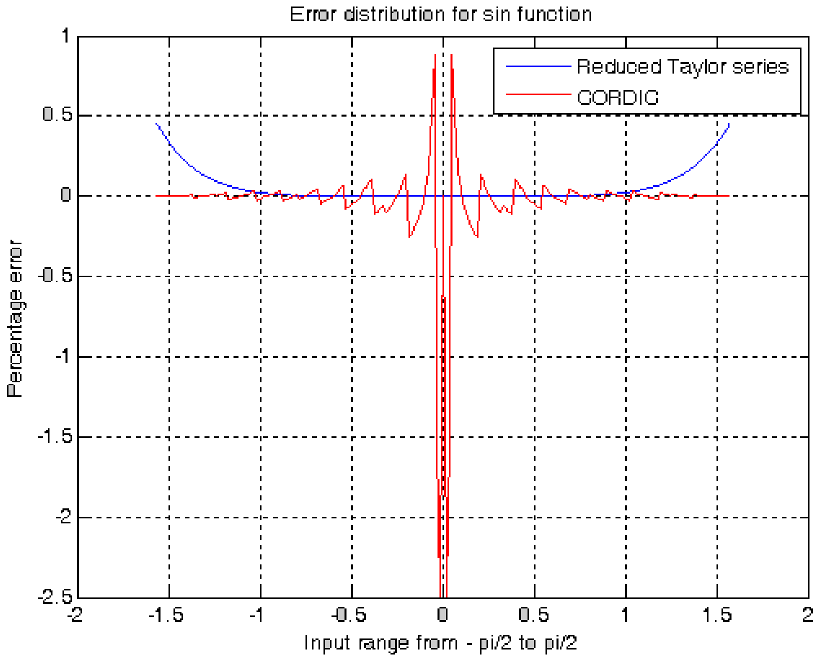

Fig. IV:20. Percentage error distribution for Taylor Series and CORDIC implementations.

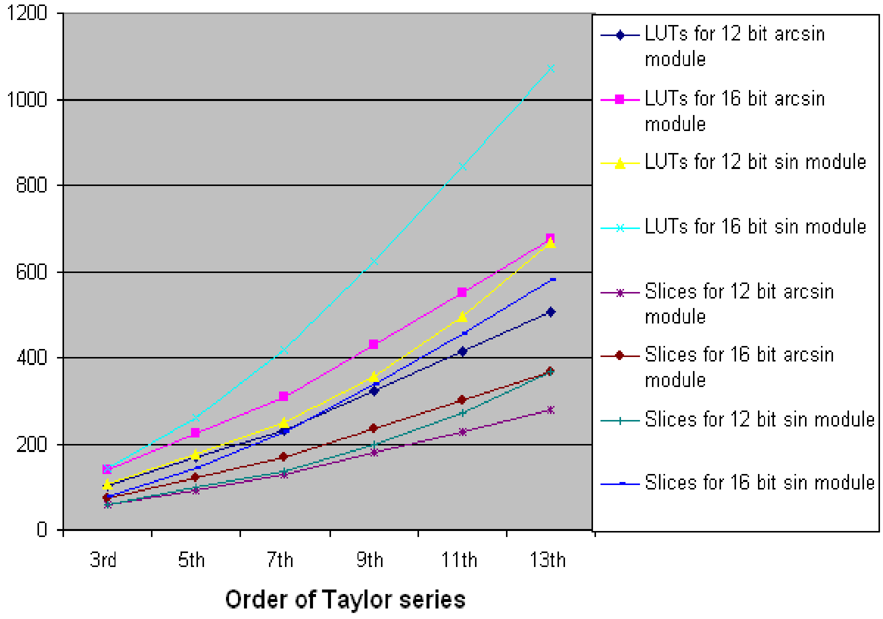

Fig. IV:21. Hardware cost for limited Taylor series based sin *and* arcsin *modules.*

IV.3.4.d Interpretation

The error, as expected, continuously reduces for increasingly higher ordered series modules (Fig. IV:19). However, for fixed-point architectures, it soon becomes a constant and if ever, rises a little as a result of the error added by the rounding off of numbers in higher ordered terms as seen in Table IV-4. Thus, we can see the effect of truncation caused by the fix point coding to represent the different real numbers.

Order of Taylor Series	3	5	7	9	11	13
Error difference between 12 bit and 16 bit	0.130	0.186	0.229	0.243	0.252	0.257

Table IV-4. Percentage error difference between 12 and 16 bit arcsin *modules*

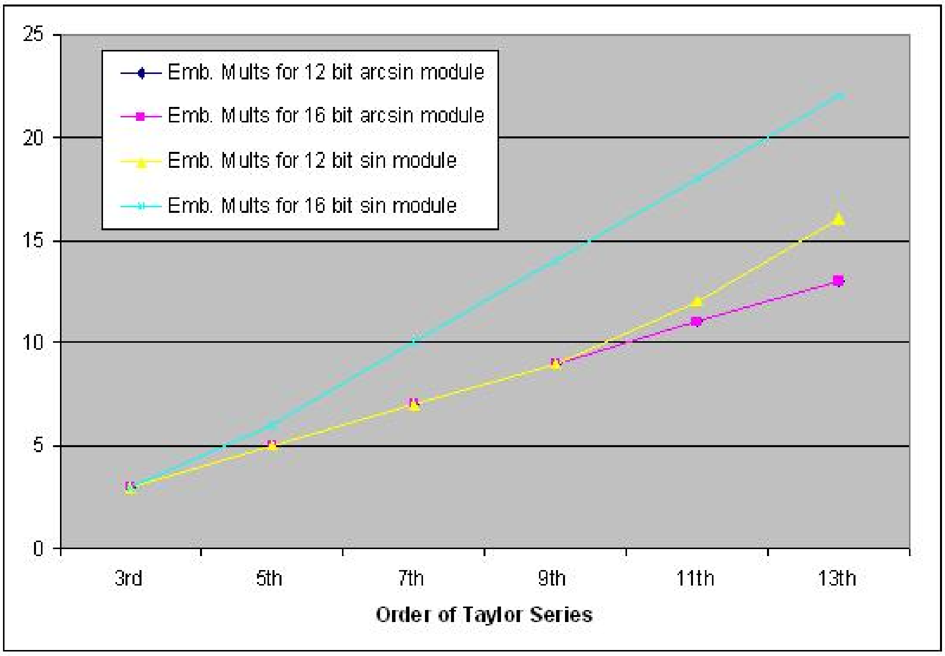

Fig. IV:22. Number of Embedded Multipliers for limited Taylor series based arcsin *and* sin *modules.*

Globally, it is seen that the 12 bit vector with 10 bits fractional part module is quite useful. Furthermore, by choosing an implementation of 3rd or 5th order, one can significantly reduce the hardware resources as compared to higher order implementations while adding no significant error to the trigonometric function results. Thus, in case of *arcsin* modules, for a 5th order 12 bit implementation, an averaged error of only **1.6 %** is introduced. A real number 5th order implementation as compared to 12 bit structure only reduces the error by **0.2 %.**

So, a considerable saving in hardware implementation is seen, e-g for a 12 bit module as compared with a 16 bit module, only an averaged error of **0.186%** is added while saving important hardware resources i.e. a saving of **23 %** in Slices and **24%** in LUTs is seen. This hardware resources ratio is seen for all the series i.e. from the 3rd order to the 13th order series.

Thus, the optimal results are for the 5th order 12 bit Taylor series implementation as compared to other Taylor series variants as well as the sequential CORDIC method. For the *sin* module, it provides sufficiently accurate results (error of 0.0589%) without causing huge hardware costs. This result is still better than 12th iteration CORDIC *sin* module (Table IV-4). The added benefit is the totally combinational implementation, thus reducing the total time needed for the operation.

IV.3.4.e Improvement for Taylor based arcsin modules

The error distribution for the *arcsin* or *arccos* implementations based on reduced Taylor series show that for a possible input interval of 0 to |1|, a huge proportion of error already indicated in Fig. IV:19 resides in the interval of |0.8| to |1|. The Table IV-5 thus shows that more than 90% of total error caused by limited series usage resides only in the 20% of the total possible input interval. It is proposed to use a ROM table dedicated to this input interval, which will contain the respective *sin* or *arcsin* value. The eventual error in the ROM table will depend on the length of the table and the fixed-point vector length to represent the function value. Thus, by using a 3rd order or 5th order Taylor module in conjunction with a ROM table, significant further improvement in the precision of the module can be achieved.

Order of Taylor Series	3	5	7	9	11	13
Error for SIN in [|1| |0.8|]	75.9	86.6	92.4	95.6	97.4	98.5

Table IV-5. Percentage error for Taylor series based SIN in 1 to 0.8 interval

IV.3.5 Hardware FPGA Implementation

In order to use the designed algorithms as a part of a real-time system, the hardware implementation scheme has been thought upon. The schematic diagram of the future sensor is presented in Fig. IV:23. A signal processing card, equipped with an FPGA shall be used to acquire the signals from the LD chip as well as the reference sensor.

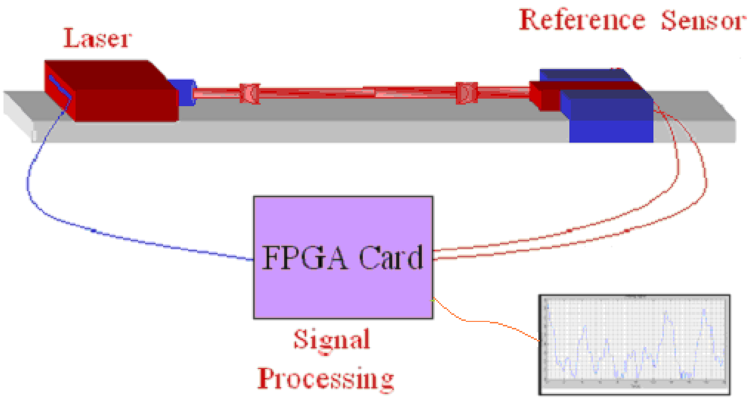

Fig. IV:23 The schematic diagram for the hardware implementation of the SM displacement sensor.

Fig. IV:24 presents in detail various other components added to the card that shall interact with the FPGA. The prototype card has a 4 channel Analog to Digital Conversion (ADC) as well as Digital to Analog conversion (DAC) capacity where each channel ran process up to 125 (MSPS Mega Samples Per Second). The chosen FPGA is a SPARTAN-3A that has a capacity of 3.4 Million logic gates and has clock frequency of 250MHz. Such high sampling frequency for the ADC and DAC coupled with a high clock shall make it possible to correctly process the SM signals. The FPGA has an interface with the external environment via the RS232 and USB communication ports. The FPGA has also access to an external RAM for sample storage.

The card is in the testing phase and its completion shall allow us to implement the SM displacement processing algorithms on the FPGA.

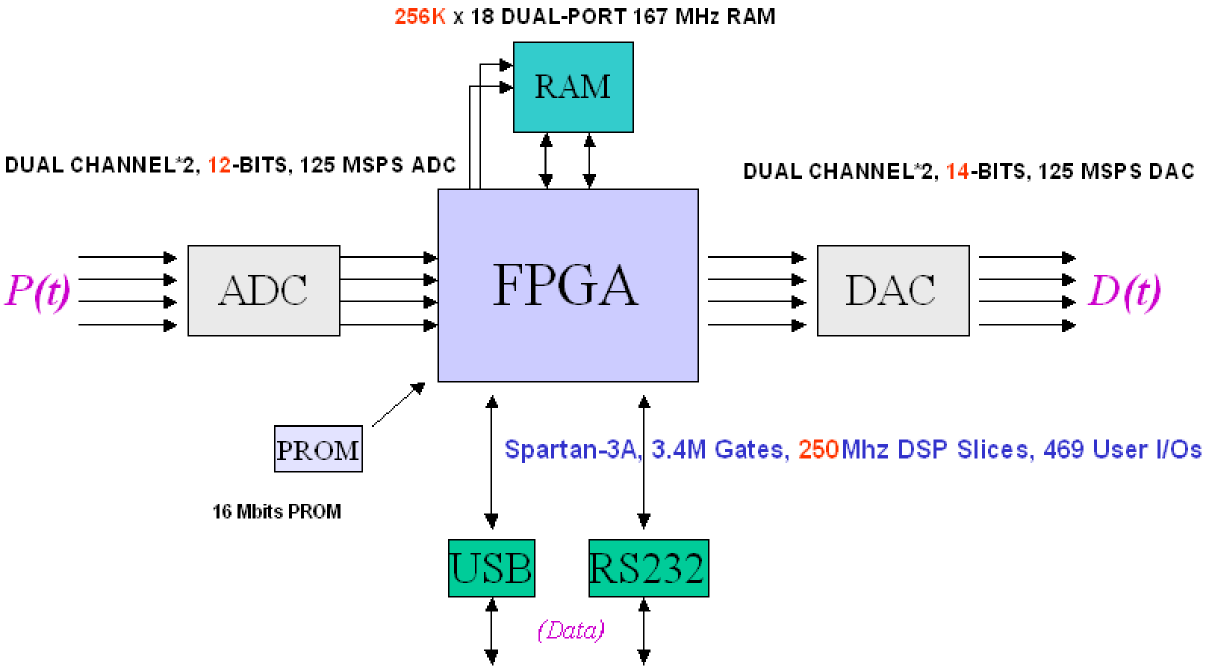

Fig. IV:24 The schematic diagram of the SM signal processing card.

IV.3.6 Assessment of Optimised Functions

It is seen that, due to the availability of embedded multipliers in the FPGA device or ASIC chip, it is presently more interesting to use Taylor series to realize trigonometric identities, than the CORDIC method, widely used in computer systems. This method enables us to find the good compromise between the area, the propagation time and the tolerable error. Furthermore, this implementation is totally combinatorial, decreasing the time to calculate the output value, thus helping in the cause of a real time LD displacement sensor.

IV.4 Conclusion

After a verification of the novel displacement measurement approaches, as presented in the last chapter, that have resulted in a faster calculation of displacement, a correction of the fringe-loss for harmonic vibrations, an adaptability of the sensor to automatically adjust itself to a change in the optical feedback regime, as well as the possibility of using a liquid lens to stay in a favourable feedback regime, it was decided to improve the behaviour of the resultant sensor with respect to its usage in industrial conditions.

Such a use implies the presence of such effects such as misalignment and non-cooperative target surfaces that increase the possibility of encountering speckle and/or presence of parasitic mechanical vibrations to the sensor either due to an unwanted mechanical coupling between the observed target and the sensor assembly or stray, ambient movements in the industrial milieu that would falsify the measurement. Thus, in this chapter, solutions to each of these two issues have been presented that shall allow us to accurately measure the target displacement even under unfavourable conditions. The other sections of this chapter presented the early work done for the hardware implementation of the sensor algorithms.

Conclusion & Future Works

The thesis was started with a desired aim of designing a self-mixing based displacement measuring system that would be auto-adaptive, of a real-time nature, robust to external perturbations while providing a measurement precision of better than the basic half-wavelength. It was also expected that the sensor would be able to go beyond the often-reported micrometric measurement range and extend it to centimetric range. Likewise, it was desired that it would provide precise results even in the presence of varying optical feedback and non-cooperative target surfaces.

In this regard, an existing displacement measuring algorithm called the phase unwrapping method was studied to adapt it to our needs as it could only measure displacement under moderate feedback regime and had static self-mixing fringe detection. Another drawback of the said method was the time consumed during a two-dimensional minimization procedure that is an inherent part of it. So, initial studies were done to optimize the Nelder-Mead Simplex technique used for this minimization. Likewise, an FFT based approach was also tested to replace this optimisation procedure. Finally, a hybrid optimisation algorithm was designed that has appreciably reduced the calculation time needed to converge to the optimised values.

Then, using the experience of these studies, another algorithm was designed that does not need any optimisation procedure and is of a real-time nature. This method has also provided a solution to the issue of fringe-loss in self-mixing that occurs due to increased feedback and causes error in measurement. A disappearance of up to four fringes has been detected and compensated to provide a precision of about 50nm for target vibrations of the order of 5µm.

Likewise, another algorithm has also been designed that removes the initially used static fringe detection by an auto-adaptive fringe transition detection technique. It is capable of distinguishing the very weak, weak, moderate and strong feedback regimes. The target displacement results for the various weak and moderate feedback regime signals coming from different lasers and media were obtained and were in good agreement with a commercial reference sensor.

The possibility of using adaptive optics in the form of a liquid lens has also been studied during this thesis. It has been shown that it can be used to maintain the self-mixing feedback to a level such that self-mixing fringes keep their saw-toothed shape while avoiding a possible fringe-loss. Furthermore, it has also allowed us to increase the laser-to-target distance range over which a stable signal can be achieved.

Furthermore, displacement measurement with centimetric amplitude also been demonstrated for a non-cooperative target surface. The influence of the speckle phenomenon is decisive under such operating conditions and a processing technique has been proposed that allows us to recover the displacement information from the speckle-affected self-mixing signals.

In order to make the sensor robust to the parasitic mechanical vibrations that would falsify the measurement results, an innovative technique has been tested that is based on a solid-state accelerometer coupled with the self-mixing sensor. Our sensor has thus recovered an arbitrary or harmonic target displacement while subjected to an arbitrary or harmonic parasitic vibration. The present set-up, using an accelerometer costing 3 euros, provides a residual error of 300nm that can be easily reduced by using a better accelerometer.

At present, a FPGA based electronic card incorporating the self-mixing sensor is being designed so that the various algorithms can be deployed onto it. In case of successful implementation, a robust, reliable and autonomous sensor will come to life.

The research undertaken during the thesis will provide a good starting point for future research endeavours. For example, the FFT based displacement retrieval technique can be used along with a self-mixing velocimeter.

Likewise, the hybrid optimisation algorithm needs to be tested for those signals where the optical feedback parameter continuously varies. In case of a correct tracking of this parameter, such a system, while measuring the target displacement, can be used to recover additional information about the target surface or the medium between the laser and the target.

Another option is to extract the fringe information by an analogue technique. This can be achieved by separating the high frequency component (representing the transitions) from the low frequency component (representing the fringe shape) of the self-mixing signal. Then, the transition information can be directly fed to the fringe-loss compensation algorithm to reconstruct the target displacement. Such a technique would also reduce the analogue-to-digital conversion needs of the system.

The successful use of liquid lens for self-mixing sensing applications also presents certain possibilities. For example, the growth of such a lens on to the laser diode substrate can allow increased control while resulting in a miniaturisation of the system. A thesis on a related subject has started in a sister laboratory and can be used to further advance the work.

Finally, the perspective of a complete System in Package (SiP) containing the laser diode, its driving and self-mixing signal extraction circuitry, a signal processing ASIC and an embedded accelerometer, shall continue to propel further research in this versatile field.

References

[1] P.G.R. King & G.J. Steward, "Metrology with an optical maser", New Scientist 17, 180 (1963).

[2] M.J. Rudd, "A laser Doppler velocimeter employing the laser as a mixer-oscillator", Journal of Physics E1, 723-726 (1968).

[3] J.H. Churnside, "Laser Doppler velocimetry by modulating a CO2 laser with backscattered light", Applied Optics 23(1), 61-66 (1984).

[4] J.H. Churnside, "Signal-to-noise in a backscatter-modulated Doppler velocimeter ", Applied Optics 23(13), 2097-2101 (1984).

[5] A. Dandridge, R.O. Miles & T.G. Giallorenz, "Diode laser sensors", Electronics Letters 16, 948-949 (1980).

[6] T. Bosch, C. Bes, L. Scalise, G. Plantier, “Optical Feedback Interferometry”, Encyclopedia of Sensors, vol. 7, pp 107-126, American Scientific Publishers, USA, (2006).

[7] S. Donati, “Electro-Optical Instrumentation: Sensing and Measuring with Lasers”, Upper Saddle River, NJ: Prentice-Hall, ch. 4, (2004).

[8] T. Bosch, “An overview of self-mixing applications”, IEEE COMMAD04 invited paper, (2004).

[9] G. Giuliani, M. Norgia, S. Donati and T. Bosch, “Laser diode self-mixing technique for sensing applications”, Journal of Optics A: Pure and Applied Optics, Vol. 4, pp. 283-294, (2002).

[10] G. Giuliani, S. Donati, “Laser interferometry”, Unlocking dynamical diversity: optical feedback effects on semiconductor lasers, D. M. Kane and K.A. Shore, Ed. Chichester: John Wiley & Sons, Ltd, pp. 217-256, (2005).

[11] K. Otsuka, T. Ohtomo, H. Makino, S. Sudo, and J.Y. Ko, “Net motion of an ensemble of many Brownian particles captured with a self-mixing laser”, Applied Physics Letters, Vol. 94, Issue 24, pp. 241117 - 241117-3, (2009).

[12] D. Larsson, A. Greve, J. Hvam, A. Boisen, K. Yvind, "Self-mixing interferometry in vertical-cavity surface-emitting lasers for nanomechanical cantilever sensing", Applied Physics Letters, Vol. 94, Issue 9, pp. 091103 - 091103-3, (2009).

[13] Christian Zakian and Mark Dickinson, "Laser Doppler imaging through tissues phantoms by using self-mixing interferometry with a laser diode", Optics Letters, Vol. 32, No. 19, pp 2798-2800, (2007).

[14] G. Mourat, "Etude de diodes laser pour des applications métrologique de la rétro-injection optique ", PHD INPT; No: 1561, (2006).

[15] Yah Leng Lim, K. Bertling, Pierre Rio, J. R. Tucker, A. D. Rakić, "Displacement and Distance Measurement using the Change in Junction Voltage across a Laser Diode due to the Self-Mixing Effect", Proceedings of SPIE 6038, pp.378-387 (2006).

[16] Kliese, R.; Yah Leng Lim; Bertling, K.; Bakar, A.A.A.; Bosch, T.; Rakic, A.D. , "Self-mixing displacement sensing using the junction voltage variation in a GaN laser" Proceedings of the 2008 IEEE Conference on Optoelectronic and Microelectronic, Materials and Devices, pp 23-25, (2008).

[17] Perchoux, J.; Dougan, H.E.; Bony, F.; Rakic, A.D., "Photodiode-free Doppler velocimeter based on self-mixing effect in commercial VCSELs", IEEE Sensors conference, pp. 290 – 293, (2008).

[18] K. Petermann, "Laser diode modulation and Noise", Kluwer academic Publishers, Dordrecht (1991).

[19] W.M. Wang, W.J.O. Boyle, K.T.V. Grattan & A.W. Palmer, "Self-mixing interference in a diode laser : experimental observations and theoretical analysis", Applied Optics 32(9), 1551-1558 (1993).

[20] Acket G A, Lenstra D, Den Boef A J and Verbeek B H, "The influence of feedback intensity on longitudinalmode properties and optical noise in index-guided semiconductor lasers", IEEE Journal of Quantum Electronics, Vol 20, pp 1163–1169, (1984).

[21] L. Golderg, H. F. Taylor, A. Dandridge, J. F. Weller, and R. O. Miles, "Spectral Characteristics of Semiconductor Lasers with Optical Feedback" IEEE J. Quantum Electron, Vol. QE-18,pp. 555-564, (1982).

[22] R. W. Tkach and A. R. Chraplyvy, “Regimes of feedback effects in 1.5 pm distributed feedback lasers,” Journal of Lightwave Technology, Vol. LT-4, pp. 1655-1661,(1986).

[23] Junji Ohtsubo,“Semiconductor lasers: stability, instability and chaos”, Springer series in optical sciences, Springer, Berlin, (2006).

[24] N. Servagent, “Etude et conception de capteurs optoélectroniques auto-alignés de distances et d&placements pour le contrôle non destructif,” Thesis of Institut National Polytechnique de Toulouse, (1997).

[25] W.M. Wang, K.T.V. Grattan, A.W. Palmer & W.J.O. Boyle, "Self-mixing interference inside a single-mode diode laser for optical sensing applications", Journal of Lightwave Technology 12(9), pp. 1577-1587 (1994).

[26] R. Justaitis, N. P. Rea, and T. Wilson, "Semiconductor laser confocal microscopy," Applied Optics, vol. 33, pp.578-584, (1994).

[27] G. Giuliani, S. Bozzi-Pietra and S. Donati, “Self-mixing laser diode vibrometer”, Meas. Sci. Technol. 14, pp. 24-32, (2003).

[28]. S. Donati, “Laser interferometry by induced modulation of the cavity field”, Journal of Applied Physics, Vol. 49, pp. 495-497, (1978).

[29]. S. Shinoara, A. Mochizuki, H. Yoshida and M. Sumi, “Laser Doppler velocimeter using the self-mixing effect of a semiconductor laser diode”, Applied Optics, Vol. 25, pp. 1417-1419, (1986).

[30]. Beheim G. and Fritsch K., “Range finding using frequency modulated laser diode”, Applied Optics, Vol. 25, pp. 1439-1442, (1986).

[31]. J. G. Webster, “The Measurement, Instrumentation and Sensors Handbook,” CRC Press, p. 29, (1998).

[32] Girao, P.M.B.S.; Postolache, O.A.; Faria, J.A.B.; Pereira, J.M.C.D.; “An Overview and a Contribution to the Optical Measurement of Linear Displacement”, IEEE Sensors Journal, Vol 1 , Issue 4, pp. 322 – 331, (2001).

[33] Ottonelli, S.; De Lucia, F.; di Vietro, M.; Dabbicco, M.; Scamarcio, G.; Mezzapesa, F.P., “A Compact Three Degrees-of-Freedom Motion Sensor Based on the Laser-Self-Mixing Effect” IEEE Photonics Technology Letters, Volume 20, Issue 16, pp.1360 – 1362, (2008) .

[34] N. Servagent, T. Bosch, and M. Lescure, “Design of a phase-shifting optical feedback interferometer using an electro-optic modulator,” IEEE Journal of Selected Topics on Quantum Electron, Vol.6, no. 5, pp. 798–802, (2000).

[35] N. Servagent, F. Gouaux, and T. Bosch, “Measurements of displacement using the self-mixing interference in a laser diode,” Journal of Optics, Vol. 29, no. 3, pp. 168–173, (1998).

[36] N. Takahashi, S. Kakuma, and R. Ohba, “Active heterodyne interferometric displacement measurement using optical feedback effects of laser diodes,” Optical Engineering, vol. 35, pp. 802–807, (1996).

[37] X. Cheng and S. Zhang, “Multiple self-mixing effect in vcsels with asymmetric external cavity,” Optics communications, vol. 260, pp. 50–56, (2006).

[38] Marta Ruiz-Llata and Horacio Lamela , “Self-mixing technique for vibration measurements in a laser diode with multiple modes created by optical feedback”, Applied Optics, Vol. 48, No. 15, pp. 2915-2923, (2009).

[39]. C. Bes, G. Plantier and T. Bosch, “Displacement Measurements Using a Self-mixing Laser Diode Under Moderate Feedback”, IEEE Trans. On Instrumentation and Measurement, Vol. 55, No. 4, pp. 1101-1105, (2006).

[40]. C. Bes, V. Belloeil, G. Plantier, Y. Gourinat and T. Bosch, “A self-mixing laser sensor design with an extended Kalman filter for optimal online structure analysis and damping evaluation”, IEEE/ASME Trans. on Mechatronics, Vol. 12, No. 3, pp. 387-394,(2007).

[41] C. Bes, T. Bosch, G. Plantier and F. Bony, "Characterisation of a self-mixing displacement sensor under moderate feedback". Optical Engineering, Vol. 45, No. 8, pp. 084402-1 – 084402-6, (2006).

[42]. A. Doncescu, C. Bes and T. Bosch, “Displacement Estimation with an Optical Feedback Interferometer Using an Evolutionary Algorithm”, Proceedings of IEEE Sensors 2007, Atlanta, (2007).

[43]. S. Donati, G. Giuliani and S. Merlo, “Laser diode feedback interferometer for measurement of displacements without ambiguity”, IEEE J. Quantum Electron., Vol. 31, pp. 113-119, (1995).

[44]. P. A. Roos, M. Stephens, and C. E. Wieman, "Laser vibrometer based on optical-feedback induced frequency modulation of a single-mode laser diode", Applied Optics, Vol. 35, pp. 6754-6761, (1996).

[45]. G. Giuliani, S. Bozzi-Pietra, and S. Donati, "Self-mixing laser diode vibrometer," Measurement Science and Technology, Vol. 14, pp. 24-32, (2003).

[46]. L. Scalise, Y. Yu, G. Giuliani, G. Plantier, and T. Bosch, "Self-mixing laser diode velocimetry: application to vibration and velocity measurement," IEEE Transactions on Instrumentation and Measurement, Vol. 53, pp. 223-232, (2004).

[47]. M. Norgia,C. Svelto,"Novel Measurement Method for Signal Recovery in Optical Vibrometer", IEEE Transactions on Instrumentation and Measurement, Vol. 57, Issue 8, pp.1703 – 1707, (2008).

[48] http://www.sensorcentral.com/displacement/laser01.php

[49] Y. Jourlin and J. Jay, O. Parriaux , "Compact diffractive interferometric displacement sensor in reflection", Precision Engineering, Vol. 26, pp. 1–6, (2002).

[50]. R. J. Adrian, "Selected Papers on Laser Doppler Velocimetry," SPIE, Bellingham, (1993).

[51]. S. Shinohara, A. Mochizuki, H. Yoshida, and M. Sumi, "Laser Doppler velocimeter using the self-mixing effect of a semiconductor laser diode," Applied Optics, Vol. 25, pp. 1417-1419, (1986).

[52]. A. van der Lee, M. Carpaij, H. Moench, M.Schemmann, and A. Pruijmboom, "A miniaturized VCSEL based sensor platform for velocity measurement", Proc. of the 25th IEEE International Instrumentation and Measurement Technology Conference, pp 141-143, (2008).

[53]. J. Albert, M. C. Soriano, I. Veretennico, K. Panajotov, J. Danckaert, P. A. Porta, D. P. Curtin, and J. G. McInerney, "Laser doppler velocimetry with polarization-bistable VCSELs," IEEE Journal Of Selected Topics In Quantum Electronics, Vol. 10, pp. 1006-1012,(2004).

[54]. X. Raoul, T. Bosch, G. Plantier and N. Servagent, "A double-laser diode onboard sensor for velocity measurement," IEEE Transactions on Instrumentation and Measurement, Vol. 53, pp. 95-101, (2004).

[55]. G. Plantier, N. Servagent, A. Sourice, and T. Bosch, "Real-time parametric estimation of velocity using optical feedback interferometry," IEEE Transactions on Instrumentation and Measurement, Vol. 50, pp. 915-919, (2001).

[56]. Shibata, T. Shinohara, S. Ikeda, H. Yoshida, H. Sawaki, T. and Sumi, H. "Laser speckle velocimeter using self-mixing laser diode", IEEE Trans. on Instrumentation and Measurement, Vol. 45, Issue 2, pp. 499-503, (1996).

[57]. S. K. Ozdemir, S. Ito, S. Shinohara, H. Yoshida, and M. Sumi, "Correlation-based speckle velocimeter with self-mixing interference in a semiconductor laser diode," Applied Optics, Vol. 38, pp. 6859-6865, (1999).

[58]. S. K. Ozdemir, S. Shinohara, S. Ito, S Takamiya and H. Yoshida, "Compact optical instrument for surface classification using self-mixing interference in a laser diode", Optical Engineering, Vol. 40, 38, (2001).

[59]. F. F. M. de Mul, L. Scalise, A. L. Petoukhova, M. Van Herwijnen, P. Moes, and W. Steenbergen, "Glass-fiber self-mixing intra-arterial laser Doppler velocimetry: Signal stability and feedback analysis," Applied Optics, Vol. 41, pp. 658-667, (2002).

[60]. M. H. Koelink, M. Slot, F. F. M. de Mul, J. Greve, R. Graa_, A. C. M. Dassel, and J. G. Aarnoudse, "Laser doppler velocimeter based on the selfmixing effect in a fiber-coupled semiconductor laser : theory," Applied Optics, Vol. 31, pp. 3401-3408, (1992).

[61]. S. K. Ozdemir, S. Takamiya, S. Ito, S. Shinohara, and H. Yoshida, "Selfmixing laser speckle velocimeter for blood flow measurement," IEEE Transactions on Instrumentation and Measurement, Vol. 49, pp. 1029-1035,(2000).

[62]. S.K. Ozdemir, I. Ohno, S. Shinohara, "A Comparative Study for the Assessment on Blood Flow Measurement Using Self-Mixing Laser Speckle Interferometer", IEEE Transactions on Instrumentation and Measurement, Vol. 57, Issue 2, pp. 355 – 363, (2008).

[63]. A. Courteville, T. Gharbi, and J. Y. Cornu, "Noncontact mmg sensor based on the optical feedback effect in a laser diode," Journal of Biomedical Optics, Vol. 3, pp. 281-285, (1998).

[64] M. A. Amann, T. Bosch, M. Lescure, R. Myllyla, and M. Rioux, "Laser ranging: a critical review of usual techniques for distance measurement",Optical Eng. Vol. 40, pp. 10-19, (2001).

[65]. F. Gouaux, N. Servagent, and T. Bosch, "Absolute distance measurement with an optical feedback interferometer," Applied Optics, Vol. 37, pp. 6684-6689, (1998).

[66] G Mourat, N Servagent, T Bosch *“Distance measurement using the self-mixing effect in a three-electrode distributed Bragg reflector laser diode”,* Optical Engineering, *Vol. 39, pp.738, (2000).*

[67] Peter J. de Groot, Gregg M. Gallatin, and Steven H. Macomber, "Ranging and velocimetry signal generation in a backscatter-modulated laser diode," Applied Optics, Vol. 27, pp. 4475-4480, (1988).

[68] JR Tucker, YL Leng, and AD Rakic, "Laser range finding using the self-mixing effect in a vertical- cavity surface-emitting laser," IEEE Conference on Optoelectronic and Microelectronic Materials and Devices, 583-583, IEEE, Sydney, Australia, (2002).

[69] Yah Leng Lim, Milan Nikolic, Karl Bertling, Russell Kliese and Aleksandar D. Rakic, “Self-mixing imaging sensor using a monolithic VCSEL array with parallel readout”, Optics Express, Vol. 17, Issue 7, pp. 5517-5525, (2009) .

[70]. http://newtonperipherals.com/MoGo_press_philips.html

[71]. http://optics.org/cws/article/research/9217

[72] C. Bes, “Conception d’un système laser de mesures de déplacements par interférométrie à rétro-injection optique dans le cas de feedbacks faible et modéré”, Ph.D thesis of l’Institut National Polytechnique de Toulouse, (2006).

[73] Y. Yanguang, G. Giuliani, and S. Donati, “Measurement of the linewidth enhancement factor of semiconductor lasers based on the optical feedback self-mixing effect,” IEEE Photonics Technology Letters, Vol. 16, no. 4, pp. 990–992, (2004).

[74] K. Petermann, “External optical feedback phenomena in semiconductor lasers,” IEEE Journal of Selected Topics on Quantum Electron., Vol. 1, no. 2, pp. 480–489, (1995).

[75] T. Bosch, U. Zabit and F. Bony, “Optimisation of the performances of a self-mixing laser diode displacement sensor under moderate feedback based on the Nelder-Mead simplex method”, The 2nd International conference on Sensing Technology, New Zealand, November 26-28, (2007).

[76] U. Zabit, F. Bony and T. Bosch, “Optimisation of the Nelder-Mead Simplex Method for Its Implementation in A Self-Mixing Laser Displacement Sensor”, Smart Sensors and Sensing Technology, Vol. 20, Springer, pp 381-400, (2008).

[77] J.A. Nelder and R. Mead, "A simplex method for function minimization.", Computer Journal 7, pp. 308-313, (1965).

[78] JC Lagarias, JA Reeds, MH Wright, PE Wright, "Convergence properties of the Nelder-Mead simplex algorithm in low dimensions.". SIAM Journal on Optimization, Vol. 9, No. 1, pp. 112-147, (1998).

[79] DM Olsson and LS Nelson, "The Nelder-Mead Simplex Procedure for Function Minimization.", Technometrics, Vol. 17, No. 1, pp. 45-51, (1975).

[80] U. Zabit, T. Bosch, and F. Bony, "A fast derivative-less optimization of the feedback coupling coefficient for a self-mixing laser displacement sensor", IEEE International Conference NEWCAS-TAISA 2009, Toulouse, France (2009).

[81] G.Plantier, C. Bes and T. Bosch, "Behavioral model of a self-mixing laser diode sensor", IEEE Journal of Quantum Electronics, vol. 41 (9), pp 1157-1167, (2005).

[82] M. J. D. Powell ,"An efficient method for finding the minimum of a function of several variables without calculating derivatives", The Computer Journal 7(2):155-162, (1964).

[83] Nocedal, J. and S.J. Wright, Numerical Optimization, Springer Series in Operations Research, Springer Verlag, (1999).

[84] Joseph El Assad, "Analysis of Self-Mixing Moderate and String Feedback Regimes for Mechantronics Applications" , PhD thesis submitted INP – ENSEEIHT, University of Toulouse,France, (2008).

[85] G.H.M. van Tartwijk and D. Lenstra, "Semiconductor lasers with optical injection and feedback", Quantum Semiclass. Opt. *Vol. 7, pp. 87-143, (1995).*

[86] U. Zabit, T. Bosch, F. Bony and A. D. Rakic , "A Self-mixing Displacement Sensor with Fringe-loss Compensation for Harmonic Vibrations", IEEE Photonics Technology Letters, vol. 22, No. 6, (2010).

[87] U. Zabit, T. Bosch, and F. Bony "Adaptive Transition Detection Algorithm for a Self-Mixing Displacement Sensor", IEEE Sensors Journal, Vol. 9, Issue 12, pp.1879 – 1886, (2009).

[88] M. Suleiman, H.C. Seat and T. Bosch, "Interrogation of Fibre Bragg Grating Dynamic Strain Sensors by Self-Mixing Interferometry". IEEE Sensors Journal, Vol. 8, No. 7, pp 1317-1323, (2008).

[89] S. Merlo and S. Donati, "Reconstruction of displacement waveforms with a single-channel laser-diode feedback interferometer". IEEE J. Quant. Elec. vol. 33, n° 4, PP 527-531, (1997).

[90] G. Giuliani, S. Donati, M. Passerini, and T. Bosch, "Angle measurement by injection detection in a laser diode", Opt. Eng., Vol. 40, 95, (2001).

[91] J. El Assad, T. Bosch, and G. Plantier, "Laser Diode Under Strong Feedback For Mechatronics Applications". Proc. IEEE Sensors 2007 Conference, pp 387-390, (2007).

[92] K. Kobayashi and R. Lang, "External optical feedback effects on semiconductor injection laser properties," IEEE J. Quant. Elec., vol. 16, no 3, pp. 347–355, (1980).

[93] U. Zabit, R. Atashkhooei, T. Bosch, S. Royo, F. Bony and A. D. Rakic, "Adaptive self-mixing vibrometer based on a liquid lens", Optics Letters, Vol. 35, No. 8, pp. 1278-1280, (2010).

[94] J.W.Hardy, "Adaptive optics for Astronomical Telescopes", Oxford University Press, Oxford, (1998).

[95] B. Potsaid, Y. Bellouard, and J. Wen, "Adaptive Scanning Optical Microscope (ASOM): A multidisciplinary optical microscope design for large field of view and high resolution imaging", Optical Express, 13, 6504 (2005).

[96] M. Ares, S.Royo "Adaptive optics system to compensate complex-shaped wavefronts", Adaptive Optics for Industry and Medicine, C.Dainty Ed. Oxford University Press, Oxford (1998).

[97] B. Berge and J. Peseux, "Variable focal lens controlled by an external voltage: An application of electrowetting", Eur. Phys. J. E 3, 159 (2000).

[98]. J. C. Dainty, "Laser Speckle and Related Phenomena," Springer Berlin, (1975).

[99]. S. Donati and G. Martin, "Speckle-pattern intensity and phase second order conditional statistics", J. Opt. Soc. Amer., Vol. 69, pp. 1690-1694, (1979).

[100]. X. Raoul, "Etude de diodes lasers pour des applications métrologiques de la rétroinjection optique" , Thèse de l'Institut National Polytechnique de Toulouse, (2002).

[101]. M. Norgia, S. Donati, and D. D'Alessandro, "Interferometric measurements of displacement on a diffusing target by a speckle tracking technique," IEEE J. Quant. Electron., Vol. 37, pp. 800-806, (2001).

[102] S. Ottonelli, M. Dabbicco, F. De Lucia, and G. Scamarcio, "Simultaneous measurement of linear and transverse displacements by laser self-mixing", Applied Optics, Vol. 48, No. 9, pp. 1784, (2009).

[103] M. Norgia, and S. Donati, "A Displacement-Measuring Instrument Utilizing Self-Mixing Interferometry", IEEE Transactions on Instrumentation and Measurement, Vol. 52, No. 6, (2003).

[104] U. Zabit, F. Bony and T. Bosch, "Implementation of optimized trigonometric functions for a self-mixing laser diode displacement sensor under moderate feedback", IEEE SENSORS Conference Proceedings 2008, pp. 988-991. Lecce, Italy, (2008).

[105] J. Volder, "The CORDIC trigonometric computing technique," IRE Transactions on Electronic Computures, vol. EC-8, pp. 330-334, (1959).

Glossary

α	The line-width enhancement factor or factor of Henry
α_p	Coefficient representing the losses mainly due to absorption by free carriers
γ	Coefficient of contraction step used in Nelder-Mead Simplex method
C	Feedback coupling coefficient
c	Speed of light
D_0	Distance between the Laser and the target
d	Width of the laser cavity
ε	The excess fringe of the self-mixing signal
η	Initial step size parameter used in Nelder-Mead Simplex method
e	The elementary charge
F_D	Doppler frequency corresponding to the self-mixing signal frequency
g_{lin}	Linear threshold gain of the laser active region
g_{th}	Threshold gain of the laser active region
g_{th0}	Threshold gain of the active region in the absence of feedback
g_{thF}	Threshold gain of the active region in the presence of feedback
η	Initial step size parameter used in Nelder-Mead Simplex method
J	The current density
κ	Coupling effect parameter between the target and the laser cavity
λ	The laser emission wavelength
λ_F , λ_0	The laser emission wavelength with and without feedback respectively
l	Length of the laser diode cavity
l_{ext}	Length of the external cavity
μ_e	Effective refractive index of the active region
μ_{e0}	Effective refractive index of the active region in the absence of feedback
μ_{eF}	Effective refractive index of the active region in the presence of feedback
$\mu_e' - j\mu_e''$	Effective refractive index in its complex form

$\bar{\mu}_{e0}$	Effective group index of the diode in the absence of target
m_{mod}	Parameter representing the modulation of the laser diode
ν_0	Laser diode emission frequency in the absence of target
ν_F	Laser diode emission frequency in the presence of target
v_g	The group velocity
N	The number of Self-Mixing fringes
n	Density of electrons
n_F , n_{thF}	Density of electrons for the laser under feedback and at the threshold
n_0 , n_{th0}	Density of electrons for the stand-alone laser and at the threshold
n_{nul}	Density of electrons corresponding to a null gain.
ρ	Coefficient of reflection step used in Nelder-Mead Simplex method
P_0	The laser optical power without feedback
P_F	The laser optical power with feedback
r'_1 , r_2	Reflection coefficients for the electric field amplitude at the interfaces of the active laser diode cavity (subscript denotes the respective interface)
r_3	Reflection coefficient for the electric field amplitude at the target
r_{eq}	Reflection coefficient for the electric field amplitude for equivalent cavity
σ	Coefficient of shrinkage step used in Nelder-Mead Simplex method
S_0	Density of photons for the stand-alone laser
S_F	Density of photons for the laser under feedback
τ_{ext}	Time of flight of the laser beam in the external cavity
τ_l	Time of flight of the laser beam in the laser cavity
τ_n	Electron half-life
t	time
V	Laser diode junction voltage
V_F	Velocity of the target
x_0 , x_F	Phase of the laser emission without and with feedback respectively
ϕ_{eq}	Inverse of the phase of the equivalent cavity reflection coefficient for the electric field amplitude

ϕ_0 , ϕ_F	Phase of the laser emission without and with feedback respectively
χ	Coefficient of expansion step used in Nelder-Mead Simplex method
Ψ	The angle of the rotating surface with the laser propagation direction

List of Publications

International Journals with Peer Review

[J1] **U. Zabit**, T. Bosch, and F. Bony, “Adaptive Transition Detection Algorithm for a Self-Mixing Displacement Sensor”, IEEE Sensors Journal, Volume 9, Issue 12, pp. 1879 – 1886, (2009).

[J2] **U. Zabit**, T. Bosch, F. Bony and A. D. Rakic, “A Self-mixing Displacement Sensor with Fringe-loss Compensation for Harmonic Vibrations”, IEEE Photonics Technology Letters, vol. 22, No. 6, pp. 410 – 412, (2010).

[J3] **U. Zabit**, R. Atashkhooei, T. Bosch, S. Royo, F. Bony and A. D. Rakic, “Adaptive self-mixing vibrometer based on a liquid lens”, Optics Letters, Vol. 35, No. 8, pp. 1278-1280, (2010).

International Conferences

[C1] **U. Zabit**, F. Bony and T. Bosch, “Implementation of optimized trigonometric functions for a self-mixing laser diode displacement sensor under moderate feedback”, IEEE International SENSORS Conference Proceedings 2008, pp. 988-991. Lecce, Italy, (2008).

[C3] **U. Zabit**, T. Bosch, and F. Bony, “A fast derivative-less optimization of the feedback coupling coefficient for a self-mixing laser displacement sensor”, IEEE International Conference NEWCAS-TAISA 2009, Toulouse, France (2009).

[C3] T. Bosch**, U. Zabit** and F. Bony, “Optimisation of the performances of a self-mixing laser diode displacement sensor under moderate feedback based on the Nelder-Mead simplex method”, The 2nd International conference on Sensing Technology, New Zealand, November 26-28, (2007).

Invited Chapter of a Book

[B1] **U. Zabit**, F. Bony and T. Bosch, “Optimisation of the Nelder-Mead Simplex Method for Its Implementation in A Self-Mixing Laser Displacement Sensor”, Smart Sensors and Sensing Technology, Vol. 20, Springer, pp 381-400, (2008).

Patent

[P1] **U. Zabit**, O. Bernal, T. Bosch and F. Bony, “Title: An optical instrument for a physical parameter measurement”, “Titre: Dispositif de mesure optique d'un paramètre physique”, Deposit No. FR : 10 53648, Date of submission: 11/05/2010, (2010).

Research Prize

[R1] **U. Zabit**, O. Bernal, T. Bosch and F. Bony, “Design of an embedded optoeletronic sensor based on self-mixing”, Prize Category “Research in Education Sector”, European Mechatronics Meeting (EMM) , 2nd-3rd June 2010, Grand Bornand Annecy, France, (2010).

Résumé / Abstract

Title: Optimisation of a self-mixing laser displacement sensor.

Abstract: Optical Feedback Interferometry, also known as Self-Mixing, results in compact, self-aligned and contact-less sensors. In this phenomenon, a portion of the laser beam is back reflected from the target and enters the active laser cavity to vary its spectral properties. The laser diode then simultaneously acts as a light source, a micro-interferometer as well as a light detector. In this thesis, a self-mixing displacement sensor has been optimised so that precise measurement can be obtained in real-time. The sensor is robust to the disappearance of self-mixing fringes for harmonic vibrations. It is also able to auto-adapt itself to a change in the optical feedback regime and so can extract displacement from the weak as well as moderate feedback regime signals. The use of adaptive optics, in the form of a liquid lens, has also been demonstrated for this sensor, which has allowed us to maintain the sensor in a fringe-loss less regime. The influence of speckle has also been reduced so that the sensor can now measure up to the centimetric range for non-cooperative targets. A novel technique has also been presented that makes the sensor insensitive to parasitic mechanical vibrations that would falsify the measurement under industrial conditions.

Key Words: Self-Mixing, Optical Feedback Interferometry, Displacement Measurement, Vibration Measurement, Adaptive Optics, Laser Diode Sensor

---

Titre: Optimisation d’un capteur laser de déplacement par interférométrie à rétro-injection optique.

Résumé : L’interférométrie à rétro-injection optique, également connu sous le nom de Self-Mixing, permet de concevoir des capteurs qui sont compacts, auto-alignés et sans contact. Dans ce phénomène, une partie du faisceau laser de retour réfléchi par la cible rentre dans la cavité active de laser et fait varier ses propriétés spectrales. La diode laser agit alors comme une source de lumière, un micro-interféromètre ainsi qu'un détecteur de lumière. Dans cette thèse, un capteur de déplacement, basé sur la rétro-injection optique, a été optimisé de sorte que des mesures précises peuvent être obtenues en temps réel. Le capteur est robuste à la disparition des franges de self-mixing pour des vibrations harmoniques. Il est également capable de s’adapter à un changement dans le régime de feedback optique et peut donc extraire le déplacement dans les cas les plus répandus expérimentalement, à savoir un feedback faible puis modéré. L'utilisation de l'optique adaptative, sous la forme d'une lentille liquide, a également été démontrée pour ce capteur, ce qui nous a permis de maintenir le capteur dans un régime de feedback favorable. L'influence du speckle a également été réduite de telle sorte que le capteur mesure jusqu'à la gamme centimétrique pour des cibles non-coopératives. Une nouvelle technique est également présentée, elle permet de rendre le capteur insensible aux vibrations mécaniques parasites qui fausseraient la mesure pour des conditions industrielles.

Mots Clés: Interférométrie à rétro-injection optique, Mesure de déplacement, Mesure de vibration, Optique adaptative, Capteur diode laser